

Assignment 1

Professor:

José Manuel de Almeida César de Sá

Student:

José Luís Passos Vila-Chã

Report presented under the scope of the
Doctoral Program in Mechanical Engineering

Porto, May 2021

Page intentionally left blank.

Contents

List of Figures	v
List of Tables	xi
1 Introduction	1
2 FFT-based methods for mechanical problems	3
2.1 Conventional FFT	4
2.2 Variational FFT	8
2.3 Other methods	8
3 Variational formulation	11
3.1 Local problem and its weak form	11
3.2 Compatibility	11
3.3 Basis functions	13
3.3.1 Numerical integration	14
3.3.2 Convolution	14
3.4 Discretization	15
3.5 Linearization	16
3.6 Algorithm	17
3.7 Extension to finite strain	18
3.7.1 Problem statement	18
3.7.2 Weak form	18
3.7.3 Projection to a compatible solution space	19
3.7.4 Discretization	19
3.7.5 Quadrature	20
3.7.6 Implementation	21
3.8 Convergence criteria	23
4 Numerical Results - Elasticity	25
4.1 Material characterization	25
4.1.1 Saint Venant-Kirchhoff model	26
4.1.2 Hencky model	27
4.2 Comparison between FFT and FEM-based homogenization	29
4.2.1 Small strain	29
4.2.2 Large strain	44

5 Numerical Results - Elastoplasticity	63
5.1 Material characterization	63
5.1.1 von Mises - small strains	64
5.1.2 von Mises - large strains	66
5.2 Comparison between FFT and FEM-based homogenization	67
6 Conclusions and Future Research	77
6.1 Conclusions and final remarks	77
6.2 Future research and challenges	78
Bibliography	81

List of Figures

4.1 Dual phased heterogeneous materials microstructure: (a) Fiber-reinforced composite (randomly distributed unidirectional circular cross-section fibers, $f = 30\%$) - 2D RVE; (b) Particle-reinforced composite (randomly distributed particles, $f = 20\%$) - 3D RVE.	26
4.2 Comparison between the Criterion I and II for FFT-based homogenization approaches, Galerkin and Basic, in the solution of the fiber-reinforced linear elastic composite equilibrium problem under uniaxial strain loading conditions: (a) Homogenized stress; (b) Computational time.	30
4.3 Comparison between the Criterion I and II for FFT-based homogenization approaches, Galerkin and Basic, in the solution of the particle-reinforced linear elastic composite equilibrium problem under uniaxial strain loading conditions: (a) Homogenized stress; (b) Computational time.	31
4.4 Comparison between the FFT and FEM-based homogenization approaches in the solution of the fiber-reinforced linear elastic composite equilibrium problem under pure shear strain loading conditions: (a) Homogenized stress; (b) Computational time; (c) Local strain field ($n_v = 600 \times 600$ discretization). Notation: linear element (L), quadratic element (Q), direct solver (DS) and iterative solver (IS)	33
4.5 Comparison between the FFT and FEM-based homogenization approaches in the solution of the fiber-reinforced linear elastic composite equilibrium problem under pure shear strain loading conditions: (a) Homogenized stress; (b) Computational time; (c) Local strain field ($n_v = 600 \times 600$ discretization). Notation: linear element (L), quadratic element (Q), direct solver (DS) and iterative solver (IS)	34
4.6 Comparison between the FFT and FEM-based homogenization approaches in the solution of the particle-reinforced linear elastic composite equilibrium problem under normal strain loading conditions: (a) Homogenized stress; (b) Computational time; (c) Local strain field ($n_v = 70 \times 70 \times 70$ discretization). Notation: linear element (L), quadratic element (Q), direct solver (DS) and iterative solver (IS)	35

4.7 Comparison between the FFT and FEM-based homogenization approaches in the solution of the fiber-reinforced linear elastic composite equilibrium problem under pure shear strain loading conditions: (a) Homogenized stress; (b) Computational time; (c) Local strain field ($n_v = 70 \times 70 \times 70$ discretization). Notation: linear element (L), quadratic element (Q), direct solver (DS) and iterative solver (IS).	36
4.8 Comparison between the FFT and FEM-based homogenization approaches in the solution of the fiber-reinforced linear elastic composite equilibrium problem under normal strain loading conditions: (a) Homogenized stress; (b) Computational time; Notation: linear element (L), quadratic element (Q).	38
4.9 Comparison between the local strain field $\varepsilon_{\mu,xx}$ obtained using FFT and FEM-based homogenization approaches in the solution of the fiber-reinforced linear elastic composite equilibrium problem under normal strain loading conditions: (a) Stiffness ratio $K = E_1/E_2 = 10^{-4}$; (b) Stiffness ratio $K = E_1/E_2 = 10^{1.5}$; Notation: quadratic element (Q).	39
4.10 Comparison between the local stress field $\sigma_{\mu,xx}$ obtained using FFT and FEM-based homogenization approaches in the solution of the fiber-reinforced linear elastic composite equilibrium problem under normal strain loading conditions: (b) Stiffness ratio $K = E_1/E_2 = 10^{-4}$; (a) Stiffness ratio $K = E_1/E_2 = 10^{1.5}$; Notation: quadratic element (Q).	40
4.11 Normal microscopic strain, $\varepsilon_{\mu,xx}$, at $y = 0$ under a normal loading scheme as a function of the x coordinate for the fiber-reinforced linear elastic composite. The stiffness ratio between the matrix phase and the particle phase is $K = E_1/E_2 = 10^{-4}$	41
4.12 Comparison between the FFT and FEM-based homogenization approaches in the solution of the particle-reinforced linear elastic composite equilibrium problem under normal strain loading conditions: (a) Homogenized stress; (b) Computational time; Notation: linear element (L), quadratic element (Q).	41
4.13 Comparison between the local strain field $\varepsilon_{\mu,xx}$ obtained using FFT and FEM-based homogenization approaches in the solution of the particle-reinforced linear elastic composite equilibrium problem under normal strain loading conditions: (a) Stiffness ratio $K = E_1/E_2 = 10^{-4}$; (b) Stiffness ratio $K = E_1/E_2 = 10^{1.5}$; Notation: quadratic element (Q).	42
4.14 Comparison between the local stress field $\sigma_{\mu,xx}$ obtained using FFT and FEM-based homogenization approaches in the solution of the particle-reinforced linear elastic composite equilibrium problem under normal strain loading conditions: (b) Stiffness ratio $K = E_1/E_2 = 10^{-4}$; (a) Stiffness ratio $K = E_1/E_2 = 10^{1.5}$; Notation: quadratic element (Q).	43
4.15 Comparison between the FFT (Criterion I and II) and FEM-based homogenization approaches in the solution of the fiber-reinforced hyperelastic (Hencky constitutive model) composite equilibrium problem under normal strain loading conditions: (a) Homogenized stress; (b) Computational time; (c) Local strain field ($n_v = 600 \times 600$ discretization). Notation: quadratic element (Q)	45

4.16 Comparison between the FFT (Criterion I and II) and FEM-based homogenization approaches in the solution of the fiber-reinforced hyperelastic (Hencky constitutive model) composite equilibrium problem under pure shear strain loading conditions: (a) Homogenized stress; (b) Computational time; (c) Local strain field ($n_\nu = 600 \times 600$ discretization). Notation: quadratic element (Q)	46
4.17 Comparison between the FFT (Criterion I and II) and FEM-based homogenization approaches in the solution of the fiber-reinforced hyperelastic (Saint Venant-Kirchhoff constitutive model) composite equilibrium problem under normal strain loading conditions: (a) Homogenized stress; (b) Computational time; (c) Local strain field ($n_\nu = 600 \times 600$ discretization). Notation: quadratic element (Q)	48
4.18 Comparison between the FFT-based and FEM-based homogenization approaches in the solution of the fiber-reinforced hyperelastic (Hencky constitutive model) composite equilibrium problem under uniaxial strain loading conditions: (a) Homogenized material response; (b) Relative error of the homogenized material response obtained with the FFT approach relative to the FEM approach; (c) Local strain field at full load ($n_\nu = 600 \times 600$ discretization). Notation: quadratic element (Q). . .	51
4.19 Comparison between the FFT-based and FEM-based homogenization approaches in the solution of the fiber-reinforced hyperelastic (Hencky constitutive model) composite equilibrium problem under shear strain loading conditions: (a) Homogenized material response; (b) Relative error of the homogenized material response obtained with the FFT approach relative to the FEM approach; (c) Local strain field at full load ($n_\nu = 600 \times 600$ discretization). Notation: quadratic element (Q).	52
4.20 Comparison between the FFT-based and FEM-based homogenization approaches in the solution of the fiber-reinforced hyperelastic (Saint Venant-Kirchhoff constitutive model) composite equilibrium problem under uniaxial strain loading conditions: (a) Homogenized material response; (b) Relative error of the homogenized material response obtained with the FFT approach relative to the FEM approach; (c) Local strain field at full load ($n_\nu = 600 \times 600$ discretization). Notation: quadratic element (Q).	55
4.21 Comparison between the FFT-based and FEM-based homogenization approaches in the solution of the fiber-reinforced hyperelastic (Hencky constitutive model) composite equilibrium problem under shear strain loading conditions: (a) Homogenized material response; (b) Relative error of the homogenized material response obtained with the FFT approach relative to the FEM approach; (c) Local strain field at full load - Only FFT available since the FEM solution did not reach full load ($n_\nu = 600 \times 600$ discretization). Notation: quadratic element (Q).	56
4.22 Comparison between the FFT and FEM-based homogenization approaches in the solution of the particle-reinforced hyperelastic (Hencky constitutive model) composite equilibrium problem under normal strain loading conditions: (a) Homogenized stress; (b) Computational time; Notation: quadratic element (Q).	58

4.23 Comparison between the local logarithmic strain field $\varepsilon_{\mu,xx}$ obtained using FFT and FEM-based homogenization approaches in the solution of the fiber-reinforced hyperelastic (Hencky constitutive model) composite equilibrium problem under normal strain loading conditions: (a) Stiffness ratio $K = E_1/E_2 = 10^{-2}$; (b) Stiffness ratio $K = E_1/E_2 = 10^4$; Notation: quadratic element (Q).	59
4.24 Comparison between the local stress field $\sigma_{\mu,xx}$ obtained using FFT and FEM-based homogenization approaches in the solution of the fiber-reinforced hyperelastic (Hencky constitutive model) composite equilibrium problem under normal stress loading conditions: (b) Stiffness ratio $K = E_1/E_2 = 10^{-2}$; (a) Stiffness ratio $K = E_1/E_2 = 10^4$; Notation: quadratic element (Q).	60
4.25 Comparison between the FFT and FEM-based homogenization approaches in the solution of the particle-reinforced hyperelastic (Saint Venant-Kirchhoff constitutive model) composite equilibrium problem under normal strain loading conditions: (a) Homogenized stress; (b) Computational time; Notation: quadratic element (Q).	61
4.26 Comparison between the local strain field $F_{\mu,xx}$ obtained using FFT and FEM-based homogenization approaches in the solution of the fiber-reinforced hyperelastic (Hencky constitutive model) composite equilibrium problem under normal strain loading conditions: (a) Stiffness ratio $K = E_1/E_2 = 10^{-4}$; (b) Stiffness ratio $K = E_1/E_2 = 10^4$; Notation: quadratic element (Q).	62
5.1 Von Mises elastoplastic matrix isotropic piecewise linear strain hardening law.	64
5.2 Comparison between the FFT and FEM-based homogenization approaches in the solution of the fiber-reinforced (fibers: linear elastic; matrix: elastoplastic with a von Mises associative flow rule and the isotropic piecewise linear strain hardening law) composite equilibrium problem under normal strain loading conditions: (a) Homogenized stress; (b) Computational time; Notation: quadratic element (Q).	68
5.3 Comparison between the FFT-based and FEM-based homogenization approaches in the solution of the fiber-reinforced (fibers: linear elastic; matrix: elastoplastic with a von Mises associative flow rule and the isotropic piecewise linear strain hardening law) composite equilibrium problem under uniaxial strain loading conditions: (a) Local elastic strain field, $\varepsilon_{\mu,xx}$, of the matrix phase at full load; (b) Local accumulated plastic strain field, $\bar{\varepsilon}_p$, of the matrix phase at full load. ($n_v = 600 \times 600$ discretization). Notation: quadratic element (Q).	69
5.4 Comparison between the FFT and FEM-based homogenization approaches in the solution of the fiber-reinforced (fibers: linear elastic; matrix: elastoplastic with a von Mises associative flow rule and the isotropic piecewise linear strain hardening law) composite equilibrium problem under normal strain loading conditions: (a) Homogenized stress; (b) Computational time; Notation: linear element (L), quadratic element (Q).	70

5.5	Comparison between the FFT-based and FEM-based homogenization approaches in the solution of the fiber-reinforced (fibers: linear elastic; matrix: elastoplastic with a von Mises associative flow rule and the isotropic piecewise linear strain hardening law) composite equilibrium problem under uniaxial strain loading conditions: (a) Local elastic strain field, $\varepsilon_{\mu,xx}$, of the matrix phase at full load; (b) Local accumulated plastic strain field, $\bar{\varepsilon}_p$, of the matrix phase at full load. ($n_v = 600 \times 600$ discretization). Notation: quadratic element (Q).	71
5.6	Comparison between the FFT and FEM-based homogenization approaches in the solution of the fiber-reinforced (fibers: hyperelastic (Hencky constitutive model); matrix: elastoplastic with a von Mises associative flow rule and the isotropic piecewise linear strain hardening law) composite equilibrium problem under normal strain loading conditions: (a) Homogenized stress; (b) Computational time; Notation: quadratic element (Q).	73
5.7	Comparison between the FFT-based and FEM-based homogenization approaches in the solution of the fiber-reinforced (fibers: hyperelastic (Hencky constitutive model); matrix: elastoplastic with a von Mises associative flow rule and the isotropic piecewise linear strain hardening law) composite equilibrium problem under uniaxial strain loading conditions: (a) Local elastic strain field, $\varepsilon_{\mu,xx}$, of the matrix phase at full load; (b) Local accumulated plastic strain field, $\bar{\varepsilon}_p$, of the matrix phase at full load. ($n_v = 600 \times 600$ discretization). Notation: quadratic element (Q).	74
5.8	Comparison between the FFT and FEM-based homogenization approaches in the solution of the fiber-reinforced (fibers: hyperelastic (Hencky constitutive model); matrix: elastoplastic with a von Mises associative flow rule and the isotropic piecewise linear strain hardening law) composite equilibrium problem under pure shear strain loading conditions: (a) Homogenized stress; ?? Computational time; Notation: quadratic element (Q).	75
5.9	Comparison between the FFT-based and FEM-based homogenization approaches in the solution of the fiber-reinforced (fibers: hyperelastic (Hencky constitutive model); matrix: elastoplastic with a von Mises associative flow rule and the isotropic piecewise linear strain hardening law) composite equilibrium problem under pure shear strain loading conditions: ?? Local elastic strain field, $\varepsilon_{\mu,xx}$, of the matrix phase at full load; ?? Local accumulated plastic strain field, $\bar{\varepsilon}_p$, of the matrix phase at full load - Only FEM available since the FFT solution did not reach full load ($n_v = 600 \times 600$ discretization). Notation: quadratic element (Q). . .	76

List of Tables

2.1	Summary of the performance comparison between the investigated solution schemes (Wicht et al., 2019)	7
4.1	Specifications of the numerical testing machine.	25
4.2	Material properties for both fiber-reinforced (2D) and particle-reinforced (3D) composites.	26
4.3	Comparison between the CPU time required by the FFT-based and FEM-based homogenization approaches in the solution of the fiber-reinforced hyperelastic (Hencky constitutive model) composite equilibrium problem under uniaxial and pure strain loading conditions ($n_v = 600 \times 600$).	50
4.4	Time profile for the FFT-based homogenization approach in the solution of the fiber-reinforced hyperelastic (Hencky constitutive model) composite equilibrium problem under uniaxial strain loading conditions ($n_v = 600 \times 600$).	50
4.5	Comparison between the CPU time required by the FFT-based and FEM-based homogenization approaches in the solution of the fiber-reinforced hyperelastic (Saint Venant-Kirchhoff constitutive model) composite equilibrium problem under uniaxial and pure strain loading conditions ($n_v = 600 \times 600$).	53
4.6	Time profile for the FFT-based homogenization approach in the solution of the fiber-reinforced hyperelastic (Saint Venat-Kirchhoff constitutive model) composite equilibrium problem under uniaxial loading conditions ($n_v = 600 \times 600$).	54
5.1	Specifications of the numerical testing machine.	63
5.2	Comparison between the CPU time required by the FFT-based and FEM-based homogenization approaches in the solution of the fiber-reinforced (fibers: linear elastic; matrix: elastoplastic with a von Mises associative flow rule and the isotropic piecewise linear strain hardening law) composite equilibrium problem under uniaxial and pure strain loading conditions ($n_v = 600 \times 600$).	67
5.3	Comparison between the CPU time required by the FFT-based and FEM-based homogenization approaches in the solution of the fiber-reinforced (fibers: hyperelastic (Hencky constitutive model); matrix: elastoplastic with a von Mises associative flow rule and the isotropic piecewise linear strain hardening law) composite equilibrium problem under uniaxial and pure strain loading conditions ($n_v = 600 \times 600$).	72

Page intentionally left blank.

Chapter 1

Introduction

Chapter 2

FFT-based methods for mechanical problems

In the following, an overview of the literature on FFT-based methods for the determination of the overall and local response of a composite material from actual images or morphological simulations of its microstructure is presented.

To establish some context, let the microstructure of the material be represented by a periodic cell Ω . The material response at a point $\mathbf{x} \in \Omega$ is specified by the constitutive relation $\boldsymbol{\sigma}(\mathbf{x}, \boldsymbol{\varepsilon}(\mathbf{x}))$ assigning the stress response $\boldsymbol{\sigma}$ to a given strain $\boldsymbol{\varepsilon}$ locally at \mathbf{x} . Furthermore, the total strain $\boldsymbol{\varepsilon}$ is split into a homogeneous average strain tensor \mathbf{E} and an Ω -periodic fluctuating strain field $\boldsymbol{\varepsilon}^*$, i.e.

$$\boldsymbol{\varepsilon}(\mathbf{x}) = \mathbf{E} + \boldsymbol{\varepsilon}^*(\mathbf{x}) \text{ for } \mathbf{x} \in \Omega, \quad \int_{\Omega} \boldsymbol{\varepsilon}^*(\mathbf{x}) d\mathbf{x} = \mathbf{0}. \quad (2.1)$$

The average strain \mathbf{E} represents a given macro-scale excitation, while the fluctuating micro-scale strain field $\boldsymbol{\varepsilon}^*$ is the primary unknown.

The fluctuating strain field $\boldsymbol{\varepsilon}^*$ is determined by the stress equilibrium and strain compatibility conditions, which under quasi-static assumptions and in small strains read as,

$$-\nabla \cdot \boldsymbol{\sigma}(\mathbf{x}, \mathbf{E} + \boldsymbol{\varepsilon}^*(\mathbf{x})) = \mathbf{0} \text{ for } \mathbf{x} \in \Omega, \quad (2.2)$$

$$\boldsymbol{\varepsilon}^* \in \mathcal{E} = \{\nabla_s \mathbf{u}^*, \mathbf{u}^* \text{ is an } \Omega\text{-periodic displacement field}\}, \quad (2.3)$$

where $\nabla \cdot$ stands for the divergence operator and ∇_s stands for the symmetrized gradient operator. The goal of the methods presented in the following is to solve Equation (2.2) under the compatibility restriction expressed by Equation (2.3).

The FFT based methods, first introduced by [Moulinec and Suquet \(1994, 1995\)](#), enjoy wide usage across many domains. They have been integrated into efficient and robust two-scale FE-FFT-based computational approaches ([Kochmann et al., 2018a](#)) and now even figure in commercial software such as DAMASK ([Roters et al., 2019](#)) and FeelMath ([Schwichow, 2020](#); [Fraunhofer ITWM, 2020](#)). Their application ranges from crystal plasticity (e.g. [Lebensohn \(2001\)](#); [Shanthraj et al. \(2015\)](#); [Kochmann et al. \(2018b\)](#); [Lebensohn and Rollett \(2020\)](#); [Wicht et al. \(2020b\)](#)), hypoelasticity (e.g. [Ma and Truster \(2019\)](#)), failure and damage (e.g. [Ernesti et al. \(2020\)](#); [Ernesti and Schneider \(2021\)](#); [Geus \(2016\)](#); [Magri et al. \(2021\)](#); [Wang et al. \(2018\)](#)) and

multi-physics simulations (e.g. [Vinogradov and Milton \(2008\)](#); [Brenner \(2010\)](#); [Shanthraj et al. \(2019\)](#); [Göküzüm et al. \(2019\)](#); [Zhou and Bhattacharya \(2020\)](#); [Wicht et al. \(2020a\)](#)). They have also been used in the context of reduced order models (e.g. [Kochmann et al. \(2019\)](#); [Gierden et al. \(2021\)](#)).

Comparisons between the FEM and the FFT-based methods can be found in [Michel et al. \(1999\)](#) and [Vondřejc and Geus \(2020\)](#). The first focuses on the "basic scheme" and concludes that the FFT-based method is much faster than FEM when the contrast between phase properties is not too large. This advantage decreases as the contrast increases, in favor of the FEM. In the second contribution, Galerkin-based formulations are considered. The advantage of FEM for the case of rough data with jumps in material coefficients regarding both memory usage and speed is reasserted. The results for continuous material coefficients are inconclusive.

The main classification scheme adopted follows [Zeman et al. \(2017\)](#) and is based on the discretization approach. The first set of methods, which include the original contribution from [Moulinec and Suquet \(1994\)](#), are labeled as "Conventional FFT" and the second class as "Variational FFT". In the last section, a few methods not fitting this classification scheme are also presented.

2.1 Conventional FFT

Following [Zeman et al. \(2017\)](#), the "Conventional FFT" methods, based on the basic scheme by [Moulinec and Suquet \(1994\)](#), are derived from the following integral equation for the fluctuating strains $\boldsymbol{\varepsilon}^* \in \mathcal{E}$,

$$\int_{\Omega} \Gamma^{\text{ref}}(\mathbf{x} - \mathbf{y}) : \boldsymbol{\sigma}(\mathbf{y}, \mathbf{E} + \boldsymbol{\varepsilon}^*(\mathbf{y})) d\mathbf{y} = \mathbf{0} \text{ for all } \mathbf{x} \in \Omega, \quad (2.4)$$

where Γ^{ref} is the Green function of the reference problem. This reference problem is an auxiliary local problem with the homogeneous constitutive relation

$$\boldsymbol{\sigma}(\mathbf{x}, \boldsymbol{\varepsilon}(\mathbf{x})) = \mathbf{C}^{\text{ref}} : \boldsymbol{\varepsilon}(\mathbf{x}) \text{ for } \mathbf{x} \in \Omega. \quad (2.5)$$

In the seminal contribution by [Moulinec and Suquet \(1994, 1995\)](#), Equation (2.4) is solved using a fixed-point iteration scheme after discretizing it through a point collocation method, the basis function being trigonometric polynomials ([Zeman et al., 2017](#)). It is originally formulated for linear elasticity and small strains. In [Michel et al. \(2000, 2001\)](#), the authors extend this scheme to materials with non-linear mechanical behavior laws.

It has become very popular as a method used for the determination of local fields and effective properties since it does not require meshing. Thus, it allows the direct use of experimental images obtained by advanced imaging techniques such as micro-computed tomography. Besides, from a computational standpoint, it is also a very fast and memory-efficient method. It enjoys from current implementations of the Fast Fourier transform, which are extremely powerful. Moreover, the scheme supports matrix-free solvers, even for strongly non-linear materials. Lastly, the method is also simple to code and use.

Despite all these favorable characteristics, the method also has some drawbacks. It is not suitable for composites with infinite contrast between the phases and near interfaces between phases where large differences in the material properties are found, spurious features have also been reported ([Ma et al., 2021](#)). Furthermore, the convergence rate as a function of the material contrast is only linear.

As already mentioned, this class of methods uses a regular mesh, where the basis functions are trigonometric polynomials. Exceptions are [Bonnet \(2007\)](#), [Monchiet and Bonnet \(2012\)](#), [Monchiet \(2015\)](#) and [Nguyen et al. \(2021\)](#). In the first three, the exact Fourier transforms of the elasticity tensor are used. This can be achieved because the Fourier transforms of the characteristic functions of the inclusion phases are known, being limited to circles and ellipses. The last work uses the approximate Fourier transform of the elasticity tensor, but the phases are not limited to circles and ellipses. More complex phase domains are approximated through the union of polygon and polyhedra (e.g. flower-shaped inclusions in 2D and torus-shaped inclusion in 3D) for which the Fourier transforms of the characteristic functions are known.

A further classification of the "Conventional methods" can be introduced, according to [Schneider \(2019\)](#). For the first kind, each iterate satisfies the mechanical compatibility condition, whereas, for the second kind, compatibility is only ensured upon convergence. The polarization schemes and solvers based on the Hashin-Shtrikman principle constitute the former kind. The latter includes the conjugate gradient method, the Newton-scheme (coupled to different linear solvers), and the fast gradient methods.

Regarding the contributions based on polarization, the original work is due to [Eyre and Milton \(1999\)](#). It is developed in the context of electrical conductivity, hence the use of the term "polarization" in connection with these schemes. Accordingly, the procedure iterates on the polarization field, and not on the strain field, as per usual. Combined with the rewriting of the expression for the original scheme, this leads to faster convergence rates, superlinear, when compared with the "basic scheme", as a function of the material contrast. In [Michel et al. \(2001\)](#) this approach is extended to linear elasticity, and a related approach based on an augmented Lagrangian is also introduced. Convergence for infinite contrast is achieved for this last method. Lastly, in [Monchiet and Bonnet \(2012\)](#) a further extension is proposed, with the scheme suggested including both of the polarization-based works previously mentioned. Convergence for infinite contrast is likewise achieved. In [Schneider et al. \(2019\)](#) two flaws in these methods are pointed out in the non-linear context. Firstly, the optimal choice of algorithmic parameters is only known for the linear elastic case. Secondly, in its original version, each iteration of the polarization scheme requires solving a nonlinear system of equations for each voxel. The authors cast these methods into a simpler form using the Douglas-Rachford splitting, thus, avoiding the solution of non-linear equations in each iteration. In [Moulinec and Silva \(2014\)](#), [Moulinec et al. \(2014\)](#) and [Schneider et al. \(2019\)](#) comparisons between these methods and others can be found. Finally, the linear solvers of [Brisard and Dormieux \(2010, 2012\)](#) also belong to the class of polarization schemes, although they operate on a different polarization ([Schneider, 2020b](#)).

Beyond the "basic scheme" of [Moulinec and Suquet \(1994\)](#) further improvements within the same framework have been proposed. In the first place improvements still dealing with linear behavior at small strains are introduced. In the original approach, a fixed point iteration/Richardson iteration/Neumann series-based scheme is used (see [Moulinec et al. \(2018\)](#) for an in-depth convergence analysis). It is the most memory-efficient method available in its class and is also robust, but slow for highly contrasted problems. Moreover, the only role of the (material-dependent) reference problem is to ensure the convergence of the Richardson iteration scheme used to solve the resulting system of linear equations. As an alternative, [Zeman et al. \(2010\)](#) propose a conjugate gradient-based approach. It proceeds from the discretization of the governing integral

equation by the trigonometric collocation method to give a linear system that can be efficiently solved by conjugate gradient methods. The authors claim a significant increase of the convergence rate for problems with high-contrast coefficients at a low overhead per iteration. The scheme is also independent of the reference problem.

According to [Kabel et al. \(2014\)](#), regarding non-linear problems, be it concerning small or large strain, there are two solution strategies. Firstly, a fixed point iteration can be employed to solve the nonlinear equation introduced in [Moulinec and Suquet \(1998\)](#) for small deformations and extended to large deformations in [Eisenlohr et al. \(2013\)](#). Also for small deformations, [Schneider et al. \(2017\)](#) and [Schneider \(2020a\)](#) present the use of the fast gradient methods (Nesterov's method, heavy-ball method, and Fletcher-Reeves CG), which also forego the linearization of the nonlinear equations. The fast gradient methods combine fast convergence with a low memory footprint. However, they suffer from a delicate parameter selection ([Schneider, 2020a](#)).

Alternatively, one can use the Newton or quasi-Newton methods to tackle the nonlinear problem by solving a sequence of linear problems. In the context of small strains, [Gélébart and Mondon-Cancel \(2013\)](#) solve the linearized equations found through the Newton method using the conjugate gradient scheme. Low sensitivity to the reference material and an improved efficiency, for a soft or a stiff inclusion, when compared to the "basic scheme" is reported. In addition to prescribed macroscopic strain, the proposed method is extended to mixed loadings.

Concerning large strains, using Newton methods to linearize the nonlinear equations, [Lahellec et al. \(2003\)](#) present a scheme where a fixed-point approach is used to solve the linearized equations. In [Kabel et al. \(2014\)](#), fixed-point schemes are also considered, in addition to Newton-Raphson and Newton-Krylov/conjugate gradient methods. In connection to the last method, a memory-efficient version is also presented.

Quasi-Newton methods are available in the literature, as well. In [Wicht et al. \(2019\)](#) two algorithms based on the Broyden-Fletcher-Goldfarb-Shanno (BFGS) method, one of the most powerful Quasi-Newton schemes, are introduced. More specifically, the BFGS update formula is utilized to approximate the global Hessian or the local material tangent stiffness. Both for Newton and Quasi-Newton methods, a globalization technique is necessary to ensure global convergence. Specific to the FFT-based context, a Dong-type line search is promoted, avoiding function evaluations altogether. Another Quasi-Newton method, mentioned in [Wicht et al. \(2019\)](#) and extended to polarization methods in [Wicht et al. \(2021\)](#), is the Anderson acceleration method. It is a method for improving the convergence behavior of fixed-point iterations, where derivatives of the fixed-point mapping are not available. Based on a limited number (the so-called depth) of previous iterates, Anderson acceleration generates the next iterate based on a mixture of previous iterates, where the mixing coefficients solve an associated low-dimensional optimization problem. In [Schneider \(2019\)](#) the Barzilai-Borwein is applied to the problem at hand. It may be interpreted as the basic scheme with adaptive time-stepping (or, equivalently, adaptive reference material). Thus, it has a low memory footprint but is competitive in terms of convergence speed when compared to the solvers mentioned above. However, it is an intrinsically non-monotone method, ie, the residual is not monotonically decreasing from one iteration to the next. This behavior is unfamiliar and may limit the applicability for industrial applications.

Table 2.1 reproduces a Table found in [Wicht et al. \(2019\)](#) detailing the memory footprint and other characteristics regarding the different solvers available.

Table 2.1: Summary of the performance comparison between the investigated solution schemes (Wicht et al., 2019)

Solution scheme	Memory footprint (strain-like fields)	Summary and remarks
Basic scheme	1	<ul style="list-style-type: none"> • Gradient descent method • Lowest memory requirements • Slowest among the studied solvers
Anderson acceleration	$2m + 2$	<ul style="list-style-type: none"> • Limited-memory Quasi-Newton method • Optimal depth m between 2 and 5 • Accelerates the basic scheme but slower than the remaining algorithms
L-BFGS	$2m + 4$	<ul style="list-style-type: none"> • Limited-memory Quasi-Newton method • Optimal depth m between 2 and 5 • Outperformed by the more memory-efficient Barzilai-Borwein method
Barzilai-Borwein	2	<ul style="list-style-type: none"> • Gradient descent with step size based on Quasi-Newton methods • Nonmonotonic convergence behavior • Fastest choice for inexpensive material laws
Newton-CG	8.5	<ul style="list-style-type: none"> • Inexact Newton method • Highest efficiency in combination with Eisenstat and Walker's forcing-term choice 2 • Requires computing the material tangent • Fastest choice for expensive material laws
BFGS-CG	10.5	<ul style="list-style-type: none"> • Inexact Quasi-Newton method • Uses the BFGS update to approximate the material tangent • Matches performance of Newton-CG for small load steps, slightly slower otherwise

Abbreviations: BFGS, Broyden-Fletcher-Goldfarb-Shanno; CG, conjugate gradient.

2.2 Variational FFT

According to [Zeman et al. \(2017\)](#) the so-called "Variational FFT" schemes, are based on the weak form of the equilibrium equation

$$\int_{\Omega} \delta \boldsymbol{\varepsilon}^*(\mathbf{x}) : \boldsymbol{\sigma}(\mathbf{x}, \mathbf{E} + \boldsymbol{\varepsilon}^*(\mathbf{x})) d\mathbf{x} = 0, \quad (2.6)$$

with the compatibility constraint enforced by

$$\delta \boldsymbol{\varepsilon}^*(\mathbf{x}) = [\mathbf{G} * \boldsymbol{\zeta}](\mathbf{x}) = \int_{\Omega} \mathbf{G}(\mathbf{x} - \mathbf{y}) : \boldsymbol{\zeta}(\mathbf{y}) d\mathbf{y} \text{ for } \mathbf{x} \in \Omega, \quad (2.7)$$

where \mathbf{G} is a projection operator, $\boldsymbol{\zeta}$ is a test function and $*$ stands for the convolution.

Vondřejc and co-workers first established the connection between FFT-based schemes and Finite Elements in the framework of conventional Galerkin methods with a specific choice of basis functions and numerical quadrature ([Vondřejc et al., 2014](#)) or exact integration ([Vondřejc et al., 2015](#)) for small strains. The main advantage of this approach is the fact that it does not rely on the notion of a reference problem. Such a feature is particularly attractive for non-linear problems, for which the concept of the Green functions cannot be used. From a conceptual standpoint, this framework has the benefit that discretization, quadrature, constitutive linearization, and the solution of a linear system can be properly distinguished and optimized individually (see e.g. [Mishra et al. \(2015\)](#), [Mishra et al. \(2016\)](#) and [Vondřejc and Geus \(2020\)](#)).

[Zeman et al. \(2017\)](#) offers a very clear presentation of this approach and supplies the demonstrations regarding robust convergence for several types of non-linear constitutive behavior in small strains. In [De Geus et al. \(2017\)](#) the extension to finite strain is achieved, and the corresponding Python code of only 59 lines (without comments) is also supplied for a linear hyperelastic material. A further extension is advanced in [Lucarini and Segurado \(2019a\)](#), where stress and mixed control of the macroscopic load history is achieved using a direct method based on a modified project operator and preserving the computational performance of the original method.

Having arrived at the set of non-linear equations found from the discretization of Equation (2.6), the methods used to solve them can, in principle, be the ones detailed above for the "Conventional FFT".

2.3 Other methods

This section collects together all the contributions that do not fit into the above categories of "Conventional FFT" and "Variational FFT".

Following Willot and co-workers ([Willot and Pellegrini, 2008](#); [Willot et al., 2014](#); [Willot, 2015](#)) the equilibrium equations are discretized using finite differences, and these discretized equations are solved using the "basic scheme". The only difference is found in the Green operator, nevertheless, it leads to much more accurate local fields, particularly in the very stiff or soft inclusions and in the vicinity of interfaces. The convergence rate is also found to be much faster compared with the different methods employing the original operator, in particular for highly-contrasted media. Different finite difference and finite element discretizations have also been introduced ([Schneider et al., 2016, 2017](#); [Djaka et al., 2017](#); [Eloh et al., 2019](#)). [Brisard and Dormieux \(2010, 2012\)](#) introduced a discretization by voxel-wise constant finite elements based

on the Hashin-Shtrikman variational principle (Hashin and Shtrikman, 1962). Also based on the same principle, Tu et al. (2020) discretizes the problem using splines instead.

In Yvonnet (2012), unlike other algorithms presented so far based on the Fourier transform, the scheme put forth strictly operates in the real-space domain and removes the numerical Fourier and inverse Fourier transforms at each iteration. For this purpose, the linear operator related to the Lippmann–Schwinger equation is constructed numerically employing transformation tensors in the real-space domain.

Concerning the approximate discretization of microstructure features, more precisely of the voxels which include the interface between phases, Mareau and Robert (2017) proposes the use of composite voxel methods. These methods use simple homogenization rules to calculate the effective behavior of heterogeneous voxels, capturing more accurately, the fact they contain material that belongs to different phases. Another example of similar techniques can be found in Kabel et al. (2017).

Lucarini and Segurado (2019b) present a method completely distinct from the ones presented so far in that the unknown field is not the strain field but the displacement field. It is shown that the algorithm does not require the definition of a reference medium and that the linear systems which arise in the method are fully ranked and therefore admit the use of preconditioners. Furthermore, in the iterative solution procedure, the convergence rate is higher than the FFT-based variational approach, and the memory usage lower.

In To and Bonnet (2020) an FFT-based numerical scheme to compute the effective conductivity of porous materials is developed. To avoid the convergence issues due to the nonuniqueness of the full field solution, the problem is reformulated using the temperature field in the skeleton as an unknown variable. Thus, in the derived governing equation, the internal temperature field can be computed from the value on the pore boundary.

Chapter 3

Variational formulation

3.1 Local problem and its weak form

In what follows, the microstructure of the material is to be represented by a periodic cell Ω_μ . In two dimensions, $\Omega_\mu = (-l_1/2, l_1/2) \times (-l_2/2, l_2/2)$ with area $v_{\mu,0} = l_1 l_2$. In three dimensions, $\Omega_\mu = (-l_1/2, l_1/2) \times (-l_2/2, l_2/2) \times (-l_3/2, l_3/2)$ with volume $v_{\mu,0} = l_1 l_2 l_3$. The material response at a point $Y \in \Omega_{\mu,0}$ is specified by the constitutive relation $\sigma_\mu(Y, \epsilon_\mu(Y))$ assigning the stress response σ_μ to a given strain ϵ_μ locally at Y . Furthermore, the total strain ϵ_μ is split into a homogeneous average strain tensor present at the macroscopic point X , $\epsilon(X)$, and an Ω_μ -periodic fluctuating strain field $\tilde{\epsilon}_\mu(Y)$, i.e.

$$\epsilon_\mu(Y) = \epsilon(X) + \tilde{\epsilon}_\mu(Y) \text{ for } Y \in \Omega_{\mu,0}, \quad \int_{\Omega_{\mu,0}} \tilde{\epsilon}_\mu(Y) d\nu = \mathbf{0}. \quad (3.1)$$

The average strain $\epsilon(X)$ represents a given macro-scale excitation, while the fluctuating micro-scale strain field $\tilde{\epsilon}_\mu$ is the primary unknown.

The fluctuating strain field $\tilde{\epsilon}_\mu$ is determined by the stress equilibrium and strain compatibility conditions, which under quasi-static assumptions and in small strains read as,

$$\operatorname{div} \left[\sigma_\mu \left(Y, \epsilon(X) + \tilde{\epsilon}_\mu(Y) \right) \right] = 0 \text{ for } Y \in \Omega_{\mu,0}, \quad (3.2)$$

$$\tilde{\epsilon}_\mu \in \mathcal{E} = \left\{ \nabla_0^s \tilde{\mathbf{u}}_\mu \mid \tilde{\mathbf{u}}_\mu \text{ is an } \Omega_\mu\text{-periodic displacement field} \right\}, \quad (3.3)$$

where ∇_0^s stands for the symmetrized gradient operator. For the numerical treatment, the local problem (3.2) is recast into the weak form, which amounts to finding $\tilde{\epsilon}_\mu \in \mathcal{E}$ such that

$$\int_{\Omega_{\mu,0}} \delta \tilde{\epsilon}_\mu(Y) : \sigma_\mu \left(Y, \epsilon(X) + \tilde{\epsilon}_\mu(Y) \right) d\nu = 0, \quad (3.4)$$

holds for all $\delta \tilde{\epsilon}_\mu \in \mathcal{E}$ (where use has been made of the periodicity of the problem eliminate the boundary term).

3.2 Compatibility

The main difference in how one proceeds from the weak form (3.4) with respect to the conventional FE method is in the way in which the compatibility constraint,

Equation (3.3), is imposed for both the solution $\tilde{\epsilon}_\mu$ and the test fields $\delta\tilde{\epsilon}_\mu$. Commonly, these quantities are expressed with the help of Ω_μ -periodic displacement fields $\tilde{\mathbf{u}}_\mu$ and $\delta\tilde{\mathbf{u}}_\mu$. As $\tilde{\epsilon}_\mu = \nabla_0^s \tilde{\mathbf{u}}_\mu$ and $\delta\tilde{\epsilon}_\mu = \nabla_0^s \delta\tilde{\mathbf{u}}_\mu$, their compatibility follows directly by definition (3.3). Fourier-based methods, on the other hand, work directly with the strains and impose the compatibility of the solution and test fields by different means. For the test strains $\delta\tilde{\epsilon}_\mu$ the compatibility is imposed via a projection operator \mathbf{G} ,

$$\delta\tilde{\epsilon}_\mu(\mathbf{Y}) = [\mathbf{G} * \boldsymbol{\xi}](\mathbf{Y}) = \int_{\Omega_{\mu,0}} \mathbf{G}(\mathbf{Y} - \mathbf{Y}') : \boldsymbol{\xi}(\mathbf{Y}') d\mathbf{v}' \quad \text{for } \mathbf{Y} \in \Omega_{\mu,0}, \quad (3.5)$$

where $*$ stands for the convolution. This operator maps an extended test function $\boldsymbol{\xi}$, taken from the space all of square-integrable symmetric tensor fields \mathcal{H} , to its compatible part, i.e. $\mathbf{G} * \boldsymbol{\xi} \in \mathcal{E}$ for all $\boldsymbol{\xi} \in \mathcal{H}$. The compatibility of the solution, $\tilde{\epsilon}_\mu \in \mathcal{E}$, will be enforced by different means later in Section 3.5.

The convolution format of Equation (3.5) suggests that it can be conveniently treated using the Fourier transform when the Fourier transform of the operator \mathbf{G} is known analytically. Indeed, direct application of the convolution theorem¹ reveals that

$$[\mathbf{G} * \boldsymbol{\xi}](\mathbf{Y}) = \sum_{\mathbf{k} \in \mathbb{Z}^d} \check{\mathbf{G}}(\mathbf{k}) : \check{\boldsymbol{\xi}}(\mathbf{k}) \varphi^{\mathbf{k}}(\mathbf{Y}) \quad \text{for } \mathbf{Y} \in \Omega_{\mu,0}, \quad (3.6)$$

where \mathbf{k} is the discrete frequency vector in the two-dimensional Fourier domain \mathbb{Z}^d with d equal to the dimension of the problem, and $\varphi^{\mathbf{k}}$ is the complex-valued Fourier basis function. These can be written as

$$\varphi^{\mathbf{k}}(\mathbf{Y}) = \exp(i\mathbf{Y} \cdot \boldsymbol{\zeta}(\mathbf{k})) \quad \text{for } \mathbf{Y} \in \Omega_{\mu,0}, \quad (3.7)$$

where the scaled frequencies ζ_i account for the size of the unit cell through $\zeta_i(\mathbf{k}) = 2\pi k_i / l_i$, and $\check{\boldsymbol{\xi}}(\mathbf{k})$ stands for the complex-valued Fourier transform of $\boldsymbol{\xi}(\mathbf{Y})$,

$$\check{\boldsymbol{\xi}}(\mathbf{k}) = \frac{1}{v_{\mu,0}} \int_{\Omega_{\mu,0}} \boldsymbol{\xi}(\mathbf{Y}) \varphi^{-\mathbf{k}}(\mathbf{Y}) d\mathbf{v} \quad \text{for } \mathbf{k} \in \mathbb{Z}^d. \quad (3.8)$$

The closed-form expression for the Fourier transform of the projection operator $\check{\mathbf{G}}$ can be found in Equation (3.23), from which it follows that $\check{\mathbf{G}}$ is a self-adjoint operator². Notice that no approximation is made in (3.6) because all quantities are Ω_μ -periodic and the sum is infinite.

Substituting (3.6) into the weak formulation in Equation (3.4) and employing the self-adjointness of \mathbf{G} provides an equivalent characterization of the unknown strain field $\tilde{\epsilon}_\mu \in \mathcal{E}$:

$$\begin{aligned} \int_{\Omega_{\mu,0}} [\mathbf{G} * \boldsymbol{\xi}](\mathbf{Y}) : \boldsymbol{\sigma}_\mu(\mathbf{Y}, \boldsymbol{\epsilon}(\mathbf{X}) + \tilde{\epsilon}_\mu(\mathbf{Y})) d\mathbf{v} = \\ \int_{\Omega_{\mu,0}} \boldsymbol{\xi}(\mathbf{Y}) : [\mathbf{G} * \boldsymbol{\sigma}_\mu](\mathbf{Y}, \boldsymbol{\epsilon}(\mathbf{X}) + \tilde{\epsilon}_\mu(\mathbf{Y})) d\mathbf{v} = 0, \end{aligned} \quad (3.9)$$

for all $\boldsymbol{\xi} \in \mathcal{H}$. Because the extended test functions $\boldsymbol{\xi}$ are no longer constrained to be compatible, this form is better suited for the discretization than the original one in Equation (3.9).

¹The convolution theorem for Fourier Transforms reads: $\mathcal{F}(f * g) = \mathcal{F}(f)\mathcal{F}(g)$, for appropriate f and g .

²A self-adjoint operator A satisfies $(Af_1, f_2) = (f_1, Af_2)$.

3.3 Basis functions

The basis functions rely on an underlying regular grid of pixels $\mathbf{n}_v = [n_{v,1}, n_{v,2}]$ for 2D and of voxels $\mathbf{n}_v = [n_{v,1}, n_{v,2}, n_{v,3}]$ with $n_v = n_{v,1} \cdot n_{v,2}$ and $n_v = n_{v,1} \cdot n_{v,2} \cdot n_{v,3}$ nodes, respectively, along each coordinate, see Figure ??.

$$\mathbf{Y}_{\mathbf{n}_v}^{\mathbf{k}} = \sum_{i=1}^d \frac{k_i l_i}{n_{v,i}} \mathbf{e}_i \quad \text{for } \mathbf{k} \in \mathbb{Z}_{\mathbf{n}_v}^{\mathbf{k}}, \text{ with } d = 2 \text{ or } 3, \quad (3.10)$$

on which the microstructure is sampled, where \mathbf{e}_i , $i = 1, 2, 3$, are the unit basis vectors. As explained below, only grids with an odd number of nodes will be considered. The individual nodes are indexed by a parameter \mathbf{k} from a reduced index set

$$\mathbb{Z}_{\mathbf{n}_v}^d = \left\{ \mathbf{k} \in \mathbb{Z}^d \mid \forall i \in [1, d] \cap \mathbb{Z} \left(-\frac{n_{v,i}}{2} < k_i < \frac{n_{v,i}}{2} \right) \right\} \quad \text{with } d = 2 \text{ or } 3, \quad (3.11)$$

it will become clear later that the indices \mathbf{k} can be naturally identified with the discrete frequencies from (3.3). Finally, we assign the integration weight $w = v_{\mu,0}/n_v$, equal to the pixel/voxel size, to each node.

It is convenient to use the *fundamental trigonometric polynomials* defined on the grid $\mathbb{Z}_{\mathbf{n}_v}^2$,

$$\varphi_{\mathbf{n}_v}^{\mathbf{k}}(\mathbf{Y}) = \frac{1}{n_v} \sum_{\mathbf{m} \in \mathbb{Z}_{\mathbf{n}_v}^d} \omega_{\mathbf{n}_v}^{-\mathbf{k}\mathbf{m}} \varphi^{\mathbf{m}}(\mathbf{k}) \quad \text{for } \mathbf{k} \in \mathbb{Z}_{\mathbf{n}_v}^d, \quad (3.12)$$

as the basis functions to approximate the weak form in Equation (3.9). Here, $\varphi^{\mathbf{m}}$ stands for the Fourier basis function (Equation (3.7)) and $\omega_{\mathbf{n}_v}^{\mathbf{k}\mathbf{m}}$ are the complex-valued coefficients of the Discrete Fourier Transform (DFT),

$$\omega_{\mathbf{n}_v}^{\mathbf{k}\mathbf{m}} = \omega_{\mathbf{n}_v}^{\mathbf{m}\mathbf{k}} = \varphi^{\mathbf{k}}(\mathbf{Y}_{\mathbf{n}_v}^{\mathbf{m}}) = \exp\left(i \mathbf{Y}_{\mathbf{n}_v}^{\mathbf{k}} \cdot \boldsymbol{\zeta}(\mathbf{m})\right) \quad \text{for } \mathbf{k}, \mathbf{m} \in \mathbb{Z}_{\mathbf{n}_v}^d. \quad (3.13)$$

The solution $\tilde{\mathbf{e}}_\mu$ and the test functions $\boldsymbol{\xi}$ in Equation (3.6) will be approximated as a linear combination of the basis functions $\varphi_{\mathbf{n}_v}^{\mathbf{k}}$; the corresponding approximation space of the tensor-valued trigonometric polynomials will be referred to as $\mathcal{T}_{\mathbf{n}_v}$. These approximations are conforming, i.e., $\mathcal{T}_{\mathbf{n}_v} \subset \mathcal{H}$, as long as the number of nodes n_v is odd. This conformity is lost when n_v is even, resulting in a much more elaborate treatment.

The computational convenience of trigonometric polynomials follows from the fact that they can be efficiently manipulated using the Fast Fourier Transform (FFT), because of (i) the involvement of the DFT coefficients $\omega_{\mathbf{n}_v}^{\mathbf{k}\mathbf{m}}$ in Equation (3.12) and (ii) the ability to work with quantities defined in the Fourier space, because they incorporate the Fourier basis functions $\varphi^{\mathbf{m}}$.

In what follows, the most important steps needed to discretize the weak form in Equation (3.4) are collected.

As can be seen from Figure ??, in the real space the fundamental trigonometric polynomials are not locally supported, unlike the conventional Finite Element shape functions, however they are still interpolatory and form the partition-of-unity, because they satisfy

$$\varphi_{\mathbf{n}_v}^{\mathbf{k}}(\mathbf{Y}_{\mathbf{n}_v}^{\mathbf{m}}) = \delta^{\mathbf{k}\mathbf{m}} \quad \text{for } \mathbf{k}, \mathbf{m} \in \mathbb{Z}_{\mathbf{n}_v}^d, \quad \sum_{\mathbf{k} \in \mathbb{Z}_{\mathbf{n}_v}^d} \varphi_{\mathbf{n}_v}^{\mathbf{k}}(\mathbf{Y}) = 1 \quad \text{for } \mathbf{Y} \in \Omega_{\mu,0}, \quad (3.14)$$

where δ^{km} is the Kronecker delta. In the Fourier domain, they are locally supported on $\mathbb{Z}_{n_v}^d$,

$$\check{\varphi}_{n_v}^k(\mathbf{m}) = 0 \quad \text{for } \mathbf{k} \in \mathbb{Z}_{n_v}^d, \mathbf{m} \in \mathbb{Z}^d \setminus \mathbb{Z}_{n_v}^d, \quad (3.15)$$

because their definition (Equation (3.12)) contains only the Fourier basis functions φ^m associated with the frequencies from the grid $\mathbb{Z}_{n_v}^d$.

As a consequence, every trigonometric polynomial $\boldsymbol{\tau} \in \mathcal{T}_{n_v}$ admits two equivalent representations on the same grid $\mathbb{Z}_{n_v}^d$ that involve its nodal values $\boldsymbol{\tau}(\mathbf{Y}_{n_v}^k)$, and the Fourier coefficients $\check{\boldsymbol{\tau}}(\mathbf{k})$. Their mutual relation is established by the forward and inverse DFTs,

$$\check{\boldsymbol{\tau}}(\mathbf{k}) = \mathcal{DFT}(\boldsymbol{\tau})(\mathbf{k}) = \frac{1}{n_v} \sum_{\mathbf{m} \in \mathbb{Z}_{n_v}^d} \omega_{n_v}^{-k\mathbf{m}} \boldsymbol{\tau}(\mathbf{Y}_{n_v}^m) \quad \text{for } \mathbf{k} \in \mathbb{Z}_{n_v}^d, \quad (3.16)$$

$$\boldsymbol{\tau}(\mathbf{Y}_{n_v}^k) = \mathcal{DFT}^{-1}(\check{\boldsymbol{\tau}})(\mathbf{Y}_{n_v}^k) = \sum_{\mathbf{m} \in \mathbb{Z}_{n_v}^d} \omega_{n_v}^{k\mathbf{m}} \check{\boldsymbol{\tau}}(\mathbf{m}) \quad \text{for } \mathbf{k} \in \mathbb{Z}_{n_v}^d. \quad (3.17)$$

3.3.1 Numerical integration

The scalar product of two trigonometric polynomials $\boldsymbol{\tau} \in \mathcal{T}_{n_v}$ and $\boldsymbol{\theta} \in \mathcal{T}_{n_v}$ can be evaluated exactly by the trapezoidal rule,

$$\int_{\Omega_{\mu,0}} \boldsymbol{\tau}(\mathbf{Y}) : \boldsymbol{\theta}(\mathbf{Y}) d\mathbf{v} = w \sum_{\mathbf{k} \in \mathbb{Z}_{n_v}^d} \boldsymbol{\tau}(\mathbf{Y}_{n_v}^k) : \boldsymbol{\theta}(\mathbf{Y}_{n_v}^k), \quad (3.18)$$

which assigns the same integration weight, equal to the pixel area w , to each grid node.

3.3.2 Convolution

Convolution. of a trigonometric polynomial $\boldsymbol{\tau} \in \mathcal{T}_{n_v}$ with the projection operator \mathbf{G} from (3.5) can be evaluated efficiently at the grid nodes $\mathbf{Y}_{n_v}^k$ by DFT. Accordingly, from Equation (3.6) one finds

$$[\mathbf{G} * \boldsymbol{\tau}](\mathbf{Y}_{n_v}^k) = \sum_{\mathbf{m} \in \mathbb{Z}^d} \check{\mathbf{G}}(\mathbf{m}) : \left[\check{\boldsymbol{\tau}}(\mathbf{m}) \varphi^m(\mathbf{Y}_{n_v}^k) \right]. \quad (3.19)$$

Noting that in the frequency domain the basis functions have compact support (Equation (3.15)) and applying the definition for the coefficients of the DFT (Equation (3.13)), yields

$$\sum_{\mathbf{m} \in \mathbb{Z}^d} \check{\mathbf{G}}(\mathbf{m}) : \left[\check{\boldsymbol{\tau}}(\mathbf{m}) \varphi^m(\mathbf{Y}_{n_v}^k) \right] = \sum_{\mathbf{m} \in \mathbb{Z}_{n_v}^d} \check{\mathbf{G}}(\mathbf{m}) : \left[\check{\boldsymbol{\tau}}(\mathbf{m}) \omega_{n_v}^{k\mathbf{m}} \right]. \quad (3.20)$$

Thus, from the definition of the Discrete Fourier Transform in Equation (3.16), the desired result is achieved

$$[\mathbf{G} * \boldsymbol{\tau}](\mathbf{Y}_{n_v}^k) = \sum_{\mathbf{m} \in \mathbb{Z}_{n_v}^d} \omega_{n_v}^{k\mathbf{m}} \check{\mathbf{G}}(\mathbf{m}) : \left[\frac{1}{n_v} \sum_{\mathbf{n} \in \mathbb{Z}_{n_v}^d} \omega_{n_v}^{-m\mathbf{n}} \boldsymbol{\tau}(\mathbf{Y}_{n_v}^n) \right], \quad (3.21)$$

which can be written in a more compact form as

$$[\mathbf{G} * \boldsymbol{\tau}](\mathbf{Y}_{n_v}^k) = \mathcal{DFT}^{-1}(\check{\mathbf{G}} : \mathcal{DFT}(\boldsymbol{\tau}))(\mathbf{Y}_{n_v}^k). \quad (3.22)$$

For the non-zero frequency $\mathbf{k} \in \mathbb{Z}_{n_v}^d \setminus \{\mathbf{0}\}$, the Fourier transform of the fourth-order projection operator $\check{\mathbf{G}}$ is provided by

$$\check{\mathbf{G}}_{ijklm}(\mathbf{k}) = \frac{1}{2} \frac{\zeta_i(\mathbf{k})\delta_{jl}\zeta_m(\mathbf{k}) + \zeta_i(\mathbf{k})\delta_{jm}\zeta_l(\mathbf{k}) + \zeta_j(\mathbf{k})\delta_{il}\zeta_m(\mathbf{k}) + \zeta_j(\mathbf{k})\delta_{im}\zeta_l(\mathbf{k})}{\|\zeta(\mathbf{k})\|^2} - \frac{\zeta_i(\mathbf{k})\zeta_j(\mathbf{k})\zeta_l(\mathbf{k})\zeta_m(\mathbf{k})}{\|\zeta(\mathbf{k})\|^4}, \quad (3.23)$$

where ζ_i are the scaled frequencies and δ_{ij} stands for the Kronecker delta. For $\mathbf{k} = \mathbf{0}$, $\check{\mathbf{G}}_{ijklm}(\mathbf{0}) = 0$ because of the zero-mean property. See Appendix (??) for the proof that \mathbf{G} is the operator with the desired properties described above.

3.4 Discretization

One is now in a position to discretize the weak form of Equation (3.4) with trigonometric polynomials. Following the standard Galerkin procedure, the unknown field $\tilde{\epsilon}_\mu$ and the test field ξ are approximated in the same way

$$\tilde{\epsilon}_\mu(\mathbf{Y}) \approx \sum_{\mathbf{m} \in \mathbb{Z}_{n_v}^d} \varphi_{n_v}^{\mathbf{m}}(\mathbf{Y}) \tilde{\epsilon}_\mu(\mathbf{Y}_{n_v}^{\mathbf{m}}), \quad (3.24)$$

$$\xi(\mathbf{Y}) \approx \sum_{\mathbf{m} \in \mathbb{Z}_{n_v}^d} \varphi_{n_v}^{\mathbf{m}}(\mathbf{Y}) \xi(\mathbf{Y}_{n_v}^{\mathbf{m}}). \quad (3.25)$$

The nodal strains, $\tilde{\epsilon}_\mu(\mathbf{Y}_{n_v}^{\mathbf{m}})$ for $\mathbf{m} \in \mathbb{Z}_{n_v}^d$, and the nodal values of test fields, $\xi(\mathbf{Y}_{n_v}^{\mathbf{m}})$ for $\mathbf{m} \in \mathbb{Z}_{n_v}^d$, are respectively located in the corresponding finite-dimensional spaces $\mathbb{E}_{n_v} \subset \mathbb{T}_{n_v}$. The (constrained) space \mathbb{E}_{n_v} thus collects the nodal values of compatible trigonometric polynomials from $\mathcal{T}_{n_v} \cap \mathcal{E}$, whereas (unconstrained) \mathbb{T}_{n_v} collects nodal values of all trigonometric polynomials from \mathcal{T}_{n_v} .

Introducing these expansions into Equation (3.9) yields

$$\int_{\Omega_{\mu,0}} \left(\sum_{\mathbf{m} \in \mathbb{Z}_{n_v}^d} \varphi_{n_v}^{\mathbf{m}}(\mathbf{Y}) \xi(\mathbf{Y}_{n_v}^{\mathbf{m}}) \right) : [\mathbf{G} * \sigma_\mu](\mathbf{Y}, \epsilon(\mathbf{X}) + \sum_{\mathbf{m} \in \mathbb{Z}_{n_v}^d} \varphi_{n_v}^{\mathbf{m}}(\mathbf{Y}) \tilde{\epsilon}_\mu(\mathbf{Y}_{n_v}^{\mathbf{m}})) d\nu = 0, \quad (3.26)$$

to be satisfied for arbitrary $\xi(\mathbf{Y}_{n_v}^{\mathbf{m}})$ from \mathbb{T}_{n_v} , $\mathbf{m} \in \mathbb{Z}_{n_v}^d$. Application of the trapezoidal quadrature rule (Equation (3.18)) provides

$$w \sum_{\mathbf{k} \in \mathbb{Z}_{n_v}^d} \left(\sum_{\mathbf{m} \in \mathbb{Z}_{n_v}^d} \varphi_{n_v}^{\mathbf{m}}(\mathbf{Y}_{n_v}^{\mathbf{k}}) \xi(\mathbf{Y}_{n_v}^{\mathbf{m}}) \right) : [\mathbf{G} * \sigma_\mu](\mathbf{Y}_{n_v}^{\mathbf{k}}, \epsilon(\mathbf{X}) + \sum_{\mathbf{m} \in \mathbb{Z}_{n_v}^d} \varphi_{n_v}^{\mathbf{m}}(\mathbf{Y}_{n_v}^{\mathbf{k}}) \tilde{\epsilon}_\mu(\mathbf{Y}_{n_v}^{\mathbf{m}})) \approx 0, \quad (3.27)$$

note that this step introduces an approximation error because the constitutive relation σ_μ does not necessarily map trigonometric polynomials to trigonometric polynomials. By exploring the Kronecker delta property of the basis functions (Equation (3.14)), the previous relation further simplifies to

$$\sum_{\mathbf{k} \in \mathbb{Z}_{n_v}^d} \xi(\mathbf{Y}_{n_v}^{\mathbf{k}}) : [\mathbf{G} * \sigma_\mu](\mathbf{Y}_{n_v}^{\mathbf{k}}, \epsilon(\mathbf{X}) + \tilde{\epsilon}_\mu(\mathbf{Y}_{n_v}^{\mathbf{k}})) = 0. \quad (3.28)$$

Because the test strains $\xi(\mathbf{Y}_{n_v}^{\mathbf{k}})$, for $\mathbf{k} \in \mathbb{Z}_{n_v}^d$, are arbitrary, one finally obtains from (3.28) that the nodal strain values, $\tilde{\epsilon}_\mu(\mathbf{Y}_{n_v}^{\mathbf{k}}) \in \mathbb{E}_{n_v}$, for $\mathbf{k} \in \mathbb{Z}_{n_v}^d$, follow from the system of

non-linear nodal equilibrium conditions,

$$[\mathbf{G} * \boldsymbol{\sigma}_\mu] \left(\mathbf{Y}_{n_v}^k, \boldsymbol{\varepsilon}(\mathbf{X}) + \tilde{\boldsymbol{\varepsilon}}_\mu \left(\mathbf{Y}_{n_v}^k \right) \right) = \mathbf{0} \quad \text{for } \mathbf{k} \in \mathbb{Z}_{n_v}^d, \quad (3.29)$$

which can be also be written as

$$\mathcal{DFT}^{-1} \left(\tilde{\mathbf{G}} : \mathcal{DFT} \left(\boldsymbol{\sigma}_\mu \right) \right) \left(\mathbf{Y}_{n_v}^k, \boldsymbol{\varepsilon}(\mathbf{X}) + \tilde{\boldsymbol{\varepsilon}}_\mu \left(\mathbf{Y}_{n_v}^k \right) \right) = \mathbf{0} \quad \text{for } \mathbf{k} \in \mathbb{Z}_{n_v}^d. \quad (3.30)$$

where the non-linearity originates solely from the constitutive relation, because the projection operator \mathbf{G} is independent of $\tilde{\boldsymbol{\varepsilon}}_\mu$.

Therefore, apart from enforcing the strain compatibility, the symmetric matrix \mathbf{G} also enforces the nodal equilibrium conditions. Also notice that, in analogy to Section 3.2, the constraint $\tilde{\boldsymbol{\varepsilon}}_\mu(\mathbf{Y}_{n_v}^k) \in \mathbb{E}_{n_v}$, for $\mathbf{k} \in \mathbb{Z}_{n_v}^d$, still needs to be accounted for.

3.5 Linearization

The conventional Newton scheme is used to find the solution to the system (3.30) iteratively. For this purpose, we express the nodal unknowns in the $(i+1)$ -th iteration as

$$\tilde{\boldsymbol{\varepsilon}}_\mu^{(i+1)} \left(\mathbf{Y}_{n_v}^k \right) = \tilde{\boldsymbol{\varepsilon}}_\mu^{(i)} \left(\mathbf{Y}_{n_v}^k \right) + \delta \tilde{\boldsymbol{\varepsilon}}_\mu^{(i+1)} \left(\mathbf{Y}_{n_v}^k \right) \quad \text{for } \mathbf{k} \in \mathbb{Z}_{n_v}^d. \quad (3.31)$$

Equation (3.30) is then linearized around $\tilde{\boldsymbol{\varepsilon}}_\mu^{(i)}$, with $\tilde{\boldsymbol{\varepsilon}}_\mu^{(0)} \left(\mathbf{Y}_{n_v}^k \right) \in \mathbb{E}_{n_v}$, for $\mathbf{k} \in \mathbb{Z}_{n_v}^d$. As a result, one obtains the linear system for the nodal strain increment $\delta \tilde{\boldsymbol{\varepsilon}}_\mu^{(i+1)} \left(\mathbf{Y}_{n_v}^k \right) \in \mathbb{E}_{n_v}$, for $\mathbf{k} \in \mathbb{Z}_{n_v}^d$,

$$\begin{aligned} [\mathbf{G} * \mathbf{K}^{(i)}] \left(\mathbf{Y}_{n_v}^k, \boldsymbol{\varepsilon}(\mathbf{X}) + \tilde{\boldsymbol{\varepsilon}}_\mu \left(\mathbf{Y}_{n_v}^k \right) \right) \delta \tilde{\boldsymbol{\varepsilon}}_\mu^{(i+1)} \left(\mathbf{Y}_{n_v}^k \right) \\ = -[\mathbf{G} * \boldsymbol{\sigma}_\mu] \left(\mathbf{Y}_{n_v}^k, \boldsymbol{\varepsilon}(\mathbf{X}) + \tilde{\boldsymbol{\varepsilon}}_\mu \left(\mathbf{Y}_{n_v}^k \right) \right) \quad \text{for } \mathbf{k} \in \mathbb{Z}_{n_v}^d, \end{aligned} \quad (3.32)$$

where the local tangent matrix $\mathbf{K}^{(i)}$ is given by

$$\mathbf{K}^{(i)} \left(\mathbf{Y}_{n_v}^k, \boldsymbol{\varepsilon}(\mathbf{X}) + \tilde{\boldsymbol{\varepsilon}}_\mu \left(\mathbf{Y}_{n_v}^k \right) \right) = \frac{\partial \boldsymbol{\sigma}_\mu}{\partial \boldsymbol{\varepsilon}_\mu} \left(\mathbf{Y}_{n_v}^k, \boldsymbol{\varepsilon}(\mathbf{X}) + \tilde{\boldsymbol{\varepsilon}}_\mu \left(\mathbf{Y}_{n_v}^k \right) \right) \quad \text{for } \mathbf{k} \in \mathbb{Z}_{n_v}^d. \quad (3.33)$$

Three considerations must be taken into account when solving the linearized system (Equation (3.32)): (i) the corresponding system matrix is dense, singular, and very costly to assemble for large grids, (ii) the multiplication with the system matrix is cheap and does not require the matrix assembly, because it involves the multiplication with structurally sparse matrices (recall that the convolution with \mathbf{G} can be performed efficiently by FFT (Equation (3.22))), and (iii) the solver must enforce the compatibility constraint $\tilde{\boldsymbol{\varepsilon}}_\mu^{(i+1)} \left(\mathbf{Y}_{n_v}^k \right) \in \mathbb{E}_{n_v}$, for $\mathbf{k} \in \mathbb{Z}_{n_v}^d$.

All these aspects invite the application of (projected) iterative solvers involving only matrix-vector products, such as specific-purpose solvers [29], or selected general-purpose iterative algorithms for symmetric positive systems [16], because the operator \mathbf{G} enforces the compatibility and equilibrium conditions simultaneously. Specifically, we will use the conventional Conjugate Gradient algorithm [30], which enforces the compatibility constraint at every iteration and outperforms alternative solvers in terms of convergence rate, as demonstrated recently in [16].

3.6 Algorithm

To summarize, the incremental-iterative Newton-Conjugate Gradient solver is outlined as a pseudo-algorithm in Box 3.1. For later reference, it is emphasized that the algorithm implements two termination criteria for the Newton and the Conjugate Gradient solvers that involve the two tolerances η^{NW} and η^{CG} , respectively. Finally, note that the same procedure applies to history- and rate-dependent material laws, once the time-incremental stress-strain laws and consistent constitutive tangents are adopted, replacing $\sigma_\mu^{(i)}$ and $\mathbf{K}^{(i)}$ in Equation (3.32).

Box 3.1: Pseudo-code for the Newton-CG algorithm solving the equilibrium problem for non-linear behavior.

- (i) Set the initial conditions: $t = t_0$
- (ii) Set strain fluctuations to zero: $\tilde{\epsilon}_\mu^{(0)}(\mathbf{Y}_{n_v}^k) = \mathbf{0}$ for $\mathbf{k} \in \mathbb{Z}_{n_v}^d$
- (iii) Initialize other history variables (material dependent)
- (iv) Enter increment loop
 - (1) Set Newton counter to zero: $i = 0$
 - (2) Initialize, indicating no convergence yet: $\delta \tilde{\epsilon}_\mu^{(i)}(\mathbf{Y}_{n_v}^k) = \infty$ for $\mathbf{k} \in \mathbb{Z}_{n_v}^d$
 - (3) Enter Newton loop
 - (a) Compute the constitutive response (material dependent):

$$\sigma_\mu^{(i)}(\mathbf{Y}_{n_v}^k) = \sigma_\mu\left(\mathbf{Y}_{n_v}^k, \epsilon(\mathbf{X}) + \tilde{\epsilon}_\mu\left(\mathbf{Y}_{n_v}^k\right)\right) \quad \text{for } \mathbf{k} \in \mathbb{Z}_{n_v}^d$$
 - (b) Compute the consistent tangent (material dependent):

$$\mathbf{K}^{(i)}(\mathbf{Y}_{n_v}^k) = \frac{\partial \sigma_\mu}{\partial \epsilon_\mu}\left(\mathbf{Y}_{n_v}^k, \epsilon(\mathbf{X}) + \tilde{\epsilon}_\mu\left(\mathbf{Y}_{n_v}^k\right)\right) \quad \text{for } \mathbf{k} \in \mathbb{Z}_{n_v}^d$$
 - (c) Use the standard Conjugate Gradient method to solve

$$[\mathbf{G} * \mathbf{K}^{(i)}]\left(\mathbf{Y}_{n_v}^k\right) \delta \tilde{\epsilon}_\mu^{(i+1)}\left(\mathbf{Y}_{n_v}^k\right) = -[\mathbf{G} * \sigma_\mu^{(i)}]\left(\mathbf{Y}_{n_v}^k\right) \quad \text{for } \mathbf{k} \in \mathbb{Z}_{n_v}^d$$

until the desired accuracy η^{CG} is reached.
 - (d) Update the strain: $\tilde{\epsilon}_\mu^{(i+1)}\left(\mathbf{Y}_{n_v}^k\right) = \tilde{\epsilon}_\mu^{(i)}\left(\mathbf{Y}_{n_v}^k\right) + \delta \tilde{\epsilon}_\mu^{(i+1)}\left(\mathbf{Y}_{n_v}^k\right)$
 - (e) If the desired accuracy η^{NW} has not been reached, update $i = i + 1$ and go to step (a).
 - (4) Set the "initial guess" for the next increment: $\tilde{\epsilon}_\mu^{(t+\Delta t)}\left(\mathbf{Y}_{n_v}^k\right) = \tilde{\epsilon}_\mu^{(i)}\left(\mathbf{Y}_{n_v}^k\right)$
 - (5) Update other history variables (material dependent)
 - (6) If $t \leq T_0$, proceed to next increment $t = t + \Delta t$ and go to step (1).

Table 1: Comparison of FFT-based and Finite Element methods.

	Finite elements	Conventional FFT	Variational FFT
Discretization approach	Galerkin	collocation	Galerkin
Computational grid	general	regular	regular
Basis functions	Lagrange	trigonometric	trigonometric
Unknown	displacement	strain	strain
Compatibility of solution	automatic	linear solver	linear solver
Compatibility of test fields	automatic	×	projection matrix \underline{G}
Equilibrium	static matrix $\underline{\mathbf{B}}^T$	Green matrix $\underline{\mathbf{\Gamma}}^{\text{ref}}$	projection matrix \underline{G}
Reference problem	×	yes	
Quadrature	Gauss	×	trapezoidal
Linear system	regular symmetric, sparse	singular non-symmetric, structurally sparse	singular non-symmetric, structurally sparse
Linear system solver	direct/iterative	iterative	iterative

3.7 Extension to finite strain

This section presents the adaptations needed to extend the scheme introduced above to finite strains.

3.7.1 Problem statement

The goal is again to solve for static mechanical equilibrium in the periodic cell for a given applied overall deformation. The balance of linear momentum, pulled-back to the (undeformed) reference configuration, reads

$$\text{div}_0 \mathbf{P}_\mu = \mathbf{0} \quad (3.34)$$

involving the divergence with respect to the reference configuration of the transposed first Piola-Kirchhoff stress tensor \mathbf{P}_μ . The stress \mathbf{P}_μ depends non-linearly on the deformation gradient \mathbf{F}_μ

$$\mathbf{P}_\mu = \mathbf{P}_\mu(\mathbf{F}_\mu). \quad (3.35)$$

3.7.2 Weak form

The integral form is obtained by multiplying (3.34) with test functions $\delta \mathbf{y}$ and integrating over the reference domain $\Omega_{\mu,0}$

$$\int_{\Omega_{\mu,0}} \delta \mathbf{y} \cdot (\text{div}_0 \mathbf{P}_\mu) \, dv = 0, \quad (3.36)$$

which must hold for all periodic $\delta \mathbf{y}$. Subsequently, integration by parts is applied in conjunction with Gauss' divergence theorem. The boundary term that arises vanishes because of periodicity. The result reads

$$\int_{\Omega_{\mu,0}} \mathbf{P}_\mu : (\text{div}_0 \delta \mathbf{y}) \, dv = 0, \quad (3.37)$$

where $:$ denotes a double tensor contraction. To make use of the FFT-based methods, the weak form of Equation (3.37) is accordingly reformulated using the deformation gradient \mathbf{F}_μ as

$$\int_{\Omega_{\mu,0}} \mathbf{P}_\mu : \delta \mathbf{F}_\mu \, dv = 0, \quad (3.38)$$

in which the test functions $\delta \mathbf{F}_\mu$ are periodic and compatible. Note that compatibility is guaranteed when $\delta \mathbf{F}_\mu$ is the gradient of a virtual position vector, as in Finite Elements, but now must be enforced as a constraint in conjunction with Equation (3.38).

3.7.3 Projection to a compatible solution space

As in the case of small strains, the compatibility of the test functions $\delta \mathbf{F}_\mu$ is imposed employing a projection operator \mathbf{G} (different from the previous one). It maps an arbitrary field $\bar{\mathbf{A}}$ to its compatible part \mathbf{A} through

$$\mathbf{G} * \bar{\mathbf{A}} = \mathbf{A}, \quad (3.39)$$

wherein $*$ is the convolution operator. The convolution can be evaluated in Fourier space as a simple, local, double tensor contraction. Furthermore, \mathbf{G} has a simple closed-form expression in Fourier space,

$$\check{\mathbf{G}}_{ijklm}(\mathbf{k}) = \begin{cases} 0 & \text{for } \mathbf{k} = \mathbf{0} \\ \frac{\delta_{im}\zeta_j(\mathbf{k})\zeta_l(\mathbf{k})}{\|\zeta\|^2} & \text{otherwise} \end{cases}, \quad (3.40)$$

wherein \mathbf{k} is the (spatial) frequency vector and ζ_i are the scaled frequencies that account for the size of the cell through $\zeta_i(\mathbf{k}) = k_i/L_i$ (with L_i the size of the periodic cell in direction i). Its background and interpretation are discussed in Appendix ??.

Application of Equation 3.39 to the weak form of Equation 3.38 results in

$$\int_{\Omega_{\mu,0}} (\mathbf{G} * \delta \bar{\mathbf{F}}_\mu) : \mathbf{P}_\mu^T d\nu = \int_{\Omega_{\mu,0}} \delta \bar{\mathbf{F}}_\mu : (\mathbf{G} * \mathbf{P}_\mu) d\nu = 0, \quad (3.41)$$

whereby the symmetry of \mathbf{G} has been used. Equation (3.41) should now hold for arbitrary, i.e. not necessarily compatible, periodic test functions $\delta \bar{\mathbf{F}}_\mu$. Please note that the deformation gradient \mathbf{F}_μ , hidden in the stress \mathbf{P}_μ through Equation (3.35), should still satisfy the compatibility constraint.

3.7.4 Discretization

Adopting a Galerkin scheme, the unknown field \mathbf{F}_μ and the test functions $\delta \bar{\mathbf{F}}_\mu$ are discretized in the same way. Like in Finite Elements, the continuous fields \mathbf{F}_μ and $\delta \bar{\mathbf{F}}_\mu$ are approximated by a finite number of n nodal values that are multiplied with shape functions associated with each node, i.e.

$$\mathbf{F}_\mu(\mathbf{Y}) \approx \sum_{\mathbf{m} \in \mathbb{Z}_{n_\nu}^2} \varphi_{n_\nu}^{\mathbf{m}}(\mathbf{Y}) \mathbf{F}_\mu(\mathbf{Y}_{n_\nu}^{\mathbf{m}}), \quad (3.42)$$

$$\delta \bar{\mathbf{F}}_\mu(\mathbf{Y}) \approx \sum_{\mathbf{m} \in \mathbb{Z}_{n_\nu}^2} \varphi_{n_\nu}^{\mathbf{m}}(\mathbf{Y}) \bar{\mathbf{F}}_\mu(\mathbf{Y}_{n_\nu}^{\mathbf{m}}). \quad (3.43)$$

Just as before, the Fundamental trigonometric polynomials are used as shape functions.

The discretization is applied to the weak form (Equation (3.41)) which therefore becomes

$$\int_{\Omega_{\mu,0}} \left(\sum_{\mathbf{m} \in \mathbb{Z}_{n_\nu}^2} \varphi_{n_\nu}^{\mathbf{m}}(\mathbf{Y}) \bar{\mathbf{F}}_\mu(\mathbf{Y}_{n_\nu}^{\mathbf{m}}) \right) : [\mathbf{G} * \mathbf{P}_\mu] \left(\mathbf{Y}_{n_\nu}^{\mathbf{k}}, \sum_{\mathbf{m} \in \mathbb{Z}_{n_\nu}^2} \varphi_{n_\nu}^{\mathbf{m}}(\mathbf{Y}) \mathbf{F}_\mu(\mathbf{Y}_{n_\nu}^{\mathbf{m}}) \right) d\nu = 0. \quad (3.44)$$

3.7.5 Quadrature

The integration is again performed using the trapezoidal rule, which applied to Equation (3.44) yields

$$w \sum_{\mathbf{k} \in \mathbb{Z}_{n_v}^2} \left(\sum_{\mathbf{m} \in \mathbb{Z}_{n_v}^2} \varphi_{n_v}^{\mathbf{m}}(\mathbf{Y}_{n_v}^{\mathbf{k}}) \bar{F}_{\mu}(\mathbf{Y}_{n_v}^{\mathbf{m}}) : [\mathbf{G} * \mathbf{P}_{\mu}] \left(\mathbf{Y}_{n_v}^{\mathbf{k}}, \sum_{\mathbf{m} \in \mathbb{Z}_{n_v}^2} \varphi_{n_v}^{\mathbf{m}}(\mathbf{Y}_{n_v}^{\mathbf{k}}) \mathbf{F}_{\mu}(\mathbf{Y}_{n_v}^{\mathbf{m}}) \right) \right) dv \approx 0. \quad (3.45)$$

The fact that the shape functions can be expressed in terms of the discrete Fourier coefficients is now exploited; and the delta property of the shape functions (Equation (3.14)), writing

$$\sum_{\mathbf{k} \in \mathbb{Z}_{n_v}^d} \bar{F}_{\mu}(\mathbf{Y}_{n_v}^{\mathbf{k}}) : [\mathbf{G} * \mathbf{P}_{\mu}] \left(\mathbf{Y}_{n_v}^{\mathbf{k}}, \mathbf{F}_{\mu}(\mathbf{Y}_{n_v}^{\mathbf{k}}) \right) = 0. \quad (3.46)$$

Because the test functions $\bar{F}_{\mu}(\mathbf{Y}_{n_v}^{\mathbf{k}})$, for $\mathbf{k} \in \mathbb{Z}_{n_v}^d$, are arbitrary, one finally obtains from (3.46) that the nodal strain values, $\mathbf{F}_{\mu}(\mathbf{Y}_{n_v}^{\mathbf{k}})$, for $\mathbf{k} \in \mathbb{Z}_{n_v}^d$, follow from the system of non-linear nodal equilibrium conditions,

$$[\mathbf{G} * \mathbf{P}_{\mu}] \left(\mathbf{Y}_{n_v}^{\mathbf{k}}, \mathbf{F}_{\mu}(\mathbf{Y}_{n_v}^{\mathbf{k}}) \right) = \mathbf{0} \quad \text{for } \mathbf{k} \in \mathbb{Z}_{n_v}^d, \quad (3.47)$$

which can be also be written as

$$\mathcal{D}\mathcal{F}\mathcal{T}^{-1} \left(\tilde{\mathbf{G}} : \mathcal{D}\mathcal{F}\mathcal{T} \left(\mathbf{P}_{\mu} \right) \right) \left(\mathbf{Y}_{n_v}^{\mathbf{k}}, \mathbf{F}_{\mu}(\mathbf{Y}_{n_v}^{\mathbf{k}}) \right) = \mathbf{0} \quad \text{for } \mathbf{k} \in \mathbb{Z}_{n_v}^d. \quad (3.48)$$

where the non-linearity originates solely from the constitutive relation, because the projection operator \mathbf{G} is independent of \mathbf{F}_{μ} .

Therefore, apart from enforcing the strain compatibility, the symmetric matrix \mathbf{G} also enforces the nodal equilibrium conditions. Also notice, that once more, the constraint regarding the compatibility of \mathbf{F}_{μ} , still needs to be accounted for.

The weak form in Equation (3.48) is a non-linear equation, as the material model involves a non-linear relation between the first Piola-Kirchhoff stress and the deformation gradient. Newton iterations are employed to solve the nodal equilibrium equations (3.48). To this end the nodal unknowns at iteration $i + 1$ are expressed as

$$\mathbf{F}_{\mu}^{(i+1)} \left(\mathbf{Y}_{n_v}^{\mathbf{k}} \right) = \mathbf{F}_{\mu}^{(i)} \left(\mathbf{Y}_{n_v}^{\mathbf{k}} \right) + \delta \mathbf{F}_{\mu} \left(\mathbf{Y}_{n_v}^{\mathbf{k}} \right) \quad \text{for } \mathbf{k} \in \mathbb{Z}_{n_v}^d, \quad (3.49)$$

where $\mathbf{F}_{\mu}^{(i)}$ are the last known iterative values of the deformation gradients and $\delta \mathbf{F}_{\mu}$ are their iterative updates. Note that δ is now used to indicate a small variation. The stresses are linearized around $\mathbf{F}_{\mu}^{(i)}$. In a material point this corresponds to

$$\delta \mathbf{P}_{\mu} = \mathbf{K}^{(i)} : \delta \mathbf{F}_{\mu}. \quad (3.50)$$

Combined with the discretized weak form in Equation (3.47), the iterative update $\delta \mathbf{F}_{\mu}$ is found by solving the following linearized system

$$[\mathbf{G} * \mathbf{K}^{(i)}] \left(\mathbf{Y}_{n_v}^{\mathbf{k}}, \mathbf{F}_{\mu}^{(i)} \left(\mathbf{Y}_{n_v}^{\mathbf{k}} \right) \right) : \delta \mathbf{F}_{\mu} \left(\mathbf{Y}_{n_v}^{\mathbf{k}} \right) = -[\mathbf{G} * \mathbf{P}_{\mu}] \left(\mathbf{Y}_{n_v}^{\mathbf{k}}, \mathbf{F}_{\mu}^{(i)} \left(\mathbf{Y}_{n_v}^{\mathbf{k}} \right) \right) \quad \text{for } \mathbf{k} \in \mathbb{Z}_{n_v}^d. \quad (3.51)$$

Note that the compatibility of the deformation gradient field still needs to be enforced. This is done by solving the linear system of Equation (3.51) using an

iterative solver which delivers a compatible solution in each iteration [18 – 21, 24]. To satisfy compatibility during the entire iterative process, projection-based iterative methods such as e.g. the conjugate gradient (CG) method and the generalized minimal residual method (GMRES), Chebyshev iterations, or Richardson iterations (used in the original Moulinec-Suquet algorithm [5, 6]) can be used [19, 20]. Alternatively, compatibility is satisfied only at convergence using the accelerated method of Ref. [25].

3.7.6 Implementation

The numerical algorithm requires the solution of (3.48) in an incremental-iterative fashion. Each increment thereby consists of Newton iterations updating the nodal deformation gradients $F_\mu^{(i+1)}(Y_{n_v}^k)$, for $k \in \mathbb{Z}_{n_v}^d$ using (3.49)-(3.51) until equilibrium is satisfied up to an accuracy η^{NW} , by employing the linearized constitutive response. The linear system in Equation (3.51) is solved up to an accuracy η^{CG} using the conjugate gradient iterative solver.

Boundary conditions With the periodic micro-fluctuations of F_μ following from equilibrium and compatibility, only the macroscopic deformation or stress needs to be prescribed. Here only a fully prescribed macroscopic deformation gradient is considered \bar{F}_μ , as this is the easiest and the most efficient choice.

The starting point is an equilibrium state given by $F_\mu^{(0)}$, to which a macroscopic deformation gradient \bar{F}_μ is applied. More specifically, we apply the difference of F and to the mean of $F_\mu^{(0)}$

$$\Delta \bar{F}_\mu(Y_{n_v}^k) = \bar{F}_\mu(Y_{n_v}^k) - \int_{\Omega_{\mu,0}} F_\mu^{(0)}(Y_{n_v}^k) dv \quad \text{for } k \in \mathbb{Z}_{n_v}^d. \quad (3.52)$$

For the first Newton iteration, equilibrium reads

$$[G * P_\mu] \left(Y_{n_v}^k, F_\mu^{(0)}(Y_{n_v}^k) + \Delta \bar{F}_\mu(Y_{n_v}^k) + \delta F_\mu(Y_{n_v}^k) \right) = \mathbf{0} \quad \text{for } k \in \mathbb{Z}_{n_v}^d. \quad (3.53)$$

Linearization of (3.53) results in

$$\begin{aligned} [G * K^{(0)}] \left(Y_{n_v}^k, F_\mu^{(0)}(Y_{n_v}^k) \right) : \delta F_\mu(Y_{n_v}^k) = \\ - [G * K^{(0)}] \left(Y_{n_v}^k, F_\mu^{(0)}(Y_{n_v}^k) \right) : \Delta \bar{F}_\mu(Y_{n_v}^k) \quad \text{for } k \in \mathbb{Z}_{n_v}^d, \end{aligned} \quad (3.54)$$

where $K^{(0)}$ is the constitutive tangent about $F_\mu^{(0)}$. Note that use has been made of the fact that $F_\mu^{(0)}$ is in equilibrium, i.e. that $[G * P_\mu] \left(Y_{n_v}^k, F_\mu^{(0)} \right) = \mathbf{0}$. After solving the system in Equation (3.54) one sets

$$F_\mu^{(1)}(Y_{n_v}^k) = F_\mu^{(0)}(Y_{n_v}^k) + \Delta \bar{F}_\mu(Y_{n_v}^k) + \delta F_\mu(Y_{n_v}^k) \quad \text{for } k \in \mathbb{Z}_{n_v}^d, \quad (3.55)$$

and proceed normally. It is thereby important to point out that the definition of \mathbb{G} ensures that the mean

$$\int_{\Omega_{\mu,0}} \delta F dv = \mathbf{0}. \quad (3.56)$$

All iterations thus satisfy the prescribed $\bar{\mathbf{F}}$ exactly. The interpretation of Equation (3.54) is that, by solving the linear system, the macroscopic deformation, $\Delta\bar{\mathbf{F}}$, is distributed over this microstructure using the tangent $\mathbf{K}^{(0)}$, which contains the microstructural heterogeneity. Equation (3.54) therefore has strong similarities with the application of essential (Dirichlet) boundary conditions in the Finite Element Method.

Box 3.2 presents the pseudo-code for the Newton-CG scheme used to solve the non-linear equilibrium equations at finite strains.

Box 3.2: Pseudo-code for the Newton-CG algorithm solving the equilibrium problem for non-linear behavior at finite strains.

- (i) Initialize $\mathbf{F}_\mu^{(0)}(\mathbf{Y}_{n_v}^{(k)}) = \mathbf{I}$ for $\mathbf{k} \in \mathbb{Z}_{n_v}^d$ and history variables
- (ii) Enter increment loop
 - (1) Set Newton counter to zero: $i = 0$
 - (2) Enter Newton loop
 - (a) Compute the constitutive response (material dependent): $\mathbf{F}_\mu^{(i)} \rightarrow \mathbf{K}^{(i)}, \mathbf{P}_\mu^{(i)}$
 - (b) According to
 - If $i = 0$ then enforce the boundary condition:
Solve

$$[\mathbf{G} * \mathbf{K}^{(0)}] \left(\mathbf{Y}_{n_v}^{\mathbf{k}}, \mathbf{F}_\mu^{(0)}(\mathbf{Y}_{n_v}^{\mathbf{k}}) \right) : \delta \mathbf{F}_\mu(\mathbf{Y}_{n_v}^{\mathbf{k}}) =$$

$$- [\mathbf{G} * \mathbf{K}^{(0)}] \left(\mathbf{Y}_{n_v}^{\mathbf{k}}, \mathbf{F}_\mu^{(0)}(\mathbf{Y}_{n_v}^{\mathbf{k}}) \right) : \Delta \bar{\mathbf{F}}(\mathbf{Y}_{n_v}^{\mathbf{k}}) \quad \text{for } \mathbf{k} \in \mathbb{Z}_{n_v}^d,$$

$$\mathbf{F}_\mu^{(1)}(\mathbf{Y}_{n_v}^{\mathbf{k}}) = \mathbf{F}_\mu^{(0)}(\mathbf{Y}_{n_v}^{\mathbf{k}}) + \Delta \bar{\mathbf{F}}_\mu(\mathbf{Y}_{n_v}^{\mathbf{k}}) + \delta \mathbf{F}_\mu(\mathbf{Y}_{n_v}^{\mathbf{k}}) \quad \text{for } \mathbf{k} \in \mathbb{Z}_{n_v}^d,$$
 - else, enforce the equilibrium iteration

$$[\mathbf{G} * \mathbf{K}^{(i)}] \left(\mathbf{Y}_{n_v}^{\mathbf{k}}, \mathbf{F}_\mu^{(i)}(\mathbf{Y}_{n_v}^{\mathbf{k}}) \right) : \delta \mathbf{F}_\mu(\mathbf{Y}_{n_v}^{\mathbf{k}}) =$$

$$- [\mathbf{G} * \mathbf{P}_\mu^{(i)}] \left(\mathbf{Y}_{n_v}^{\mathbf{k}}, \mathbf{F}_\mu^{(i)}(\mathbf{Y}_{n_v}^{\mathbf{k}}) \right) \quad \text{for } \mathbf{k} \in \mathbb{Z}_{n_v}^d.$$

$$\mathbf{F}_\mu^{(i+1)}(\mathbf{Y}_{n_v}^{\mathbf{k}}) = \mathbf{F}_\mu^{(i)}(\mathbf{Y}_{n_v}^{\mathbf{k}}) + \delta \mathbf{F}_\mu(\mathbf{Y}_{n_v}^{\mathbf{k}}) \quad \text{for } \mathbf{k} \in \mathbb{Z}_{n_v}^d,$$
 - (c) If the desired accuracy η^{NW} has not been reached, update index $i = i + 1$ and go to (a)
 - (3) Store the converged state $\mathbf{F}_\mu^{(i+1)}$ and the history variables, set $\mathbf{F}_\mu^{(0)} = \mathbf{F}_\mu^{(i+1)}$, and go to (1)

3.8 Convergence criteria

Two different convergence criteria are considered in this work and described in what follows. They include a criterion for the Conjugate Gradient procedure (interior loop) and a criterion for the Newton-Raphson procedure (exterior loop). Let i and j be the current Newton and Conjugate Gradient iteration steps, respectively.

Criterion I Criterion I follows from the most common criterion for the Conjugate Gradient. Since equilibrium is described by Equation (??), repeated here for clarity sake,

$$\mathbf{G} * \boldsymbol{\sigma}_\mu = 0, \quad (3.57)$$

the linearized version reads

$$\mathbf{G} * \boldsymbol{\sigma}_\mu^{(i)} + [\mathbf{G} * \mathbf{K}^{(i)}] : \delta \tilde{\boldsymbol{\epsilon}}_\mu^{(i+1)} = 0. \quad (3.58)$$

Thus, the Conjugate Gradient will converge only when

$$\frac{\|[\mathbf{G} * \mathbf{K}^{(i)}] : \delta \tilde{\boldsymbol{\epsilon}}_\mu^{(i+1)} + \mathbf{G} * \boldsymbol{\sigma}_\mu^{(i)}\|}{\|\mathbf{G} * \boldsymbol{\sigma}_\mu^{(i)}\|} < \eta^{\text{CG}}, \quad (3.59)$$

using as the reference value $\mathbf{G} * \boldsymbol{\sigma}_\mu^{(i)}$.

Regarding the Newton-Raphson procedure, the tangent stiffness is updated and the same expression is used, such that the scheme has converged only when

$$\frac{\|[\mathbf{G} * \mathbf{K}^{(i+1)}] : \delta \tilde{\boldsymbol{\epsilon}}_\mu^{(i+1)} + \mathbf{G} * \boldsymbol{\sigma}_\mu^{(i)}\|}{\|\mathbf{G} * \boldsymbol{\sigma}_\mu^{(i)}\|} < \eta^{\text{NW}}. \quad (3.60)$$

The application of this criterion to the case of large strain is straightforward, needing only the small strain tensor and the Cauchy stress to be replaced by the deformation gradient the first Piola-Kirchhoff stress tensor, respectively.

Criterion II Criterion II uses the consecutive values of the stress tensor to ascertain if both procedure have converged.

For the Conjugate Gradient it reads

$$\frac{\|\boldsymbol{\sigma}_\mu^{(i,j)} - \boldsymbol{\sigma}_\mu^{(i,j+1)}\|}{\|\boldsymbol{\sigma}_\mu^{(i,j+1)}\|} < \eta^{\text{CG}}, \quad (3.61)$$

where the $\boldsymbol{\sigma}_\mu^{(i,j+1)}$ is computed as

$$\boldsymbol{\sigma}_\mu^{(i,j+1)} = \boldsymbol{\sigma}_\mu^{(i,j)} + \mathbf{K}^{(i)} \delta \tilde{\boldsymbol{\epsilon}}_\mu^{(i+1,j)}. \quad (3.62)$$

For the Newton-Raphson procedure, the consecutive values for the stress in the current and the next iteration are used as follows

$$\frac{\|\boldsymbol{\sigma}_\mu^{(i+1)} - \boldsymbol{\sigma}_\mu^{(i)}\|}{\|\boldsymbol{\sigma}_\mu^{(i+1)}\|} < \eta^{\text{NW}}. \quad (3.63)$$

Chapter 4

Numerical Results - Elasticity

In the following chapter, results pertaining to elasticity are presented. The validation of the FFT-based Galerkin formulation is performed on elastic materials at small strains and large strains. At large strains two different models are considered, the Saint Venant-Kirchhoff constitutive model and the Hencky constitutive model.

It is important to remark that all the numerical results shown in this chapter are obtained in the same machine with the specifications provided in Table 5.1. Unless otherwise stated, each numerical simulation is performed only with 1 CPU core.

Table 4.1: Specifications of the numerical testing machine.

CPU	Model	2 × Intel Xeon E5-2650 v4
	Microarchitecture	Broadwell
	Base/Max Frequency	2.20/2.90GHz
	Num. of cores/threads	24/48(2 × 12/24)
	L1 Cache	718KiB(2 × 384KiB)
	L2 Cache	6MiB(2 × 3MiB)
	L3 Cache	60MiB(2 × 30MiB)
	Numerical features	SSE3 SSSE3 AVX2
Memory	Capacity	128 GB(8 × 16 GB)
	Specification	DDR4 @ 2400MHz

4.1 Material characterization

In order to perform several numerical applications in a systematic way, the same microstructures are considered throughout the entire chapter. Without any loss of generality in what concerns the objectives of the following studies, two types of periodic microstructures are addressed following [Ferreira \(2020\)](#):

2D microstructure Fiber-reinforced composite characterized by unidirectional

circular cross-section fibers (phase 2, $f = 30\%$) randomly distributed and embedded in a matrix (phase 1, $f = 70\%$)¹ - see Figure 4.1(a);

3D microstructure Particle-reinforced composite characterized by spherical particles (phase 2, $f = 20\%$) randomly distributed and embedded in a matrix (phase 1, $f = 80\%$) see Figure 4.1(b).

The assumed material properties for each phase are presented in Table 4.2. At small strains, the material considered is linear elastic and at large strains, two constitutive models are considered. The Saint Venant-Kirchhoff and Hencky constitutive models, both to be introduced next.

Table 4.2: Material properties for both fiber-reinforced (2D) and particle-reinforced (3D) composites.

Property	SI Units	Phase 1	Phase 2
E	Pa	100×10^6	500×10^6
ν	—	0.30	0.19

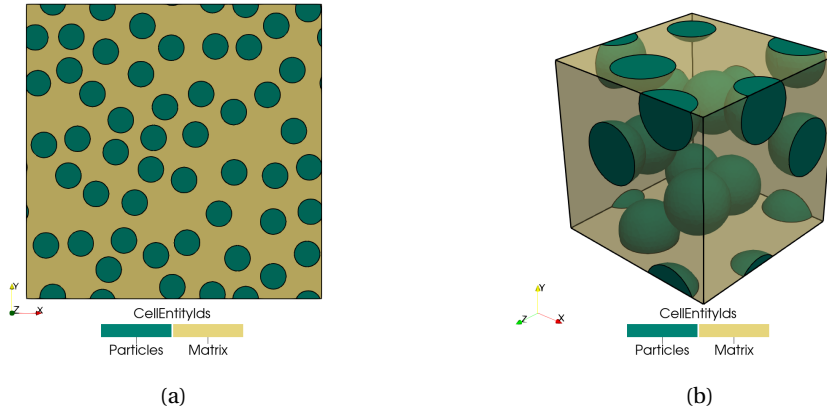


Figure 4.1: Dual phased heterogeneous materials microstructure: (a) Fiber-reinforced composite (randomly distributed unidirectional circular cross-section fibers, $f = 30\%$) - 2D RVE; (b) Particle-reinforced composite (randomly distributed particles, $f = 20\%$) - 3D RVE.

4.1.1 Saint Venant-Kirchhoff model

One of the simplest constitutive models to consider is a hyper-elastic model defined in the reference configuration. Note that the problem is still non-linear because of the geometric nonlinearity. According to [De Geus et al. \(2017\)](#) it can be described as follows.

¹This type of microstructure is suitable to be modeled in plane strain conditions by considering any transversal plane relative to the fibers direction.

Constitutive model The model is defined in the undeformed configuration and it involves a linear relation between the second Piola-Kirchhoff stress \mathbf{S} and the Green-Lagrange strain \mathbf{E}

$$\mathbf{S} = \mathbf{D}^e : \mathbf{E}, \quad (4.1)$$

wherein \mathbf{D}^e is the standard fourth-order elastic stiffness tensor

$$\mathbf{D}^e \equiv \lambda \mathbf{I} \otimes \mathbf{I} + 2\mu \mathbf{I}_S, \quad (4.2)$$

with Lamé's constants λ and μ . In terms of Young's modulus, E , and Poisson's ratio, ν , they read

$$\lambda = \frac{E\nu}{(1+\nu)(1-2\nu)}, \quad \mu = \frac{E}{2(1+\nu)}. \quad (4.3)$$

Furthermore, \mathbf{I} is the second-order identity tensor and \mathbf{I}_S is the fourth-order symmetrization tensor².

The connection to the deformation gradient tensor \mathbf{F} and the first Piola-Kirchhoff stress \mathbf{P} is made by the definition of the Green-Lagrange strain

$$\mathbf{E} = \frac{1}{2} (\mathbf{F}^T \mathbf{F} - \mathbf{I}), \quad (4.4)$$

and of the first Piola-Kirchhoff stress

$$\mathbf{P} = \mathbf{F} \mathbf{S}. \quad (4.5)$$

Consistent tangent The constitutive model is linearized in the reference configuration in accordance with Equation (3.50). Its derivation is straightforward. The first step is to linearize the stress relation in Equation (4.5), leading to

$$\delta \mathbf{P}^T = \mathbf{S}^{(i)} \delta \mathbf{F}^T + \mathbf{I}_{RT} : (\mathbf{F}^{(i)} \delta \mathbf{S}), \quad (4.6)$$

wherein \mathbf{I}_{RT} is the fourth-order right-transposed identity tensor³. The constitutive model in Equation (4.1) is already linear. Combined with the linearization of the Green-Lagrange strain one obtains

$$\delta \mathbf{S} = \mathbf{D}^e : \left(\mathbf{I}^S \mathbf{F}^{(i)T} \right) : \delta \mathbf{F}. \quad (4.7)$$

The expression of the tangent stiffness follows by combining Equations (4.6) and (4.7) to obtain

$$\mathbf{A}^{(i)} = \mathbf{S}^{(i)} \mathbf{I} + \mathbf{I}_{RT} : \left(\mathbf{F}^{(i)} \mathbf{D}^e \mathbf{F}^{(i)T} \right) : \mathbf{I}_{RT}, \quad (4.8)$$

whereby the right-symmetry of \mathbf{D}^e has been used to absorb \mathbf{I}_S .

4.1.2 Hencky model

The Hencky model is the finite logarithmic strain-based extension of the standard linear elastic material. According to [de Souza Neto et al. \(2008\)](#) it can be described as follows.

²The fourth order symmetrization tensor is defined as $(\mathbf{I}_S)_{ijkl} = \frac{1}{2}(\delta_{ik}\delta_{jl} + \delta_{il}\delta_{jk})$.

³The fourth-order right-transposed identity tensor is defined as $(\mathbf{I}_{RT})_{ijkl} = \delta_{ik}\delta_{jl}$.

Constitutive model Let ε be the Eulerian logarithmic strain tensor

$$\varepsilon \equiv \ln \mathbf{V} = \frac{1}{2} \ln \mathbf{B}. \quad (4.9)$$

The Hencky strain-energy function is defined in compact form as

$$\bar{\rho} \psi(\varepsilon) = \frac{1}{2} \varepsilon : \mathbf{D}^e : \varepsilon, \quad (4.10)$$

where \mathbf{D}^e has the format of the infinitesimal isotropic elasticity tensor

$$\mathbf{D}^e \equiv 2G\mathbf{I}_S + \left(K - \frac{2}{3}G\right) \mathbf{I} \otimes \mathbf{I}. \quad (4.11)$$

The above strain-energy renders the following linear relationship between the Kirchhoff stress and the Eulerian logarithmic strain

$$\boldsymbol{\tau} = \bar{\rho} \frac{\partial \psi}{\partial \varepsilon} = \mathbf{D}^e : \varepsilon, \quad (4.12)$$

which has the same functional format as the infinitesimal linear elastic stress-strain relation.

Consistent tangent Under material isotropy, where $\boldsymbol{\tau}$ can be expressed as a function of \mathbf{B} only, the spatial elasticity tensor can be equivalently represented as

$$\mathbf{a} = \frac{2}{J} \frac{\partial \boldsymbol{\tau}}{\partial \mathbf{B}} \mathbf{B} - \mathbf{I}_{RT} \boldsymbol{\sigma}. \quad (4.13)$$

As the Kirchhoff stress for the Hencky material is a linear function of the logarithmic Eulerian strain which, through its definition (4.9), is a function of \mathbf{B} , the derivative $\partial \boldsymbol{\tau} / \partial \mathbf{B}$ can be derived by a straightforward application of the chain rule to (4.12). This gives

$$\frac{\partial \boldsymbol{\tau}}{\partial \mathbf{B}} = \frac{\partial \boldsymbol{\tau}}{\partial \varepsilon} : \frac{\partial \varepsilon}{\partial \mathbf{B}} = \frac{1}{2} \mathbf{D}^e : \mathbf{L}, \quad (4.14)$$

where

$$\mathbf{L} \equiv \frac{\partial (\ln \mathbf{B})}{\partial \mathbf{B}}, \quad (4.15)$$

is the derivative of the tensor logarithm function evaluated at \mathbf{B} .

In order to derive a compact expression for the Hencky elasticity tensor, we note that (4.13) is equivalent to

$$\mathbf{a} = \frac{1}{J} \frac{\partial \boldsymbol{\tau}}{\partial \mathbf{B}} : \mathbf{B} - \mathbf{I}_{RT} \boldsymbol{\sigma} \quad (4.16)$$

where we have defined the fourth-order tensor \mathbf{B} by

$$\mathbf{B} \equiv 2\mathbf{I}_S \mathbf{B}. \quad (4.17)$$

Finally, formula (4.16) together with (4.14) yields the following expression for the Hencky spatial elasticity tensor

$$\mathbf{a} = \frac{1}{2J} \mathbf{D}^e : \mathbf{L} : \mathbf{B} - \mathbf{I}_{RT} \boldsymbol{\sigma}, \quad (4.18)$$

which has a particularly simple format. The pull-back(?) to the material configuration is given by

$$\mathbf{A}^{(i)} = \mathbf{F}^{(i)-1} \left(\frac{1}{2} \mathbf{D}^e : \mathbf{L}^{(i)} : \mathbf{B}^{(i)} - \mathbf{I}_{RT} \boldsymbol{\tau}^{(i)} \right) \mathbf{F}^{(i)-T}, \quad (4.19)$$

reintroducing the dependency on the current Newton iteration (i).

4.2 Comparison between FFT and FEM-based homogenization

To better gauge the accuracy and efficiency of the FFT-based Galerkin formulation, some numerical simulations are performed. Their goals is to (1) validate the implementation of the FFT-based homogenization Galerkin scheme (Vondřejc et al., 2014; Zeman et al., 2017; De Geus et al., 2017), (2) compare the accuracy and computational performance between the FFT, basic (Moulinec and Suquet, 1994) and Galerkin formulation, and FEM-based homogenization approaches and (3) choose the suitable spatial discretization refinement to evaluate the microstructures in Figure 4.1.

Concerning the FFT-based homogenization, the same discretization is performed in the different problem dimensions ($n_{v,1} = n_{v,2} = n_{v,3}$). In order to generate the FEM finite element meshes, the FFT-FEM mesh conversion strategy adopted is to convert the pixels (2D) and voxels (3D) into quadrilateral (2D) and brick (3D) finite elements. It is employed with both linear (QUAD4, HEXA8) and quadratic finite elements (QUAD8, HEXA20) such that $n_e = n_v$. Moreover, given the solver library available in LINKS, two types of solvers are considered in the FEM-based homogenization simulations: the direct solver MKL PARDISO (Schenk et al., 2001; Schenk and Gärtner, 2004) and the iterative solver WSMP (Watson Sparse Matrix Package) (Gupta, 2002a,b) with an SSOR (Symmetric Successive Over-relaxation) preconditioner. Extensive preliminary research has shown that these are the overall (solver time and memory footprint) best direct and iterative solvers available in Links (Cardoso Coelho, 2019).

4.2.1 Small strain

Comparison of the convergence criteria The following numerical results are obtained to provide a better understanding of the differences in efficiency and accuracy between the two convergence criteria detailed in Section 3.8.

Both phases are assumed linear elastic (see Table 4.2 for the properties), periodic boundary conditions are adopted and the following macroscale strain loading case is considered

$$\text{uniaxial: } \boldsymbol{\varepsilon} = \begin{bmatrix} 5 & 0 & 0 \\ 0 & 0 & 0 \\ 0 & 0 & 0 \end{bmatrix} \times 10^{-3} \quad (4.20)$$

being enforced in a single load increment. Note that in the 2D plane strain case, only the inplane O_{xy} macroscale strain components are enforced.

The numerical results of the fiber-reinforced linear elastic composite equilibrium problem using the two criteria under analysis are shown in Figure 4.2 for the uniaxial loading case. Figure 4.2(a) shows that both FFT techniques converge to the same value at approximately the same rate as a function of the number of voxels in the discretization. Also, no noticeable difference can be seen between the two convergence criteria considered. Regarding the CPU time expended to reach an error of 1×10^{-6} , presented in Figure 4.2(b), Criterion I leads to faster convergence. This effect is stronger for the FFT Basic scheme.

The numerical results of the particle-reinforced linear elastic composite equilibrium problem are shown in Figure 4.3 for the uniaxial loading case. The results mirror the ones found for the two-dimensional example. Figure 4.3(a) shows that both FFT techniques converge to the same value at approximately the same rate as a function of the number of voxels in the discretization. Also, no noticeable difference

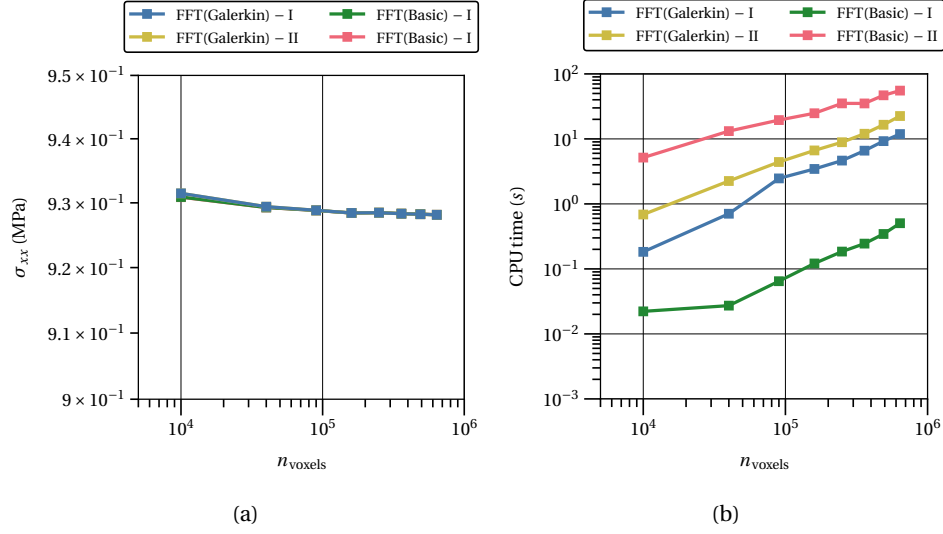


Figure 4.2: Comparison between the Criterion I and II for FFT-based homogenization approaches, Galerkin and Basic, in the solution of the fiber-reinforced linear elastic composite equilibrium problem under uniaxial strain loading conditions: (a) Homogenized stress; (b) Computational time.

can be seen between the two convergence criteria considered. Regarding the CPU time expended to reach an error of 1×10^{-5} , presented in Figure 4.3(b), Criterion I leads to faster convergence. This effect is stronger for the FFT Basic scheme.

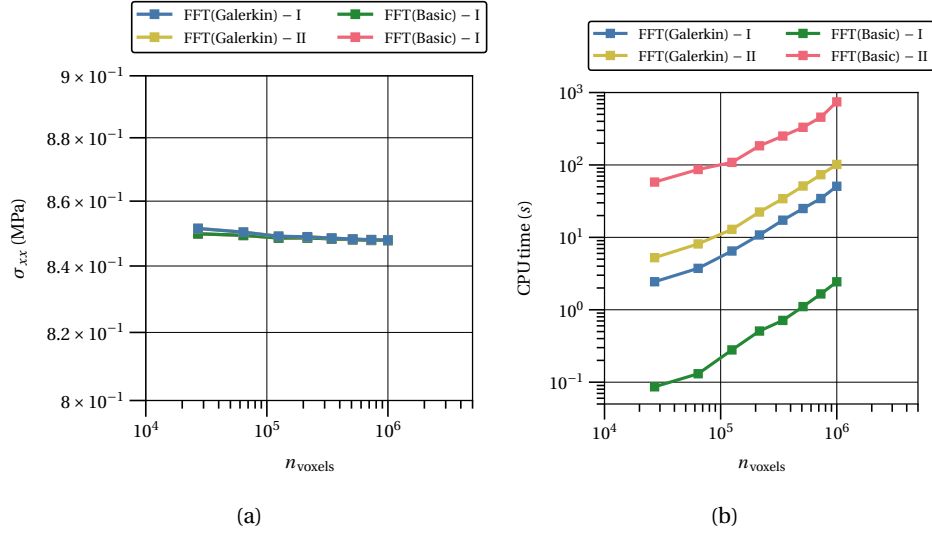


Figure 4.3: Comparison between the Criterion I and II for FFT-based homogenization approaches, Galerkin and Basic, in the solution of the particle-reinforced linear elastic composite equilibrium problem under uniaxial strain loading conditions: (a) Homogenized stress; (b) Computational time.

Accuracy validation Both phases are assumed linear elastic (see Table 4.2 for the properties), periodic boundary conditions are adopted and the following two macroscale strain loading cases are considered

$$\text{uniaxial: } \boldsymbol{\varepsilon} = \begin{bmatrix} 5 & 0 & 0 \\ 0 & 0 & 0 \\ 0 & 0 & 0 \end{bmatrix} \times 10^{-3}, \quad \text{pure shear: } \boldsymbol{\varepsilon} = \begin{bmatrix} 0 & 5 & 5 \\ 5 & 0 & 5 \\ 5 & 5 & 0 \end{bmatrix} \times 10^{-3}, \quad (4.21)$$

being enforced in a single load increment. Note that in the 2D plane strain case, only the inplane O_{xy} macroscale strain components are enforced. The convergence criterion used is Criterion II, as described in Section 3.8.

The numerical results of the fiber-reinforced linear elastic composite equilibrium problem are shown in Figures 4.4 and ?? for the uniaxial and pure shear loading cases, respectively. In both cases there is an excellent agreement between the FFT and FEM-based homogenization solutions concerning both the homogenized response (see Figures 4.4(a) and 4.5(a)) and the local strain fields (see Figures 4.4(c) and 4.5(c)). In terms of computational performance, Figures 4.4(b) and 4.5(b) show that the FFT-based homogenization Galerkin scheme outperforms the FEM-based homogenization with speedups of around 2 relative to the direct solver with linear finite elements. There is however a caveat, regarding this direct comparison. The Python libraries used in the implementation of the FFT-based homogenization Galerkin scheme are parallelized and used all the cores available in the machine at the time. On the other hand, the FEM simulations are run using only one core. When compared with the FFT-based homogenization basic scheme, the CPU time expended differs by more than an order of magnitude, with the Galerkin scheme being slower.

The numerical results of the particle-reinforced linear elastic composite equilibrium problem are shown in Figures 4.6 and 4.7 for the uniaxial and pure shear

loading cases, respectively. Once again there is an excellent agreement between the FFT and FEM-based homogenization solutions concerning both the homogenized response (see Figures 4.6(a) and 4.7(a)) and the local strain fields (see Figures 4.6(c) and 4.7(c)). In terms of computational performance, Figures 4.6(b) and 4.7(b) show that the FFT-based homogenization Galerkin scheme outperforms the FEM-based homogenization with speedups ranging from around 10 and 100 relative to the iterative solver with linear and quadratic finite elements, respectively. The same remark concerning the number of cores used in each method mentioned previously also applies here. Comparing the two FFT-based schemes, the basic scheme is faster by an order of magnitude than the Galerkin scheme. Adding to this, the 3D cases highlight another important aspect concerning FEM-based homogenization. When attempting to run the direct solver simulations with $n_e = 80 \times 80 \times 80$ (linear finite element mesh) and $n_e = 50 \times 50 \times 50$ (quadratic finite element mesh) the memory required to build the global tangent stiffness matrix (stored in compressed sparse row (CSR) format) exceeds the available 128 GB! Despite reaching a significantly lower peak memory than the direct solver, the iterative solver suffered from the same limitation for a simulation over $n_e = 100 \times 100 \times 100$ (linear finite element mesh) and $n_e = 70 \times 70 \times 70$ (quadratic finite element mesh). In comparison, the FFT-based homogenization memory footprint is almost negligible as it does not require the computation of a global tangent stiffness matrix.

From the results present, a few conclusions and remarks are in order:

- The FFT-based homogenization Galerkin scheme implementation is validated as solutions obtained (both homogenized results and local fields) are in excellent agreement with ones obtained with the FEM-based homogenization from LINKS and the FFT-based homogenization basic scheme;
- In the linear elastic regime, the FFT-based homogenization Galerkin scheme outperforms the FEM-based homogenization both in terms of speed and memory footprint. However, it must be kept in mind that some of the Python libraries employed in the implementation of the FFT-based homogenization Galerkin scheme are parallelized and only one core is used in the LINKS simulations.
- In the linear elastic regime, the FFT-based homogenization basic scheme outperforms the FFT-based homogenization Galerkin scheme in terms of CPU time expended. Yet, consider that the implementation of the basic scheme used in the comparison has already undergone some performance optimization. This is not the case for the Galerkin scheme.
- Given the solution convergence with the increasing sampling/meshing refinement, the spatial discretizations of $n_v = 600 \times 600$ (fiber-reinforced composite 2D RVE) and $n_v = 70 \times 70 \times 70$ (particle-reinforced composite 3D RVE) are considered hereafter unless otherwise stated;
- In the following numerical studies, the reference DNS solution is obtained considering quadratic finite elements (QUAD8 and HEXA20) and the fastest solver time (MKL PARDISO in the 2D case and WSMP-SSOR in the 3D case) unless otherwise stated.

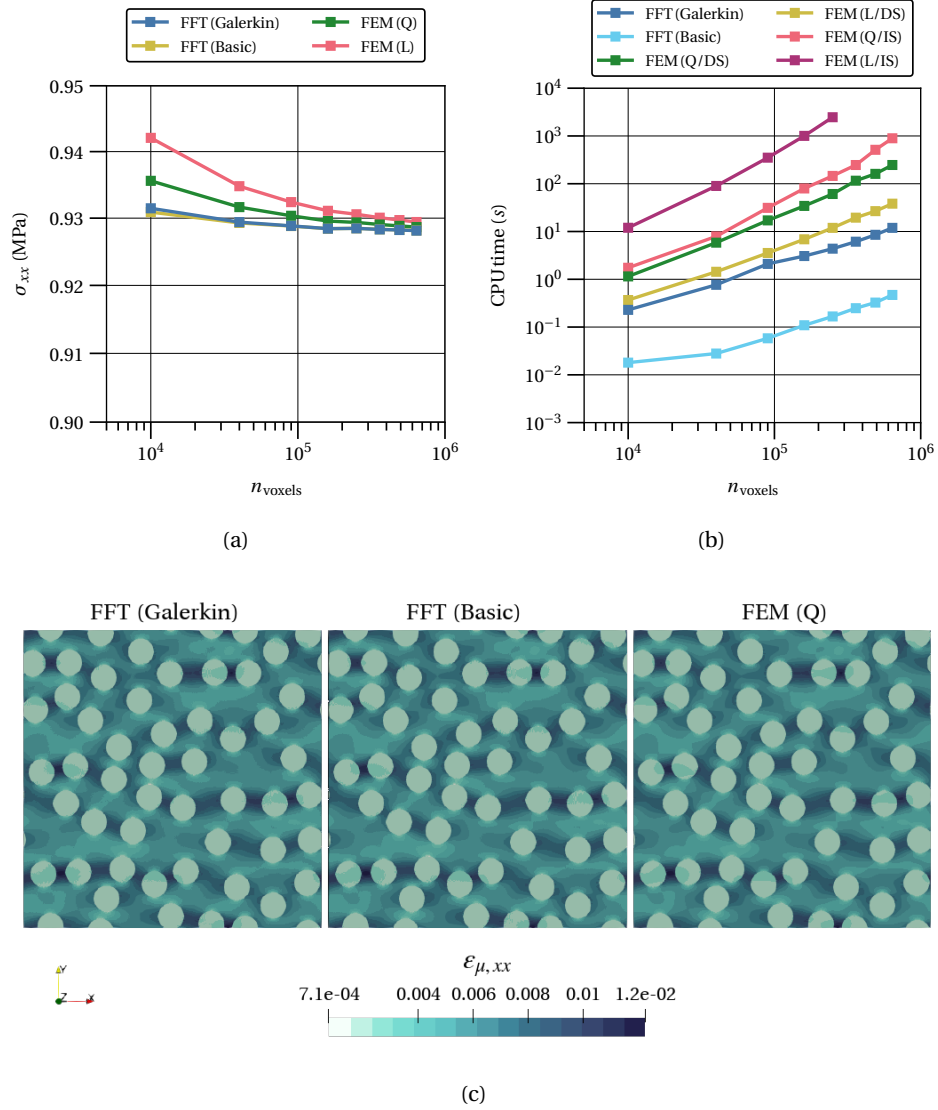


Figure 4.4: Comparison between the FFT and FEM-based homogenization approaches in the solution of the fiber-reinforced linear elastic composite equilibrium problem under pure shear strain loading conditions: (a) Homogenized stress; (b) Computational time; (c) Local strain field ($n_v = 600 \times 600$ discretization). Notation: linear element (L), quadratic element (Q), direct solver (DS) and iterative solver (IS)

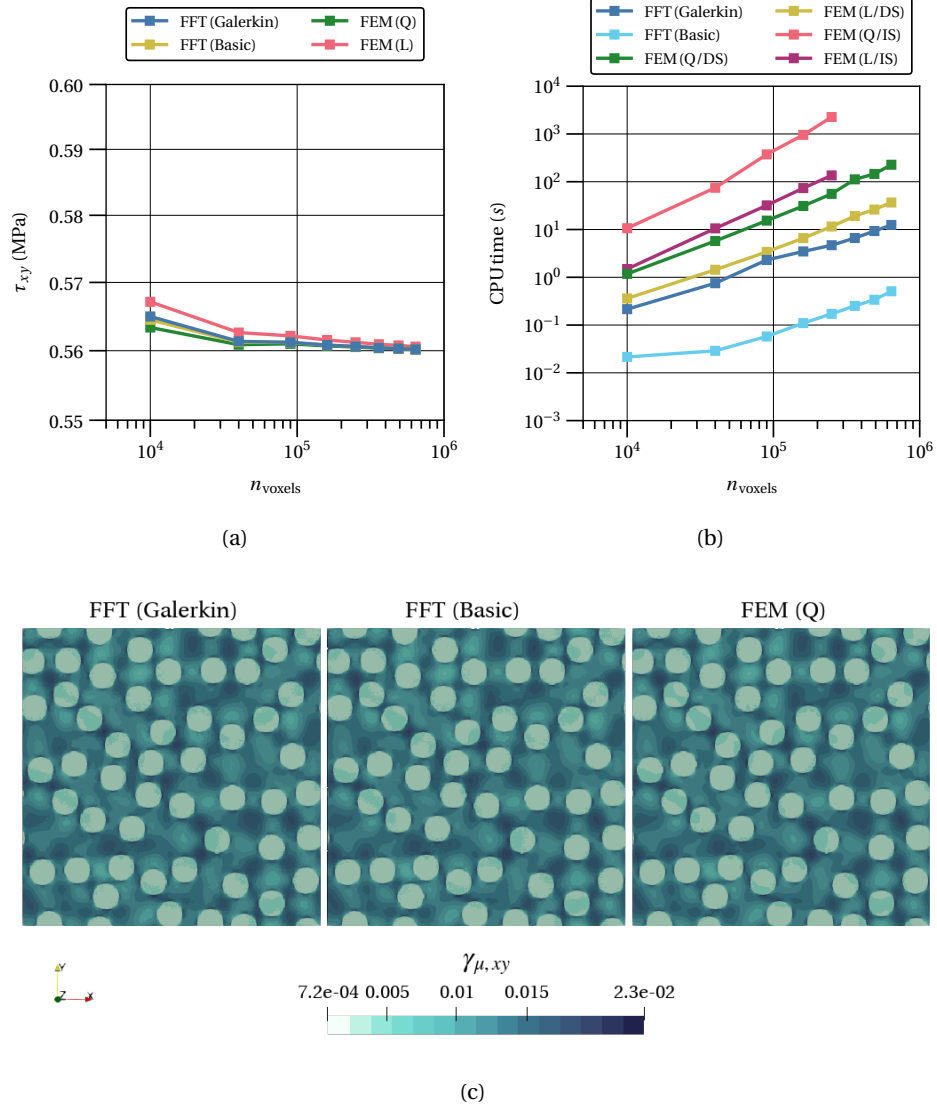


Figure 4.5: Comparison between the FFT and FEM-based homogenization approaches in the solution of the fiber-reinforced linear elastic composite equilibrium problem under pure shear strain loading conditions: (a) Homogenized stress; (b) Computational time; (c) Local strain field ($n_v = 600 \times 600$ discretization). Notation: linear element (L), quadratic element (Q), direct solver (DS) and iterative solver (IS)

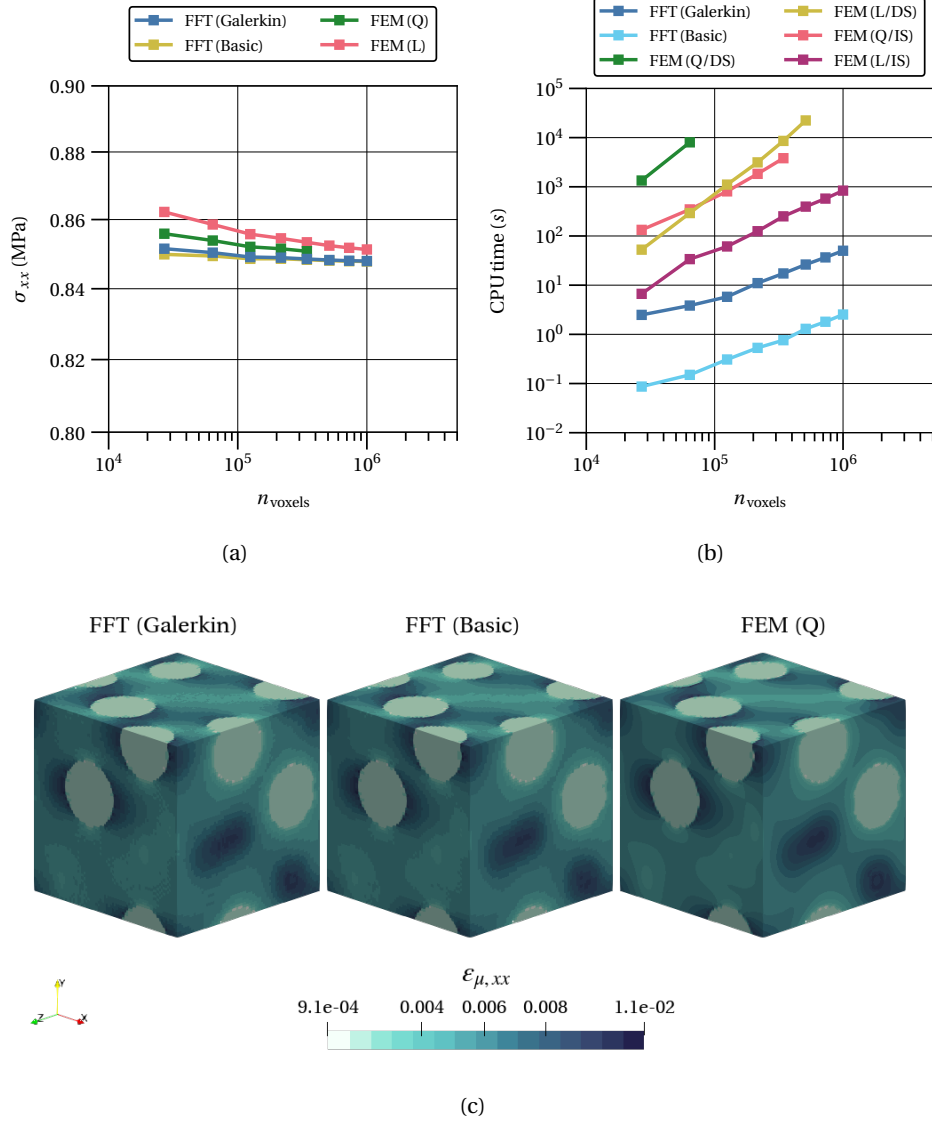


Figure 4.6: Comparison between the FFT and FEM-based homogenization approaches in the solution of the particle-reinforced linear elastic composite equilibrium problem under normal strain loading conditions: (a) Homogenized stress; (b) Computational time; (c) Local strain field ($n_v = 70 \times 70 \times 70$ discretization). Notation: linear element (L), quadratic element (Q), direct solver (DS) and iterative solver (IS)

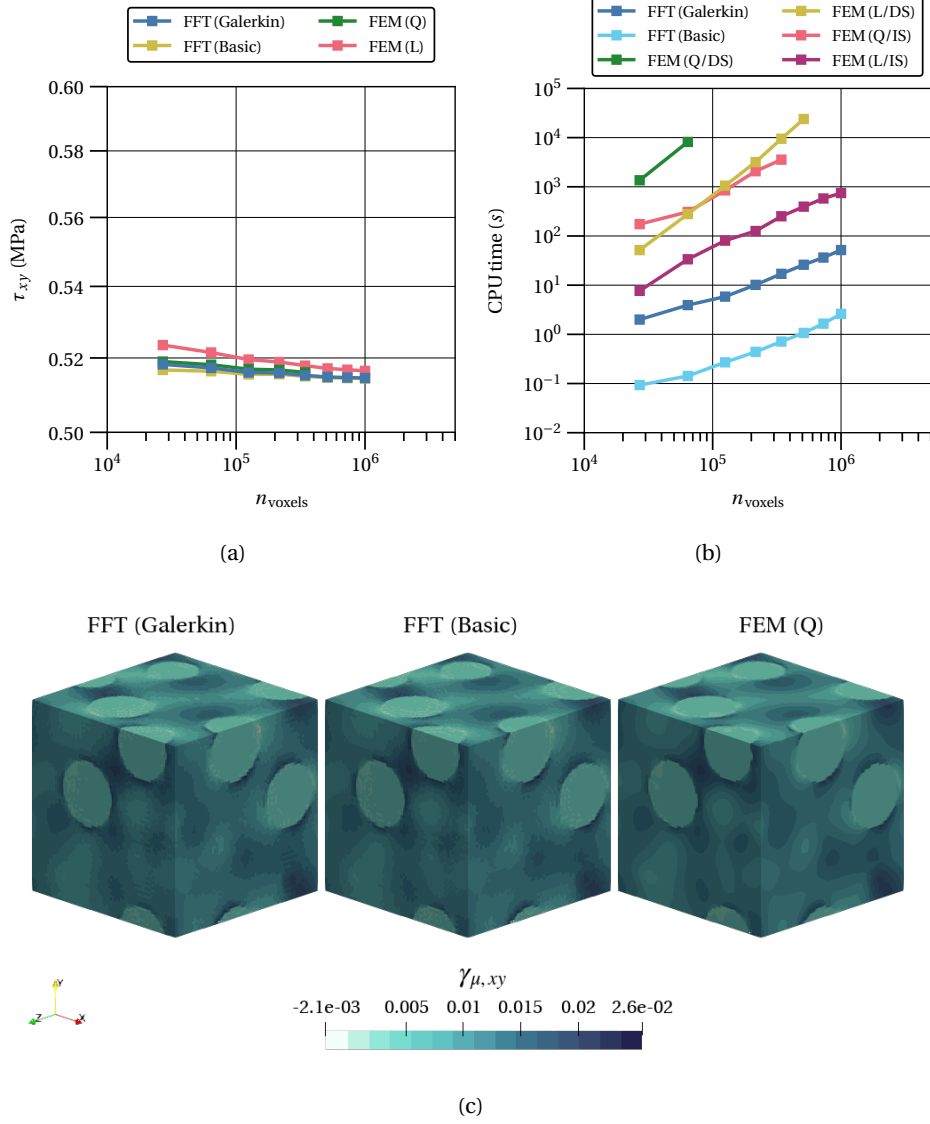


Figure 4.7: Comparison between the FFT and FEM-based homogenization approaches in the solution of the fiber-reinforced linear elastic composite equilibrium problem under pure shear strain loading conditions: (a) Homogenized stress; (b) Computational time; (c) Local strain field ($n_v = 70 \times 70 \times 70$ discretization). Notation: linear element (L), quadratic element (Q), direct solver (DS) and iterative solver (IS).

Extreme stiffness ratios between phases The following set of results is presented to better comprehend the limitations of the FFT-based methods regarding the stiffness ratio between the phases, widely reported in the literature . As previously, FEM solutions are used as a comparison standard.

Both phases are assumed linear elastic having the same Poisson's ratio, $\nu = 0.3$. The Young modulus of the matrix is fixed at $E_1 = 100\text{MPa}$ and the ratio between the stiffness of the particles and the matrix, $K = E_1/E_2$, is made to vary from 10^{-6} to 10^4 in increments of $\times\sqrt{10}$. Periodic boundary conditions are adopted and the following macroscale strain loading case is considered

$$\text{uniaxial: } \boldsymbol{\epsilon} = \begin{bmatrix} 5 & 0 & 0 \\ 0 & 0 & 0 \\ 0 & 0 & 0 \end{bmatrix} \times 10^{-3}, \quad (4.22)$$

being enforced in a single load increment. Note that in the 2D plane strain case, only the inplane O_{xy} macroscale strain components are enforced.

The numerical results of the fiber-reinforced linear elastic composite equilibrium problem are shown in Figures 4.8 for the uniaxial loading case. There is an excellent agreement between the FFT and FEM-based homogenization solutions concerning the homogenized response as attested by Figure 4.8(a). In terms of computational performance, Figure 4.8(b) shows that the FFT-based homogenization Galerkin scheme outperforms the FEM-based homogenization with speedups from around 20 at low stiffness contrast to around 2 at the highest stiffness contrasts, both high and low, relative to the direct solver with linear finite elements. As before, the caveat regarding the parallelization of the Python libraries still applies. When compared with the FFT-based homogenization basic scheme, the CPU time expended differs from one to two orders of magnitude across the stiffness ranges considered, with the Galerkin scheme being slower. However, the basic scheme is unable to reach the preset tolerance (10^{-6}) for stiffness ratios beyond the range $[10^{-3}, 10^3]$.

Concerning the local field, an excellent agreement can be observed at both high ($K = E_1/E_2 = 10^4$) and low ($K = E_1/E_2 = 10^{-4}$) stiffness ratios in the matrix phase, as can be seen in Figures 4.9 and 4.10. There is also good agreement regarding the local field in the particle phase for the strain field at the low stiffness ratio and the stress field at the high stiffness ratio. On the other hand, the strain field at the low stiffness ratio and the strain field at the high stiffness ratio exhibit strong oscillations in the particle phase. Figure 4.11 provides a more detailed representation of the variation of the strain field $\epsilon_{\mu,xx}$ inside the particle phase at a stiffness ratio equal to 10^{-4} . This phenomenon is often denominated by "ringing" and is widely reported in the literature as being a consequence of very high or low stiffness ratios. The extreme values found in Figure 4.11(a) concerning the FFT Galerkin method for the local normal strain field, $\epsilon_{\mu,xx}$, at $y = 0$ and $0 \leq x \leq 0.2$, are not dissimilar to the extreme values present in FEM solution (see Figure 4.9(a)). However, looking at Figure 4.11(b), the extreme values of the local field at $y = 0$ and $0.45 \leq x \leq 0.55$ are now one order of magnitude larger than the ones in the FEM solution. This presents a clear error in the FFT-Galerkin solution for the local strain field inside the particles. The FFT-based basic scheme homogenization also presents this fragility. In closing, it bears mentioning that this does not affect the accuracy of the homogenized response.

The numerical results of the particle-reinforced linear elastic composite equilibrium problem are shown in Figures 4.12 for the uniaxial loading case. There is an excellent agreement between the FFT-based homogenization Galerkin scheme and

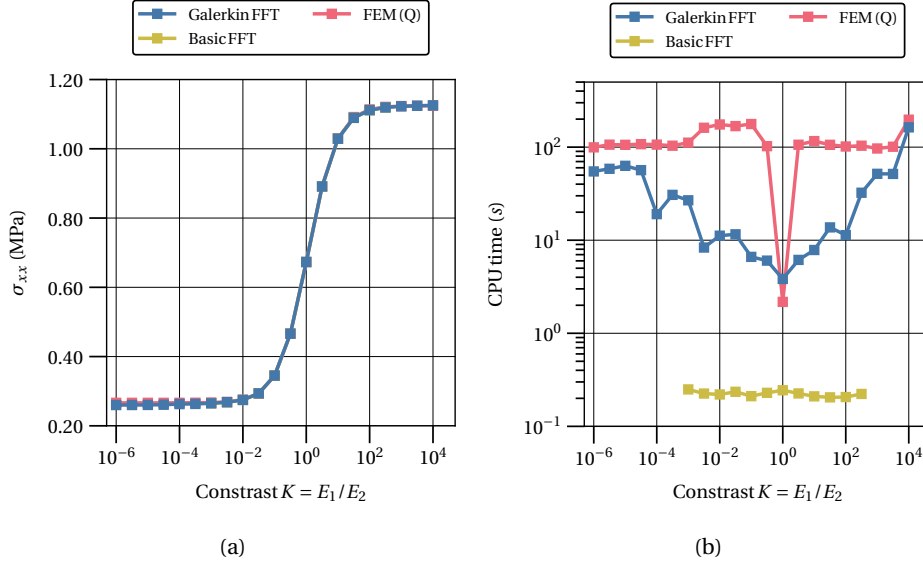


Figure 4.8: Comparison between the FFT and FEM-based homogenization approaches in the solution of the fiber-reinforced linear elastic composite equilibrium problem under normal strain loading conditions: (a) Homogenized stress; (b) Computational time; Notation: linear element (L), quadratic element (Q).

the FEM-based homogenization solutions concerning the homogenized response as attested by Figure 4.12(a). The same cannot be said for the FFT-based homogenization Galerkin scheme as the stiffness ratio becomes more extreme. In terms of computational performance, Figure 4.12(b) shows that the FFT-based homogenization Galerkin scheme outperforms the FEM-based homogenization with speedups from around 100 at minor stiffness contrast to around 3 at the lowest stiffness contrast, relative to the direct solver with linear finite elements. As before, the caveat regarding the parallelization of the Python libraries still applies. When compared with the FFT-based homogenization basic scheme, the CPU time expended differs from one to two orders of magnitude across the stiffness ranges considered, with the Galerkin scheme being slower. It must be added that for higher stiffness ratios the WSMP-SSOR solver is not able to converge.

Concerning the local field, an excellent agreement can be observed at both high ($K = E_1/E_2 = 10^{1.5}$) and low ($K = E_1/E_2 = 10^{-4}$) stiffness ratios in the matrix phase, as can be seen in Figures 4.13 and 4.14. There is also good agreement regarding the local field in the particle phase for the strain field at the low stiffness ratio and the stress field at the high stiffness ratio. On the other hand, the strain field at the low stiffness ratio and the strain field at the high stiffness ratio exhibit strong oscillations in the particle phase. This mirrors the previous results concerning two-dimensional microstructures.

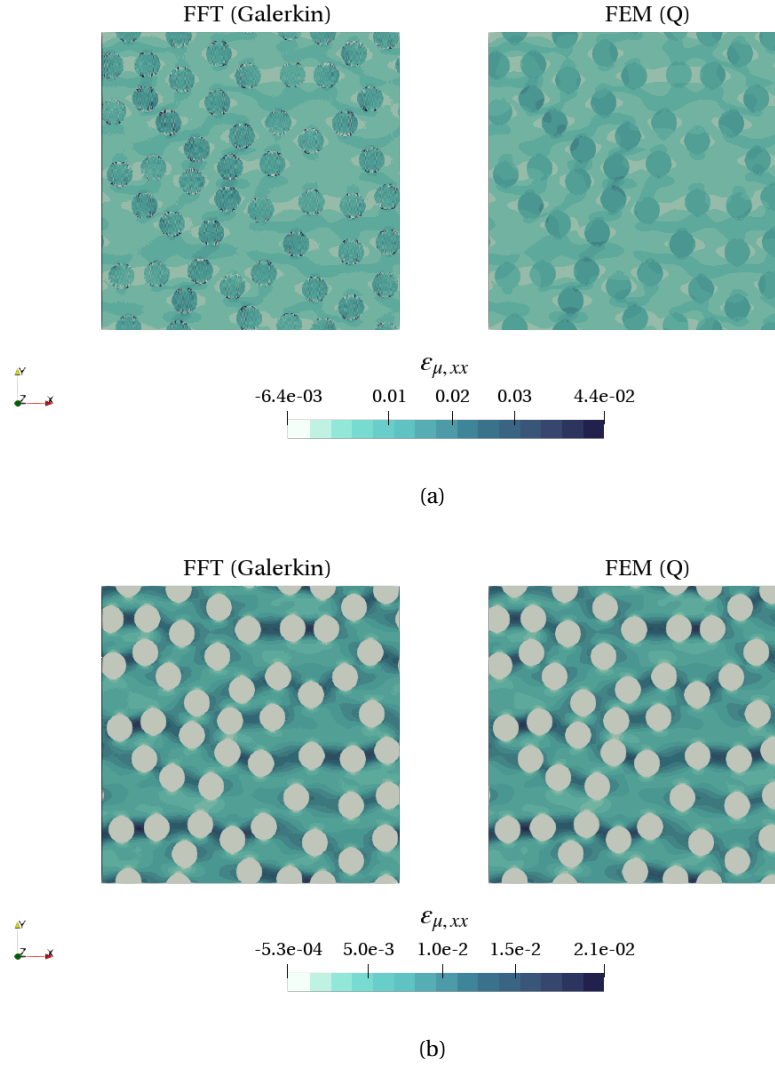


Figure 4.9: Comparison between the local strain field $\varepsilon_{\mu,xx}$ obtained using FFT and FEM-based homogenization approaches in the solution of the fiber-reinforced linear elastic composite equilibrium problem under normal strain loading conditions: (a) Stiffness ratio $K = E_1/E_2 = 10^{-4}$; (b) Stiffness ratio $K = E_1/E_2 = 10^{1.5}$; Notation: quadratic element (Q).

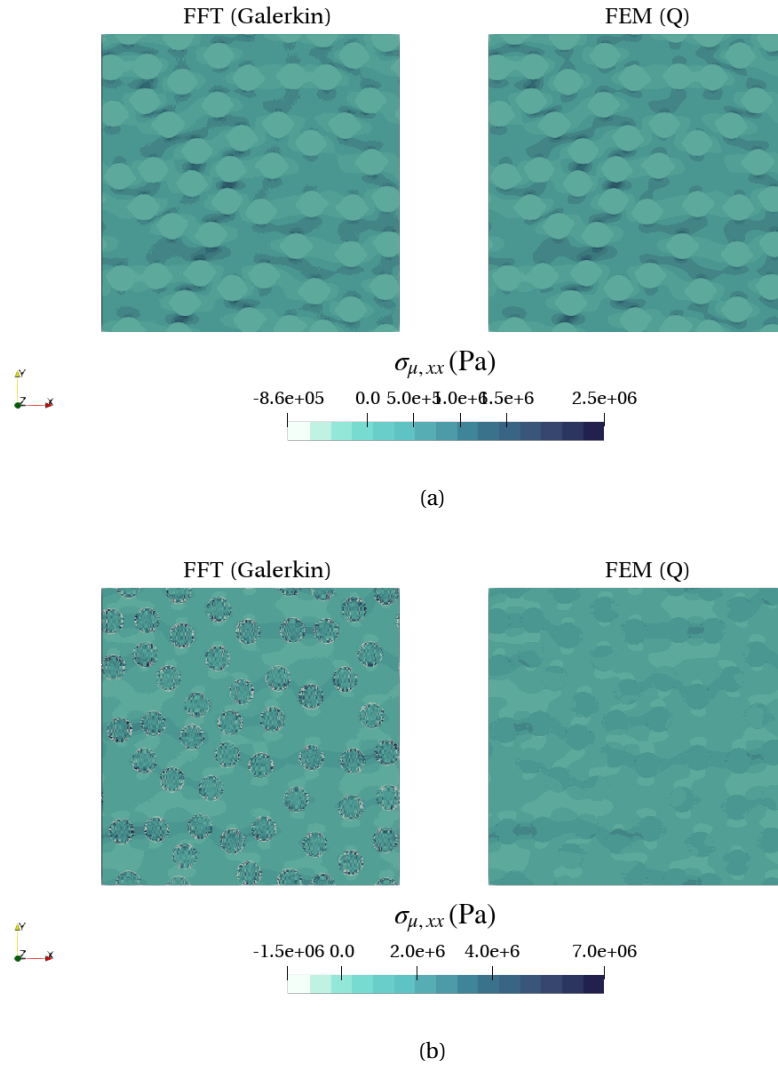


Figure 4.10: Comparison between the local stress field $\sigma_{\mu,xx}$ obtained using FFT and FEM-based homogenization approaches in the solution of the fiber-reinforced linear elastic composite equilibrium problem under normal strain loading conditions: (b) Stiffness ratio $K = E_1/E_2 = 10^{-4}$; (a) Stiffness ratio $K = E_1/E_2 = 10^{1.5}$; Notation: quadratic element (Q).

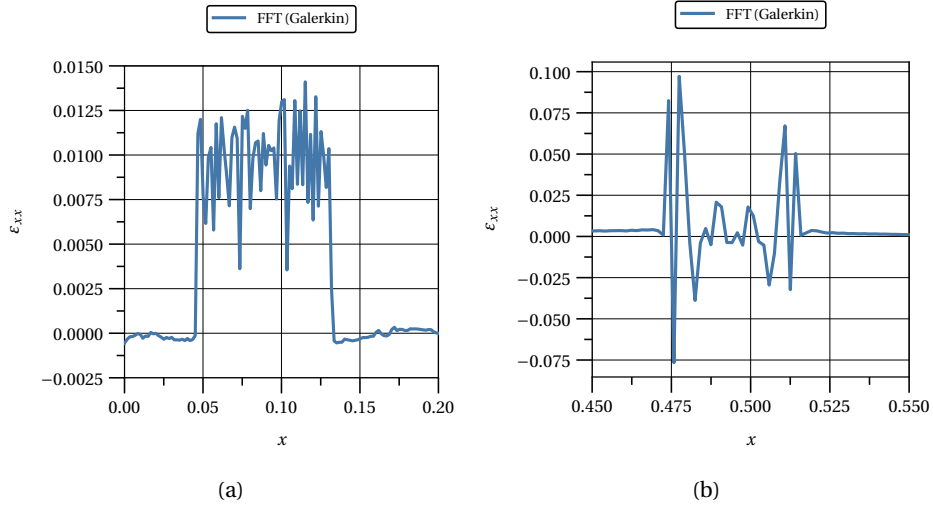


Figure 4.11: Normal microscopic strain, $\varepsilon_{\mu,xx}$, at $y = 0$ under a normal loading scheme as a function of the x coordinate for the fiber-reinforced linear elastic composite. The stiffness ratio between the matrix phase and the particle phase is $K = E_1 / E_2 = 10^{-4}$.

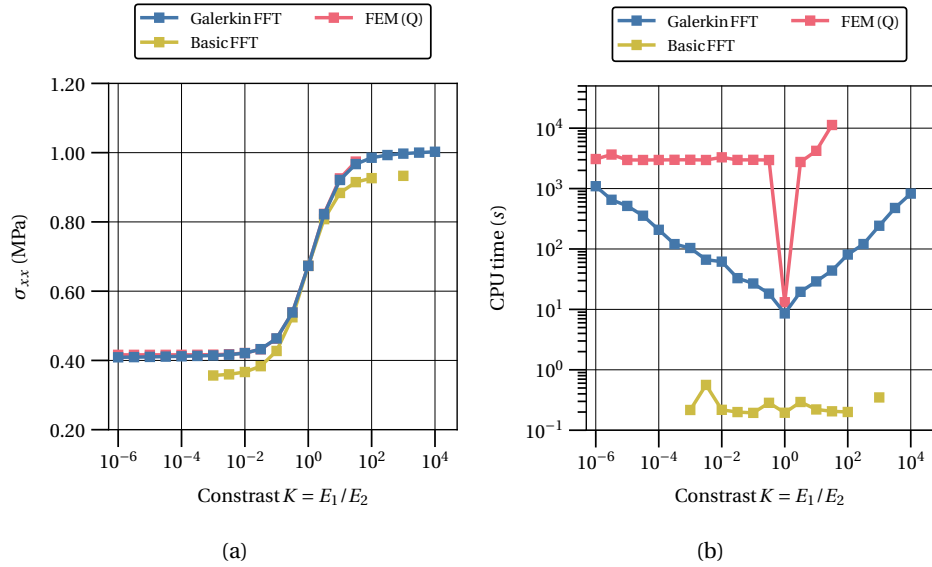


Figure 4.12: Comparison between the FFT and FEM-based homogenization approaches in the solution of the particle-reinforced linear elastic composite equilibrium problem under normal strain loading conditions: (a) Homogenized stress; (b) Computational time; Notation: linear element (L), quadratic element (Q).

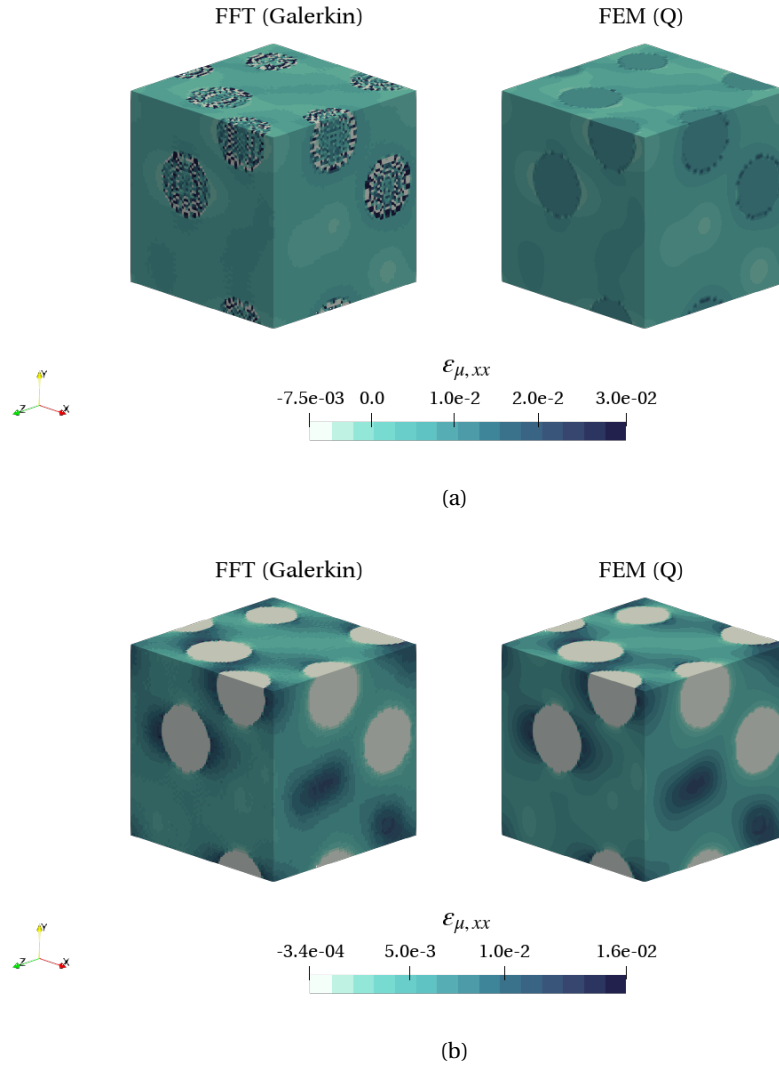


Figure 4.13: Comparison between the local strain field $\varepsilon_{\mu,xx}$ obtained using FFT and FEM-based homogenization approaches in the solution of the particle-reinforced linear elastic composite equilibrium problem under normal strain loading conditions: (a) Stiffness ratio $K = E_1/E_2 = 10^{-4}$; (b) Stiffness ratio $K = E_1/E_2 = 10^{1.5}$; Notation: quadratic element (Q).

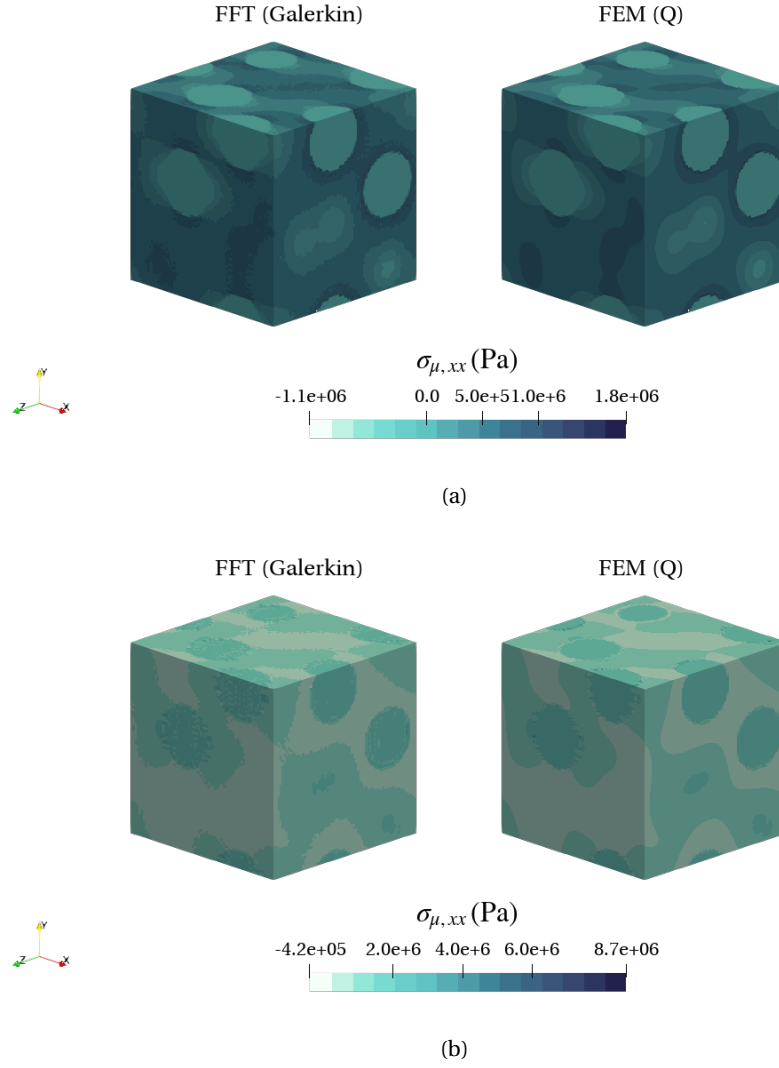


Figure 4.14: Comparison between the local stress field $\sigma_{\mu,xx}$ obtained using FFT and FEM-based homogenization approaches in the solution of the particle-reinforced linear elastic composite equilibrium problem under normal strain loading conditions: (b) Stiffness ratio $K = E_1/E_2 = 10^{-4}$; (a) Stiffness ratio $K = E_1/E_2 = 10^{1.5}$; Notation: quadratic element (Q).

4.2.2 Large strain

The following results concern large strains with materials being modeled either by the Hencky constitutive model or the Saint Venant-Kirchhoff constitutive model.

Mesh convergency studies A few mesh convergency studies are presented in what follows. Both phases are assumed to follow either the Hencky constitutive model or the Saint Venant-Kirchhoff model (see Table 4.2 for the properties), periodic boundary conditions are adopted and the following two macroscale strain loading cases are considered

$$\text{uniaxial: } \mathbf{F} = \begin{bmatrix} 1.1 & 0 \\ 0 & 1 \end{bmatrix}, \quad \text{pure shear: } \mathbf{F} = \begin{bmatrix} 1 & 0.3 \\ 0 & 1 \end{bmatrix}, \quad (4.23)$$

being enforced in a single load increment. Only the 2D microstructure is considered due to time and memory constraints.

Hencky The numerical results of the fiber-reinforced Hencky hyperelastic composite equilibrium problem are shown in Figures 4.15 and 4.16 for the uniaxial and pure shear loading cases, respectively. In both cases the finest mesh used fails to achieve convergence and there is still some disagreement between the FFT and FEM-based homogenization solutions regarding the homogenized response (see Figures 4.15(a) and 4.16(a)). In what concerns, the local strain fields (see Figures 4.18(c) and 4.19(c)), visually, there seems to be a good agreement between the two approaches. In terms of computational performance, Figures 4.15(b) and 4.16(b) show that the FFT-based homogenization Galerkin scheme outperforms the FEM-based homogenization with speedups of around 2 relative to the direct solver with linear quadratic elements. However, the caveat regarding parallelization still applies.

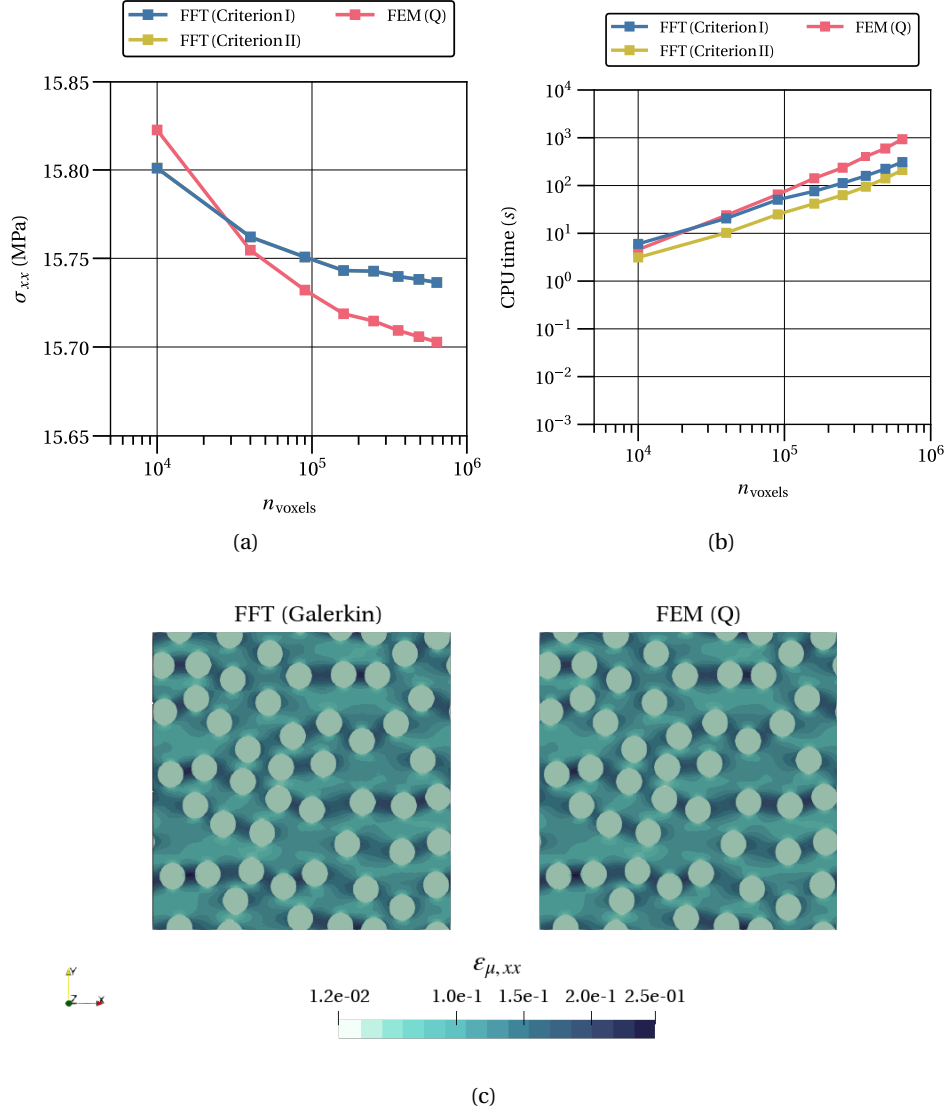


Figure 4.15: Comparison between the FFT (Criterion I and II) and FEM-based homogenization approaches in the solution of the fiber-reinforced hyperelastic (Hencky constitutive model) composite equilibrium problem under normal strain loading conditions: (a) Homogenized stress; (b) Computational time; (c) Local strain field ($n_v = 600 \times 600$ discretization). Notation: quadratic element (Q)

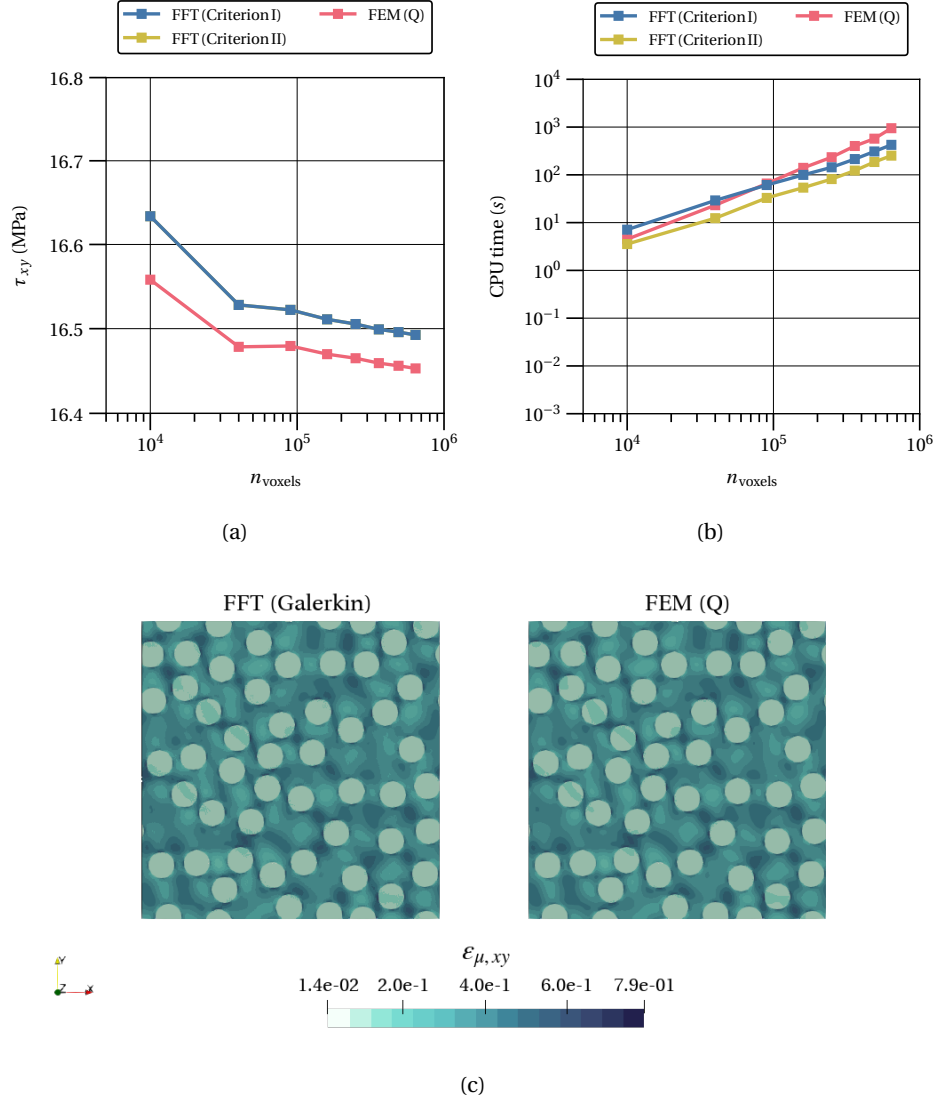


Figure 4.16: Comparison between the FFT (Criterion I and II) and FEM-based homogenization approaches in the solution of the fiber-reinforced hyperelastic (Hencky constitutive model) composite equilibrium problem under pure shear strain loading conditions: (a) Homogenized stress; (b) Computational time; (c) Local strain field ($n_v = 600 \times 600$ discretization). Notation: quadratic element (Q)

Saint Venant-Kirchhoff model The numerical results of the fiber-reinforced Saint Venant-Kirchhoff hyperelastic composite equilibrium problem are shown in Figure 4.17 for the uniaxial loading case. Neither the FFT-based nor the FEM-based homogenization procedures are able to solve the equilibrium problem for the pure shear loading cases when the load is enforced in a single increment, as such these results are not presented. There is an excellent agreement between the FFT and FEM-based homogenization solutions concerning both the homogenized response (see Figure 4.17(a)) and the local strain fields (see Figure 4.17(c)). In terms of computational performance, Figure 4.17(b) shows that the FFT-based homogenization Galerkin scheme outperforms the FEM-based homogenization with speedups of around 2 to 10 relative to the direct solver with quadratic finite elements as the number of voxels increases. The caveat previously mentioned regarding the parallelization of both schemes still applies. Comparing the convergence criteria for the FFT schemes, Criterion I remains the most efficient without compromising accuracy.

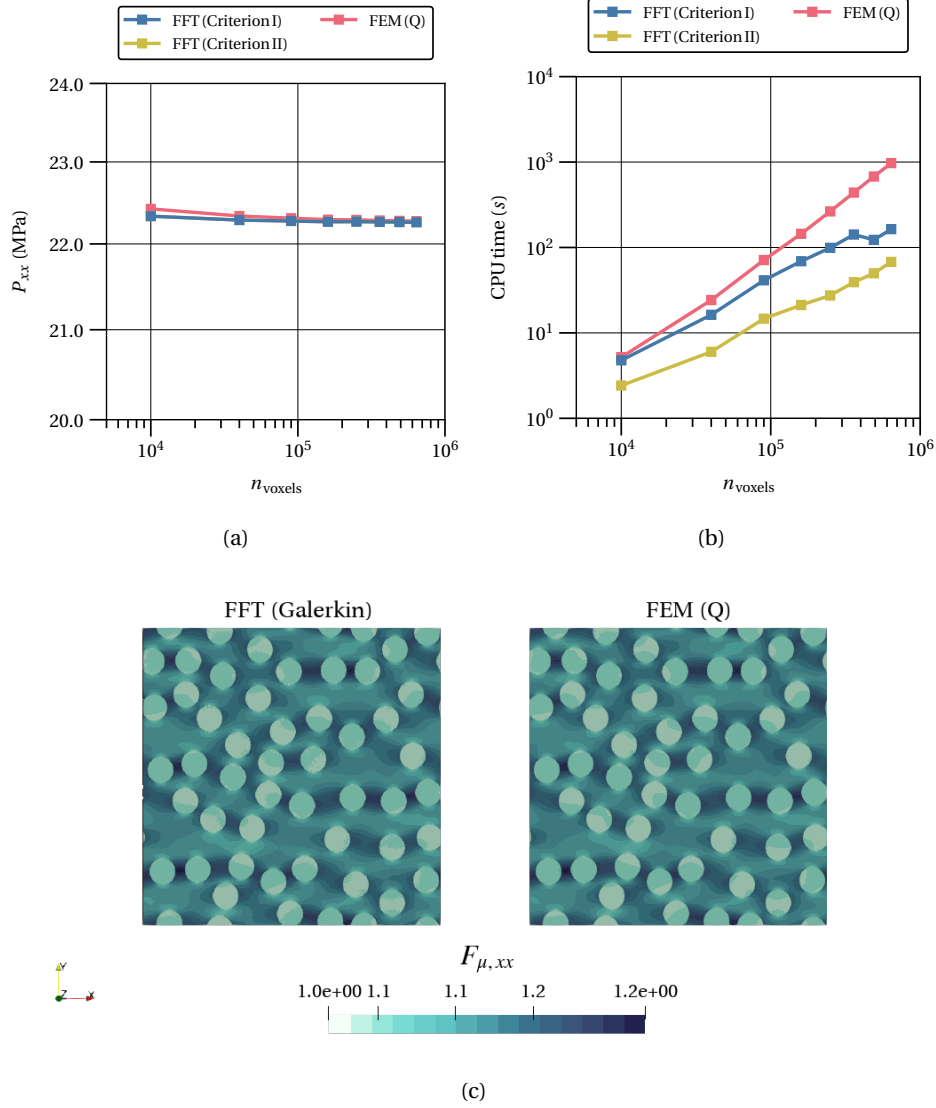


Figure 4.17: Comparison between the FFT (Criterion I and II) and FEM-based homogenization approaches in the solution of the fiber-reinforced hyperelastic (Saint Venant-Kirchhoff constitutive model) composite equilibrium problem under normal strain loading conditions: (a) Homogenized stress; (b) Computational time; (c) Local strain field ($n_v = 600 \times 600$ discretization). Notation: quadratic element (Q)

Accuracy validation Both phases are assumed to follow either the Hencky constitutive model or the Saint Venant-Kirchhoff model (see Table 4.2 for the properties), periodic boundary conditions are adopted and the following two macroscale strain loading cases are considered

$$\text{uniaxial: } \mathbf{F} = \begin{bmatrix} 1.3 & 0 & 0 \\ 0 & 1 & 0 \\ 0 & 0 & 1 \end{bmatrix}, \quad \text{pure shear: } \mathbf{F} = \begin{bmatrix} 1 & 0.3 & 0 \\ 0 & 1 & 0 \\ 0 & 0 & 1 \end{bmatrix}, \quad (4.24)$$

being enforced in 200 load increments. The convergence criterion used for the FFT Galerkin method scheme is Criterion II (see Section 3.8). Both schemes (FFT and FEM) use all the cores available in the machine. The mesh used is $n_e = 600 \times 600$ for both models, despite the fact that for the Hencky constitutive model convergence with the FEM solution is not achieved.

Hencky The numerical results of the fiber-reinforced linear elastic composite equilibrium problem are shown in Figures 4.18 and 4.19 for the uniaxial and pure shear loading cases, respectively.

In both cases there is an excellent agreement between the FFT and FEM-based homogenization solutions concerning both the homogenized response (see Figures 4.18(a), 4.18(b), 4.19(a) and 4.19(b) and the local strain fields (see Figures 4.18(c) and 4.19(c)). Moreover, the relative error of the FFT solution when compared for both loading schemes with the FEM solution is very low. Under 0.1% for the uniaxial load and under 0.015% for the pure shear load. However, it must be kept in mind that the enforced deformation is not very large as can be seen from the relatively small deviation of the material response from linear behavior. The deformation values are conservative for a hyperelastic material because the FEM solutions fail to converge for more demanding values with 200 load increments. The FFT-based Galerkin method homogenization scheme is able to obtain the correct solution for uniaxial strains F_{xx} as high as 1.5 in a single load increment. This is found from numerical experience using a coarser mesh and more than 200 increments.

In terms of computational performance, Table 4.3 shows that FFT and FEM approaches take about the same CPU time for both loading schemes, i.e, around three hours and twenty minutes. Table 4.4 shows the time profile for the FFT-based homogenization approach in the solution of the fiber-reinforced hyperelastic (Hencky constitutive model) composite equilibrium problem under uniaxial strain loading conditions ($n_v = 600 \times 600$). The phase of the solution procedure that takes the majority of the time is the state update ($\approx 92\%$). The application of the projection operator, repeated during the solution using the conjugate gradient method takes only $\approx 6\%$ of the time.

Table 4.3: Comparison between the CPU time required by the FFT-based and FEM-based homogenization approaches in the solution of the fiber-reinforced hyperelastic (Hencky constitutive model) composite equilibrium problem under uniaxial and pure strain loading conditions ($n_\nu = 600 \times 600$).

Loading scheme	CPU Time (s)	
	FFT	FEM
Uniaxial strain	1.16×10^4	1.20×10^4
Pure shear strain	1.14×10^4	1.20×10^4

Table 4.4: Time profile for the FFT-based homogenization approach in the solution of the fiber-reinforced hyperelastic (Hencky constitutive model) composite equilibrium problem under uniaxial strain loading conditions ($n_\nu = 600 \times 600$).

Phase	Duration (s)	Duration (%)
Assembling material constitutive functions	3.09	0.03
Setting up projection operator and the generator for the equilibrium operator	5.80×10^{-2}	0.00
State update	1.06×10^4	91.78
Applying projection operator	7.01×10^2	6.05
Other	2.64×10^2	2.27
Total time	1.16×10^4	

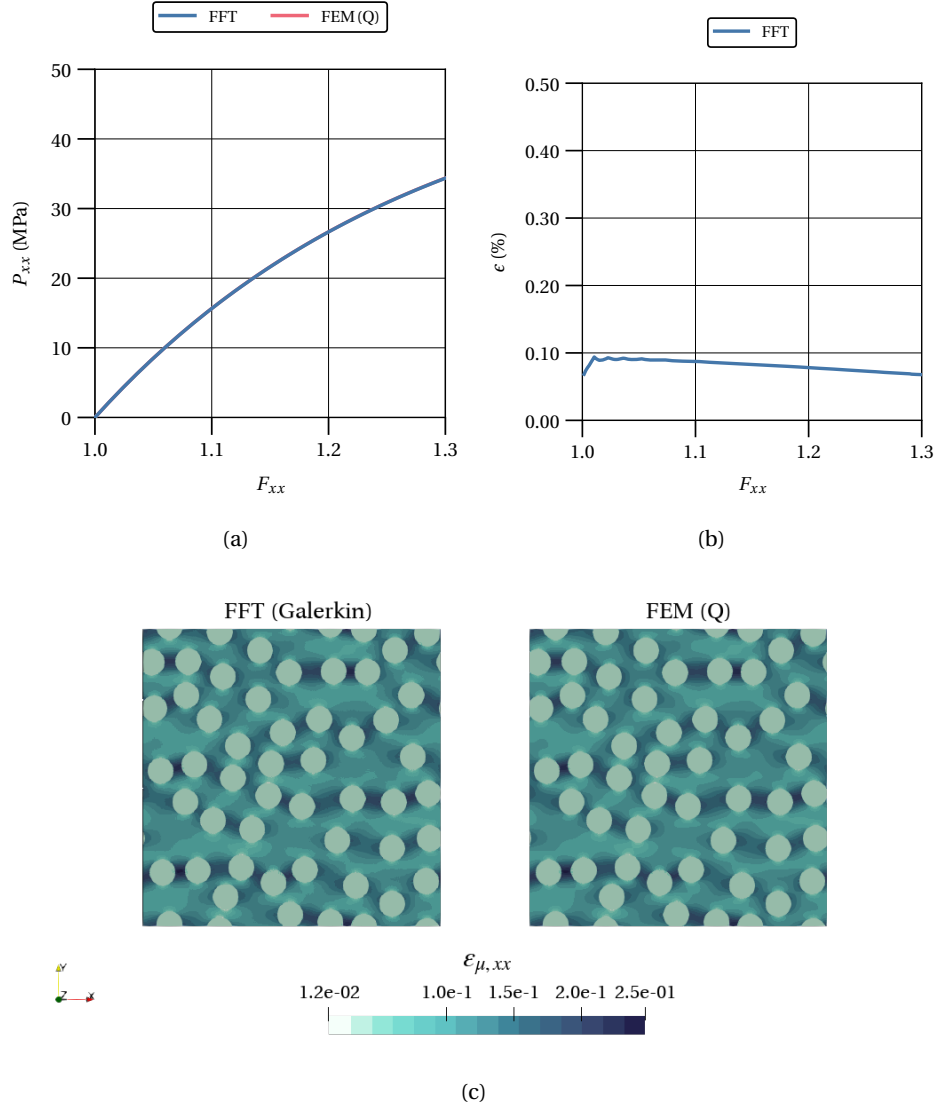


Figure 4.18: Comparison between the FFT-based and FEM-based homogenization approaches in the solution of the fiber-reinforced hyperelastic (Hencky constitutive model) composite equilibrium problem under uniaxial strain loading conditions: (a) Homogenized material response; (b) Relative error of the homogenized material response obtained with the FFT approach relative to the FEM approach; (c) Local strain field at full load ($n_v = 600 \times 600$ discretization). Notation: quadratic element (Q).

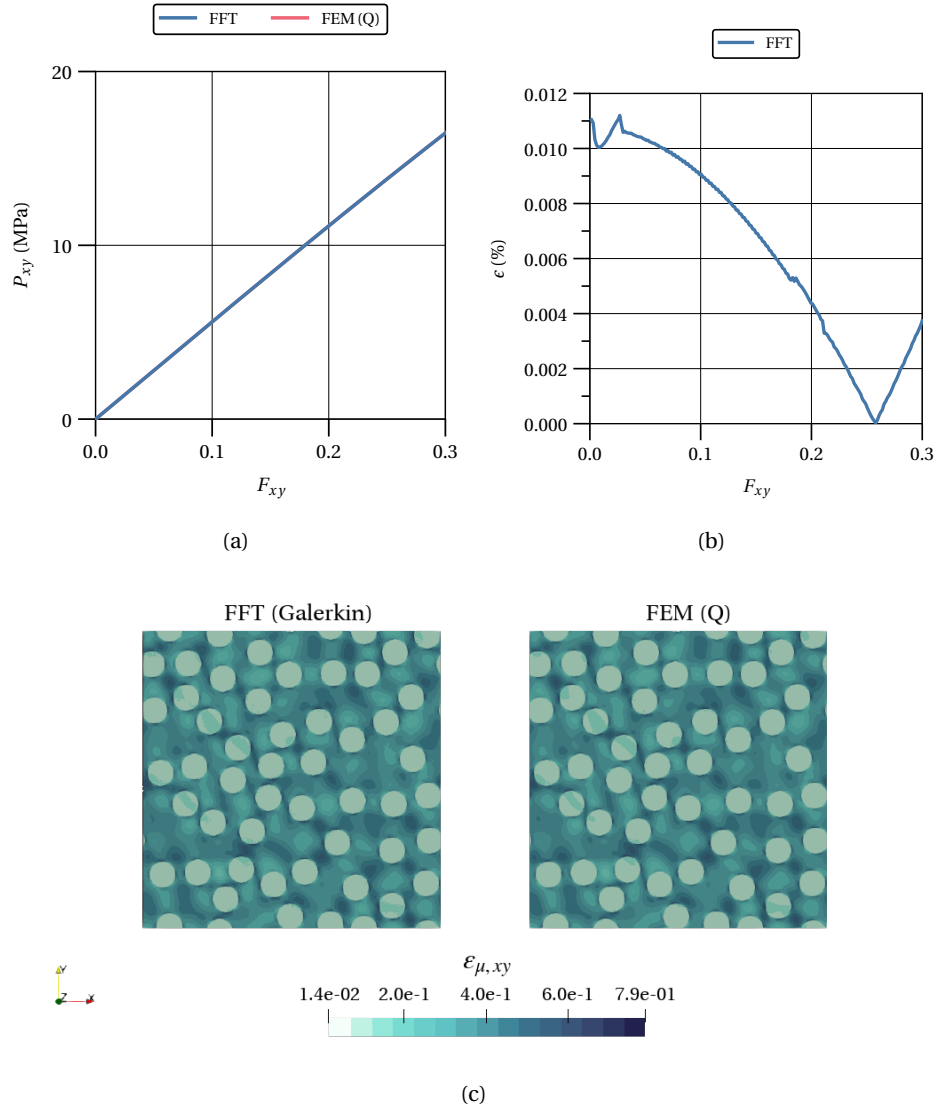


Figure 4.19: Comparison between the FFT-based and FEM-based homogenization approaches in the solution of the fiber-reinforced hyperelastic (Hencky constitutive model) composite equilibrium problem under shear strain loading conditions: (a) Homogenized material response; (b) Relative error of the homogenized material response obtained with the FFT approach relative to the FEM approach; (c) Local strain field at full load ($n_v = 600 \times 600$ discretization). Notation: quadratic element (Q).

Saint Venant-Kirchhoff model The numerical results of the fiber-reinforced hyperelastic (Saint Venant-Kirchhoff) composite equilibrium problem are shown in Figures 4.20 and 4.21 for the uniaxial and pure shear loading cases, respectively.

In both cases there is an excellent agreement between the FFT and FEM-based homogenization solutions concerning both the homogenized response (see Figures 4.20(a), 4.20(b), 4.21(a) and 4.21(b) and the local strain fields (see Figure 4.17(c)). Moreover, the relative error of the FFT solution when compared for both loading schemes with the FEM solution is very low. Under 0.1% for the uniaxial load and under 0.02% for the pure shear load. However, as before it must be kept in mind that the enforced deformation is not very large as can be seen from the relatively small deviation of the material response from linear behavior. The deformation values are conservative for a hyperelastic material because the FEM solutions fail to converge for more demanding values with 200 load increments. In Figure 4.21, it can be seen that the FEM procedure did not reach the full load for the pure shear loading scheme enforced in 200 increments.

In terms of computational performance, Table 4.5 shows that the FFT approach is three times faster than the FEM approach. Comparing with Table 4.5, one can also conclude that solving the fiber-reinforced hyperelastic composite equilibrium problem using FFT is also three times faster when modelling both phases using the Saint Venant-Kirchhoff constitutive model than the Hencky constitutive model. Looking at Table 4.6, where the time profile for the FFT-based homogenization approach under uniaxial loading conditions is shown it can be understood why. The difference can be found in the time taken by the state update procedure, as the application of the projection operator takes about the same time (7×10^2 s). This is due to the more convoluted pre- and post-processing needed to use the Hencky constitutive model. These procedures are also possibly present in the FEM implementation for both models explaining the time difference observed for to obtain the final solution.

Table 4.5: Comparison between the CPU time required by the FFT-based and FEM-based homogenization approaches in the solution of the fiber-reinforced hyperelastic (Saint Venant-Kirchhoff constitutive model) composite equilibrium problem under uniaxial and pure strain loading conditions ($n_v = 600 \times 600$).

Loading scheme	CPU Time (s)	
	FFT	FEM
Uniaxial strain	3.55×10^3	1.19×10^4
Pure shear strain	3.69×10^3	-

Table 4.6: Time profile for the FFT-based homogenization approach in the solution of the fiber-reinforced hyperelastic (Saint Venat-Kirchhoff constitutive model) composite equilibrium problem under uniaxial loading conditions ($n_\nu = 600 \times 600$).

Phase	Duration (s)	Duration (%)
Assembling material constitutive functions	2.24	0.06
Setting up projection operator and the generator for the equilibrium operator	5.30×10^{-2}	0.00
State update	2.64×10^3	74.53
Applying projection operator	6.90×10^2	19.47
Other	2.15×10^2	6.05
Total time	3.55×10^3	

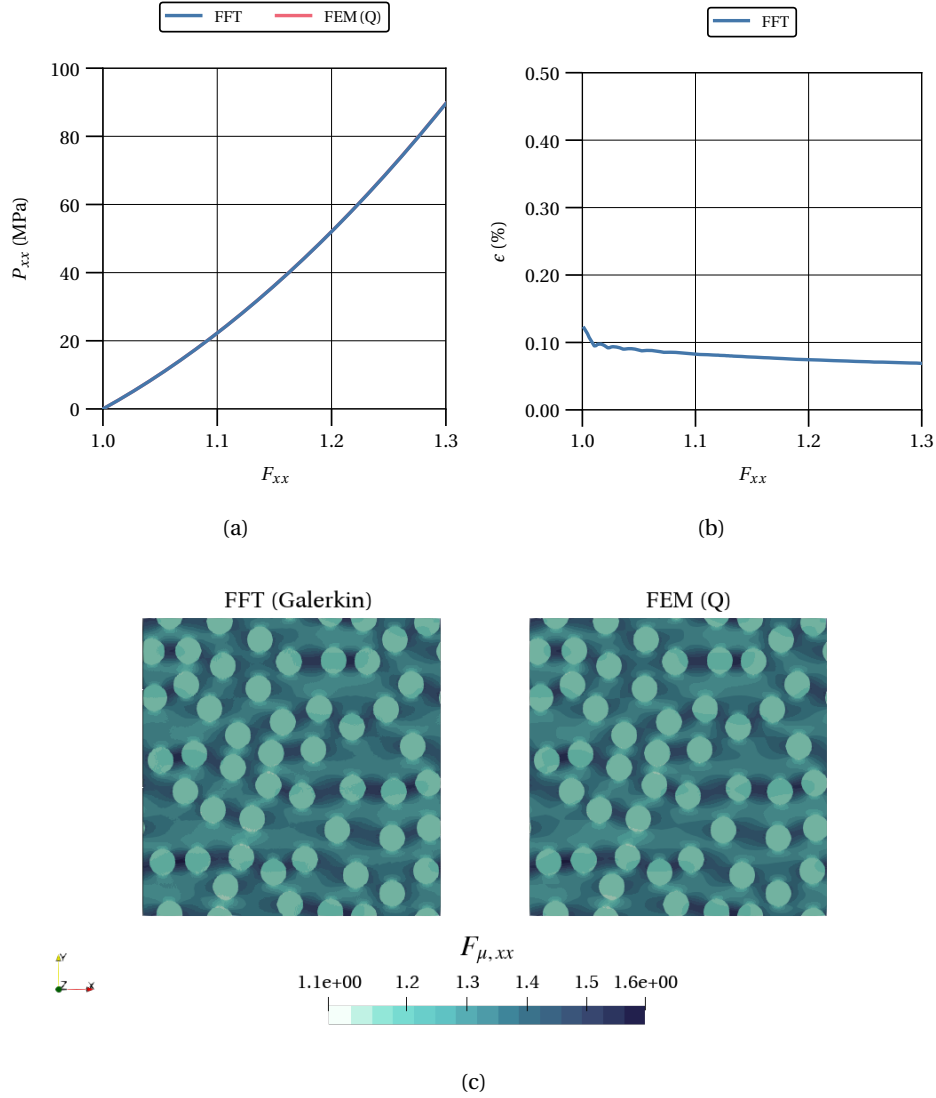


Figure 4.20: Comparison between the FFT-based and FEM-based homogenization approaches in the solution of the fiber-reinforced hyperelastic (Saint Venant-Kirchhoff constitutive model) composite equilibrium problem under uniaxial strain loading conditions: (a) Homogenized material response; (b) Relative error of the homogenized material response obtained with the FFT approach relative to the FEM approach; (c) Local strain field at full load ($n_v = 600 \times 600$ discretization). Notation: quadratic element (Q).

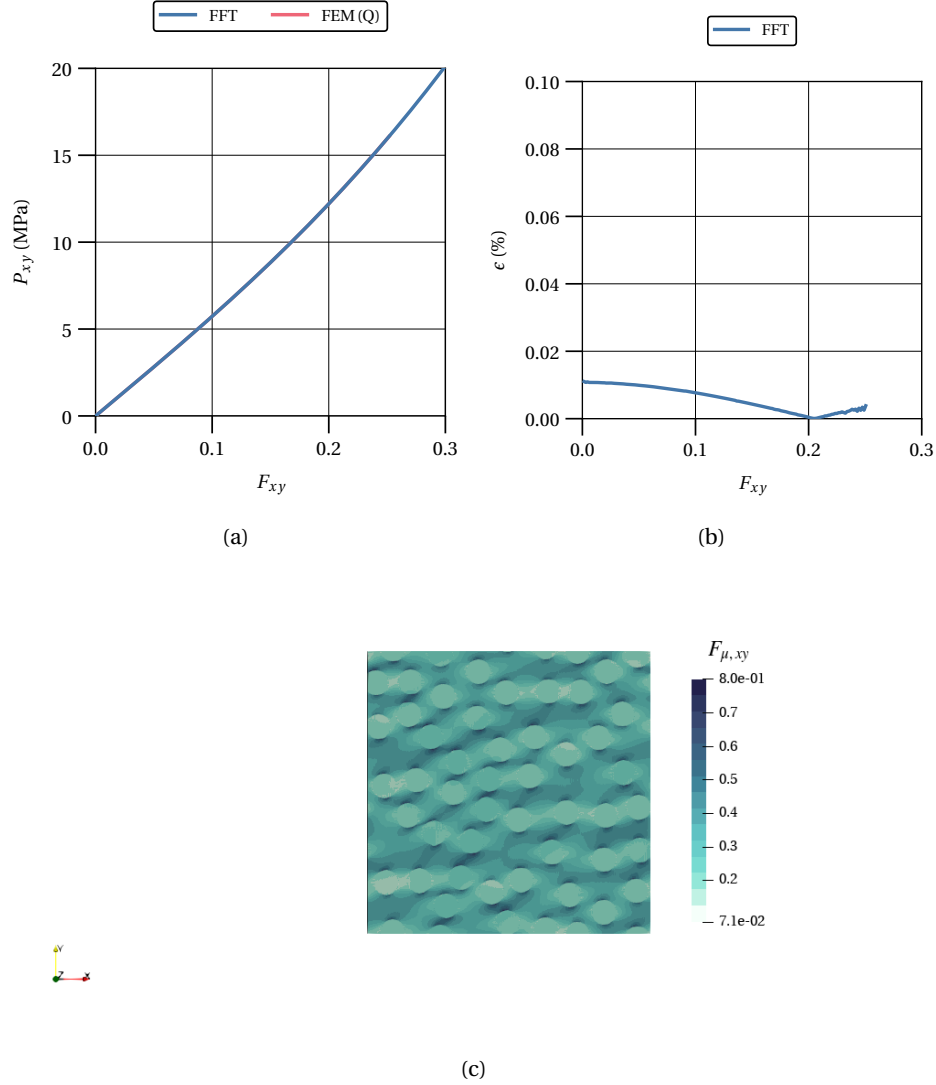


Figure 4.21: Comparison between the FFT-based and FEM-based homogenization approaches in the solution of the fiber-reinforced hyperelastic (Hencky constitutive model) composite equilibrium problem under shear strain loading conditions: (a) Homogenized material response; (b) Relative error of the homogenized material response obtained with the FFT approach relative to the FEM approach; (c) Local strain field at full load - Only FFT available since the FEM solution did not reach full load ($n_v = 600 \times 600$ discretization). Notation: quadratic element (Q).

Extreme stiffness ratios between phases The following set of results is presented to better comprehend the limitations of the FFT-based methods regarding the stiffness ratio between the phases. As previously, FEM solutions are used as a comparison standard.

Both phases are assumed to follow either the Hencky constitutive model or the Saint Venant-Kirchhoff model having the same Poisson's ratio, $\nu = 0.3$. The Young modulus of the matrix is fixed at $E_1 = 100$ MPa and the ratio between the stiffness of the particles and the matrix, $K = E_1/E_2$, is made to vary from 10^{-6} to 10^4 in increments of $\times\sqrt{10}$. Periodic boundary conditions are adopted and the following macroscale strain loading case is considered

$$\text{uniaxial: } \mathbf{F} = \begin{bmatrix} 1.1 & 0 \\ 0 & 1 \end{bmatrix}, \quad (4.25)$$

being enforced in a single load increment. Only the 2D microstructure is considered due to time and memory constraints.

Hencky The numerical results of the fiber-reinforced hyperelastic (Hencky constitutive model) composite equilibrium problem are shown in Figures 4.22 for the uniaxial loading case. The FFT approach is not able to converge for very soft particles, more precisely, for stiffness ratios below 10^{-2} using Criterion II. Criterion I exhibited an even poorer behavior, failing to converge for ratios below $10^{-0.5}$ and above $10^{2.5}$. For the stiffness ratios where convergence is achieved, there is an excellent agreement between the FFT and FEM-based homogenization solutions concerning the homogenized response as attested by Figure 4.22(a). In terms of computational performance, Figure 4.22(b) shows that the FFT-based homogenization Galerkin scheme outperforms the FEM-based homogenization with speedups from around 5 at low stiffness contrast to around 2 at the strongest stiffness contrasts, both high and low, relative to the direct solver with quadratic finite elements. As before, the caveat regarding the parallelization of the Python libraries still applies.

Concerning the local field, an excellent agreement can be observed at both high ($K = E_1/E_2 = 10^4$) and low ($K = E_1/E_2 = 10^{-2}$) stiffness ratios in the matrix phase, as can be seen in Figures 4.24 and ???. There is also good agreement regarding the local field in the particle phase for the strain field at the low stiffness ratio and the stress field at the high stiffness ratio. On the other hand, the strain field at the low stiffness ratio and the stress field at the high stiffness ratio exhibit strong oscillations in the particle phase. In closing, it bears mentioning that this does not affect the accuracy of the homogenized response.

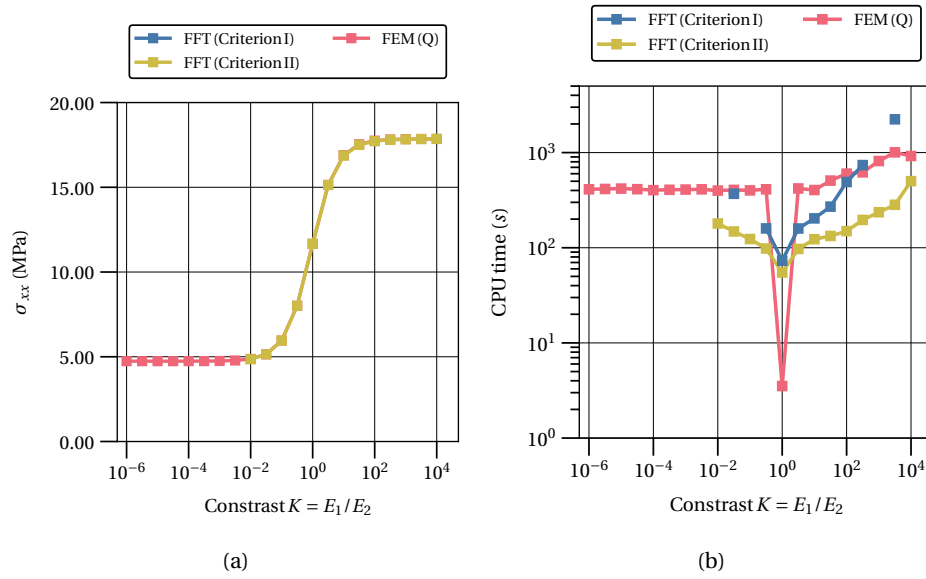


Figure 4.22: Comparison between the FFT and FEM-based homogenization approaches in the solution of the particle-reinforced hyperelastic (Hencky constitutive model) composite equilibrium problem under normal strain loading conditions: (a) Homogenized stress; (b) Computational time; Notation: quadratic element (Q).

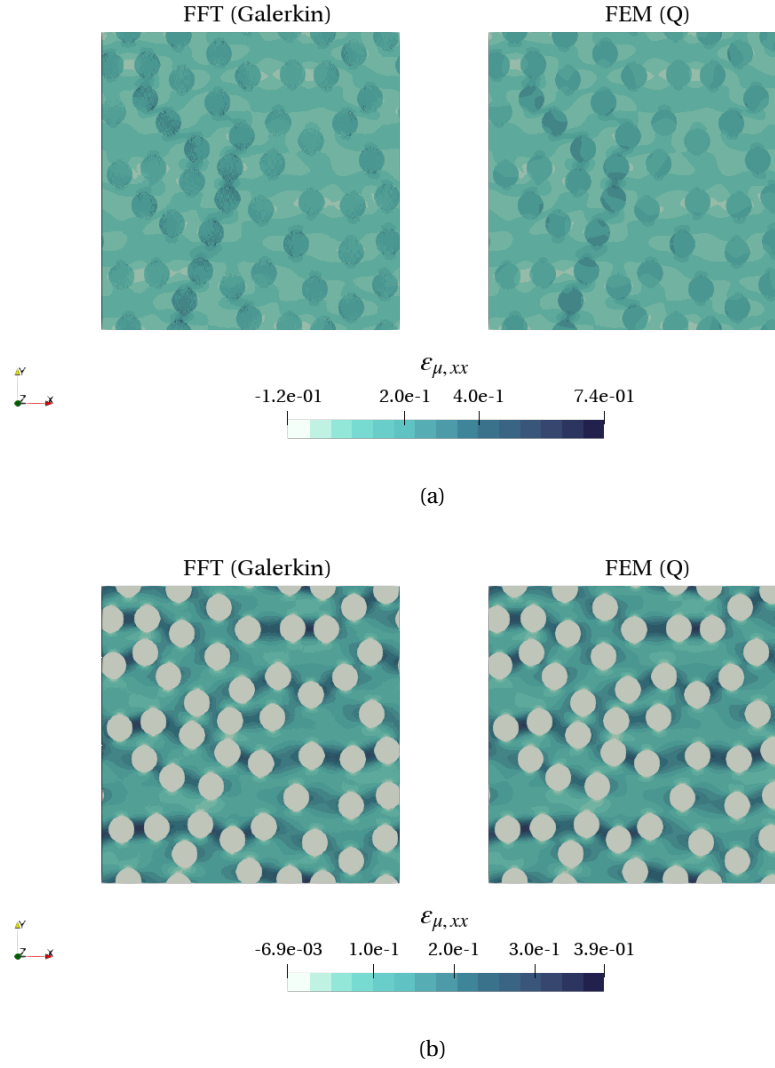


Figure 4.23: Comparison between the local logarithmic strain field $\varepsilon_{\mu,xx}$ obtained using FFT and FEM-based homogenization approaches in the solution of the fiber-reinforced hyperelastic (Hencky constitutive model) composite equilibrium problem under normal strain loading conditions: (a) Stiffness ratio $K = E_1/E_2 = 10^{-2}$; (b) Stiffness ratio $K = E_1/E_2 = 10^4$; Notation: quadratic element (Q).

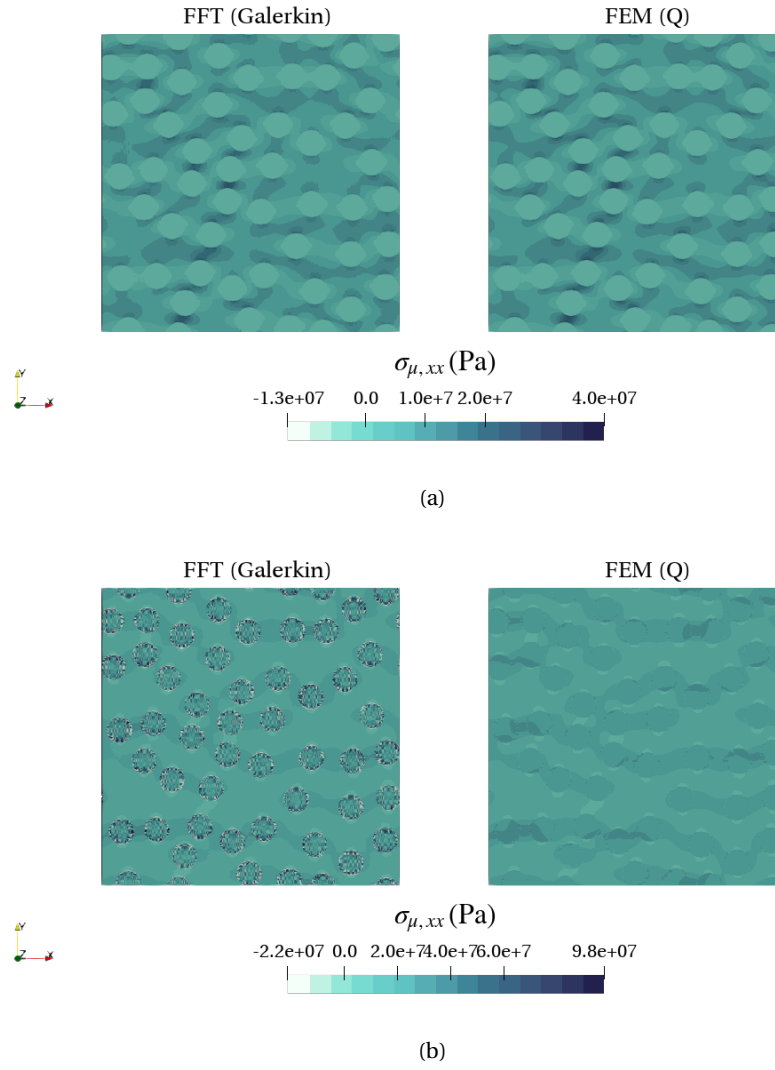


Figure 4.24: Comparison between the local stress field $\sigma_{\mu,xx}$ obtained using FFT and FEM-based homogenization approaches in the solution of the fiber-reinforced hyperelastic (Hencky constitutive model) composite equilibrium problem under normal stress loading conditions: (b) Stiffness ratio $K = E_1/E_2 = 10^{-2}$; (a) Stiffness ratio $K = E_1/E_2 = 10^4$; Notation: quadratic element (Q).

Saint Venant-Kirchhoff model The numerical results of the fiber-reinforced hyperelastic (Saint Venant-Kirchhoff constitutive model) composite equilibrium problem are shown in Figures 4.25 for the uniaxial loading case. The FFT approach when using Criterion I is not able to converge for stiffness ratios below 10^{-2} and above 10^2 . On the other hand, using Criterion II, convergence is achieved for all stiffness ratios. Moreover, there is an excellent agreement between the FFT and FEM-based homogenization solutions concerning the homogenized response as attested by Figure 4.25(a). In terms of computational performance, Figure 4.25(b) shows that the FFT-based homogenization Galerkin scheme outperforms the FEM-based homogenization with speedups from around 25 at low stiffness contrast to around 2 at the strongest stiffness contrasts, both high and low, relative to the direct solver with quadratic finite elements. As before, the caveat regarding the parallelization of the Python libraries still applies.

Concerning the local field, an excellent agreement can be observed at both high ($K = E_1/E_2 = 10^4$) and low ($K = E_1/E_2 = 10^{-4}$) stiffness ratios in the matrix phase, as can be seen in Figure 4.26. There is also good agreement regarding the local field in the particle phase for the strain field at the low stiffness ratio. On the other hand, the strain field at the low stiffness ratio exhibits strong oscillations in the particle phase. Results for the stress fields are not presented as the same stress measure was not available for both homogenization schemes using the Saint Venant-Kirchhoff constitutive model. In closing, it bears mentioning that this does not affect the accuracy of the homogenized response.

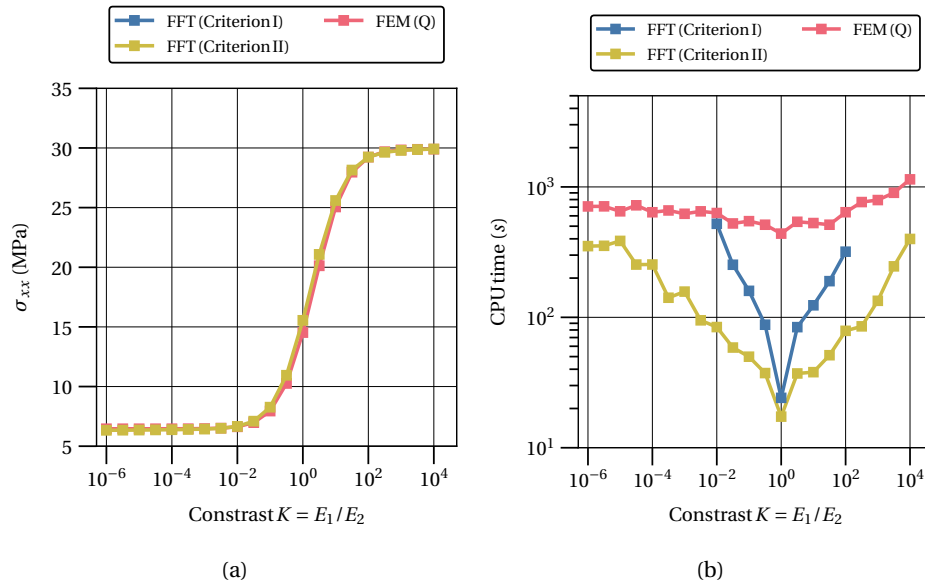


Figure 4.25: Comparison between the FFT and FEM-based homogenization approaches in the solution of the particle-reinforced hyperelastic (Saint Venant-Kirchhoff constitutive model) composite equilibrium problem under normal strain loading conditions: (a) Homogenized stress; (b) Computational time; Notation: quadratic element (Q).

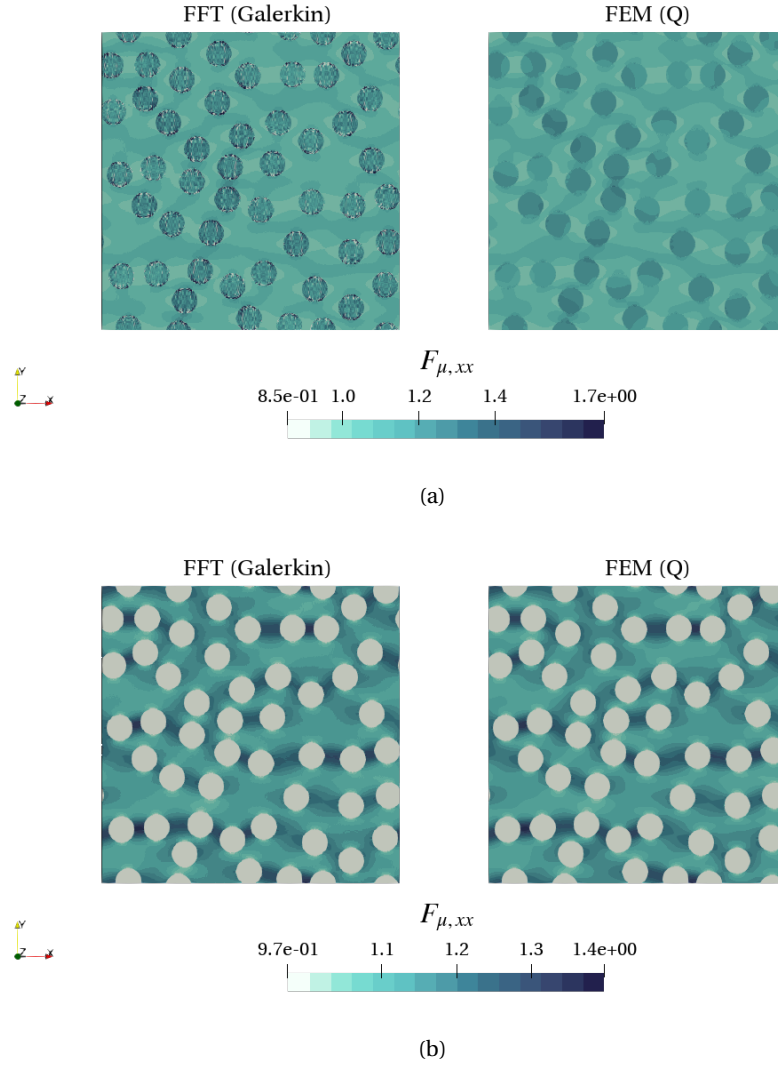


Figure 4.26: Comparison between the local strain field $F_{\mu,xx}$ obtained using FFT and FEM-based homogenization approaches in the solution of the fiber-reinforced hyperelastic (Hencky constitutive model) composite equilibrium problem under normal strain loading conditions: (a) Stiffness ratio $K = E_1/E_2 = 10^{-4}$; (b) Stiffness ratio $K = E_1/E_2 = 10^4$; Notation: quadratic element (Q).

Chapter 5

Numerical Results - Elastoplasticity

In the following chapter, results pertaining to elastoelasticity are presented. The validation of the FFT-based Galerkin formulation is performed on elastoplastic materials at small strains and large strains. The constitutive model considered is von Mises material model.

As in the previous chapter, all the numerical results shown in this chapter are obtained in the same machine with the specifications provided in Table 5.1. Contrary to the previous chapter, all the available cores in the machine are used in each simulation.

Table 5.1: Specifications of the numerical testing machine.

CPU	Model	2× Intel Xeon E5-2650 v4
	Microarchitecture	Broadwell
	Base/Max Frequency	2.20/2.90GHz
	Num. of cores/threads	24/48(2 × 12/24)
	L1 Cache	718KiB(2 × 384KiB)
	L2 Cache	6MiB(2 × 3MiB)
	L3 Cache	60MiB(2 × 30MiB)
	Numerical features	SSE3 SSSE3 AVX2
Memory	Capacity	128 GB(8 × 16 GB)
	Specification	DDR4 @ 2400MHz

5.1 Material characterization

The microstructures and linear elastic properties considered in the following can be found in Section 4.1. The isotropic piecewise linear strain hardening law is presented

in Figure 5.1. The yield stress, σ_y , is given as a function of the accumulated plastic strain, $\bar{\epsilon}_p$ by

$$\sigma_y = \begin{cases} 0.5 + 5\bar{\epsilon}_p, & 0 \leq \bar{\epsilon}_p \leq 0.04 \\ 0.7 + 2(\bar{\epsilon}_p - 0.04), & \bar{\epsilon}_p \geq 0.04 \end{cases}, \quad \text{MPa.} \quad (5.1)$$

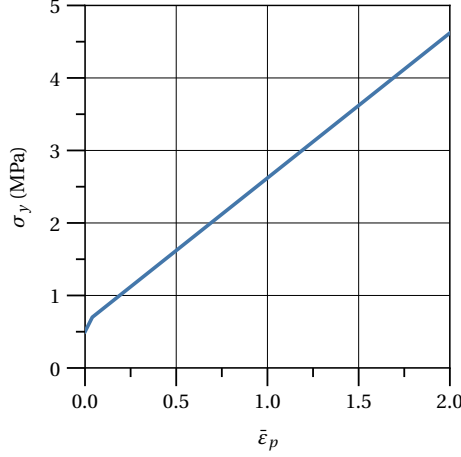


Figure 5.1: Von Mises elastoplastic matrix isotropic piecewise linear strain hardening law.

5.1.1 von Mises - small strains

Constitutive model The model considered here for the elastoplastic behavior of the material is the von Mises model with associative potential and isotropic hardening, also known as standard J_2 -plasticity. In this model the total strain, $\boldsymbol{\epsilon}$, is additively split into an elastic part, $\boldsymbol{\epsilon}^e$, and a plastic part, $\boldsymbol{\epsilon}^p$, i.e.

$$\boldsymbol{\epsilon} = \boldsymbol{\epsilon}^e + \boldsymbol{\epsilon}^p, \quad (5.2)$$

The stress, $\boldsymbol{\sigma}$, depends on the elastic strain, $\boldsymbol{\epsilon}^e$, through the standard linear relation

$$\boldsymbol{\sigma} = \mathbf{D}^e : (\boldsymbol{\epsilon} - \boldsymbol{\epsilon}^p), \quad \text{with} \quad \mathbf{D}^e = K\mathbf{I} \otimes \mathbf{I} + 2G\mathbf{I}_d \quad (5.3)$$

wherein K is the bulk modulus, G is the shear modulus and \mathbf{I}_d is (?)¹. The elastic domain is bounded by the plastic admissibility condition

$$\Phi(\boldsymbol{\sigma}, \bar{\epsilon}^p) = \sigma_{\text{eq}} - \sigma_y(\bar{\epsilon}^p) \leq 0, \quad (5.4)$$

where σ_y is the hardening curve. The deformation history enters this expression via the accumulated plastic strain, $\bar{\epsilon}^p$, which equals zero in the initial stress-free state.

Finally, the von Mises equivalent stress, σ_{eq} , is defined as

$$\sigma_{\text{eq}} = \sqrt{\frac{3}{2} \mathbf{s} : \mathbf{s}} \quad (5.5)$$

¹The (?) is defined as $(\mathbf{I}_d)_{ijkl} = (?)$.

with \mathbf{s} the stress deviator. The plastic strain rate follows from the associative potential or normality as

$$\dot{\boldsymbol{\varepsilon}}^p = \dot{\gamma} \mathbf{N} = \dot{\gamma} \frac{\partial \Phi}{\partial \boldsymbol{\sigma}} = \dot{\gamma} \sqrt{\frac{3}{2}} \frac{\mathbf{s}}{\|\mathbf{s}\|}. \quad (5.6)$$

The accumulated plastic strain is determined from

$$\bar{\boldsymbol{\varepsilon}}^p = \int_0^t \dot{\boldsymbol{\varepsilon}}^p dt, \quad \text{with} \quad \dot{\boldsymbol{\varepsilon}}^p = \sqrt{\frac{2}{3}} \dot{\boldsymbol{\varepsilon}}^p : \dot{\boldsymbol{\varepsilon}}^p = \dot{\gamma} \quad (5.7)$$

The model is discretized in time using the, unconditionally stable, backward Euler scheme. The stress update is implemented using an elastic-predictor plastic-corrector scheme, whereby the amount of plastic flow is determined in two steps. First, a trial state is calculated by assuming the increment in strain to be fully elastic, the elastic predictor. Second, if necessary, a return-map is used that quantifies the plastic strain increment, the plastic corrector.

Given an increment in total strain

$$\Delta \boldsymbol{\varepsilon} = \boldsymbol{\varepsilon}_{n+1} - \boldsymbol{\varepsilon}_n, \quad (5.8)$$

corresponding to a typical pseudo-time increment $[t_n, t_{n+1}]$, the trial state, or elastic predictor, denoted by $(\bullet)^{\text{trial}}$, is computed by assuming that $\Delta \boldsymbol{\varepsilon}$ gives rise to a purely elastic strain increment, i.e.,

$$\boldsymbol{\varepsilon}_{n+1}^{\text{trial}} = \boldsymbol{\varepsilon}_n^e + \Delta \boldsymbol{\varepsilon}, \quad (5.9)$$

$$\bar{\boldsymbol{\varepsilon}}_{n+1}^p = \bar{\boldsymbol{\varepsilon}}_n^p. \quad (5.10)$$

The corresponding trial stress is computed as

$$\boldsymbol{\sigma}_{n+1}^{\text{trial}} = \mathbf{D}^e : \boldsymbol{\varepsilon}_{n+1}^{\text{trial}}. \quad (5.11)$$

The trial yield stress is simply

$$\sigma_{y n+1}^{\text{trial}} = \sigma_y \left(\bar{\boldsymbol{\varepsilon}}_n^p \right) = \sigma_{y n}, \quad (5.12)$$

Having computed the elastic trial state, the next step in the algorithm is to check whether $\boldsymbol{\sigma}_{n+1}^{\text{trial}}$ lies inside or outside of the trial yield surface. If $\boldsymbol{\sigma}_{n+1}^{\text{trial}}$ lies inside of the trial yield surface, i.e. if

$$\Phi \left(\boldsymbol{\sigma}_{n+1}^{\text{trial}}, \bar{\boldsymbol{\varepsilon}}_{n+1}^p \right) \leq 0, \quad (5.13)$$

then the process within the interval $[t_n, t_{n+1}]$ is purely elastic and the elastic trial state itself is the solution to the integration problem. In this case,

$$\boldsymbol{\varepsilon}_{n+1}^e = \boldsymbol{\varepsilon}_{n+1}^{\text{trial}} \quad (5.14)$$

$$\boldsymbol{\sigma}_{n+1} = \boldsymbol{\sigma}_{n+1}^{\text{trial}} \quad (5.15)$$

$$\bar{\boldsymbol{\varepsilon}}_{n+1}^p = \bar{\boldsymbol{\varepsilon}}_{n+1}^{\text{trial}} = \bar{\boldsymbol{\varepsilon}}_n^p \quad (5.16)$$

$$\sigma_{y n+1} = \sigma_{y n+1}^{\text{trial}} = \sigma_{y n} \quad (5.17)$$

is updated.

Otherwise, the process is elastoplastic within the interval $[t_n, t_{n+1}]$ and the return mapping procedure has to be applied to return the trial state to an admissible state.

For this state, the equality needs to hold in the yield function, given the actual stress that in turn depends on the plastic flow. Due to the assumed associative potential or normality, this non-linear system of equations can be rewritten as a single scalar equation

$$\bar{\Phi}(\Delta\gamma) = \sigma_{eqn}^{\text{trial}} - 3G\Delta\gamma - \sigma_y(\bar{\epsilon}_n^p + \Delta\gamma) = 0, \quad (5.18)$$

which has to be solved for $\Delta\gamma$.

The resulting state can is then determined as

$$\boldsymbol{\epsilon}_{n+1}^p = \boldsymbol{\epsilon}_n^p + \Delta\gamma \mathbf{N}^{\text{trial}}, \quad (5.19)$$

$$\bar{\epsilon}_{n+1}^p = \bar{\epsilon}_n^p + \Delta\gamma, \quad (5.20)$$

$$\boldsymbol{\sigma}_{n+1} = \mathbf{D}^e : (\boldsymbol{\epsilon}_{n+1} - \boldsymbol{\epsilon}_{n+1}^p). \quad (5.21)$$

Consistent constitutive tangent The tangent is derived by linearizing the stress update procedure. If the trial state is elastic, i.e. when $\Phi^{\text{trial}} \leq 0$, the result is trivially $\mathbf{D} = \mathbf{D}^e$. Otherwise, the stress update needs to be linearized, giving

$$\begin{aligned} \mathbf{D}^{\text{ep}} &= \frac{\partial \boldsymbol{\sigma}_{n+1}}{\partial \boldsymbol{\epsilon}_{n+1}} \\ &= \mathbf{D}^e - \frac{6G^2 \Delta\gamma}{\sigma_{eqn}^{\text{trial}}} \mathbf{I}_d + 4G^2 \left(\frac{\Delta\gamma}{\sigma_{eqn}^{\text{trial}}} - \frac{1}{3G + \frac{\partial \sigma_y}{\partial \bar{\epsilon}^p}(\bar{\epsilon}_p + \Delta\gamma)} \right) \mathbf{N}^{\text{trial}} \otimes \mathbf{N}^{\text{trial}}. \end{aligned} \quad (5.22)$$

5.1.2 von Mises - large strains

The extension of the von Mises constitutive model from the context of small strains to large strains rest solely on a pre- and post-processing step. The remaining procedure regarding the state update and the consistent constitutive tangent is the same.

Pre-processing To enforce a multiplicative split of the elastic and plastic parts of the deformation gradient, the strain measure used instead of the small strain tensor is the Eulerian logarithmic strain tensor

$$\boldsymbol{\epsilon} \equiv \ln \mathbf{V} = \frac{1}{2} \ln \mathbf{B}, \quad (5.23)$$

where $\mathbf{B} = \mathbf{F}\mathbf{F}^T$ is left Cauchy-Green strain tensor, and \mathbf{F} the deformation gradient.

Post-processing The post-processing concerns the state update and the consistent tangent. For the state update, the first Piola-Kirchhoff stress tensor can be obtained as

$$\mathbf{P} = \boldsymbol{\tau} \mathbf{F}^{-T}, \quad (5.24)$$

keeping in mind that the stress measure outputed having used the pre-processing is the Kirchhof stress tensor $\boldsymbol{\tau}$.

Regarding the spatial consistent tangent, it is obtained using the expression in Equation (??), with the only difference being that instead of the elasticity tensor \mathbf{D}^e the elastoplastic tensor \mathbf{D}^{ep} is used.

5.2 Comparison between FFT and FEM-based homogenization

Small strain Only the two-dimensional microstructure described in Section 4.1 is again considered together with the elastic properties described in Table 4.2. The matrix is now assumed elastoplastic with a von Mises associative flow rule and the isotropic piecewise linear strain hardening law illustrated in Figure 5.1. Only small strains are considered. Periodic boundary conditions are adopted and the following two macroscale strain loading cases are considered

$$\text{uniaxial: } \boldsymbol{\varepsilon} = \begin{bmatrix} 5 & 0 \\ 0 & 0 \end{bmatrix} \times 10^{-2}, \quad \text{pure shear: } \boldsymbol{\varepsilon} = \begin{bmatrix} 0 & 2.5 \\ 2.5 & 0 \end{bmatrix} \times 10^{-2}, \quad (5.25)$$

being enforced in a total of 200 increments. Note that in the 2D plane strain case, only the in-plane O_{xy} macroscale strain components are enforced. In terms of spatial discretization, a grid $n_\nu = 600 \times 600$ is considered. The convergence criterion used is Criterion II, as described in Section 3.8.

The homogenized response of the fiber-reinforced composite under uniaxial and pure shear strain loading conditions is presented in Figures 5.2 and 5.4. The relative error with respect to the FEM reference solution is also shown. An excellent agreement between the two solutions is found. Moreover, the error is below 0.15% for the whole deformation history. The local strain fields can be found in Figure 5.3 and 5.5. Again, visually there is no detectable difference between the local field computed using the two different approaches.

In terms of computational performance, Table 5.2 shows that the FFT approach is around 20 times faster than the FEM approach. It is difficult to tell if this time difference is due to a greater efficiency of the FFT approach or a larger amount of pre- and post-processing steps used in the FEM implementation used. See Section 4.2.2 for an example of the impact of pre- and post-processing operation during state update in the execution time of the FFT approach.

Table 5.2: Comparison between the CPU time required by the FFT-based and FEM-based homogenization approaches in the solution of the fiber-reinforced (fibers: linear elastic; matrix: elastoplastic with a von Mises associative flow rule and the isotropic piecewise linear strain hardening law) composite equilibrium problem under uniaxial and pure strain loading conditions ($n_\nu = 600 \times 600$).

Loading scheme	CPU Time (s)	
	FFT	FEM
Uniaxial strain	1.24×10^3	2.00×10^4
Pure shear strain	2.87×10^3	3.64×10^4

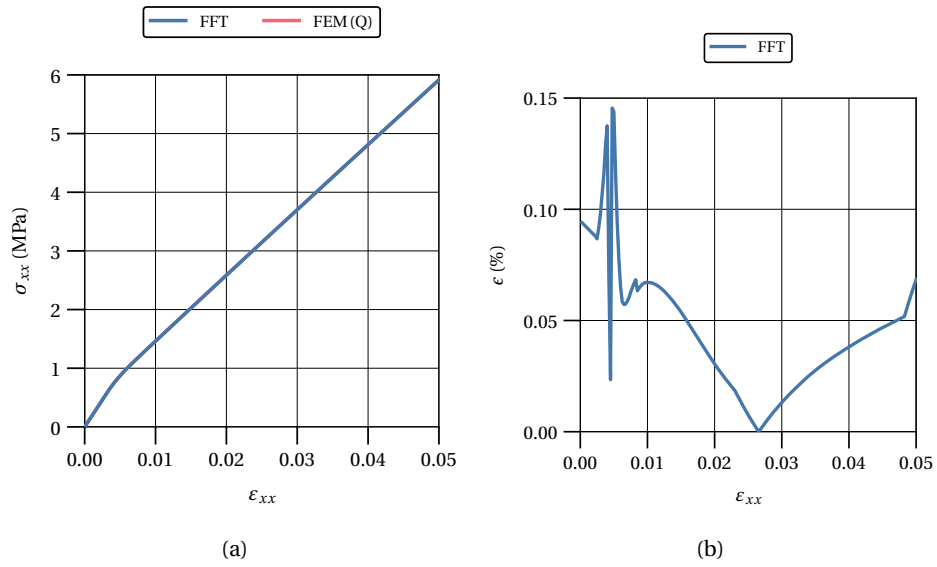


Figure 5.2: Comparison between the FFT and FEM-based homogenization approaches in the solution of the fiber-reinforced (fibers: linear elastic; matrix: elastoplastic with a von Mises associative flow rule and the isotropic piecewise linear strain hardening law) composite equilibrium problem under normal strain loading conditions: (a) Homogenized stress; (b) Computational time; Notation: quadratic element (Q).

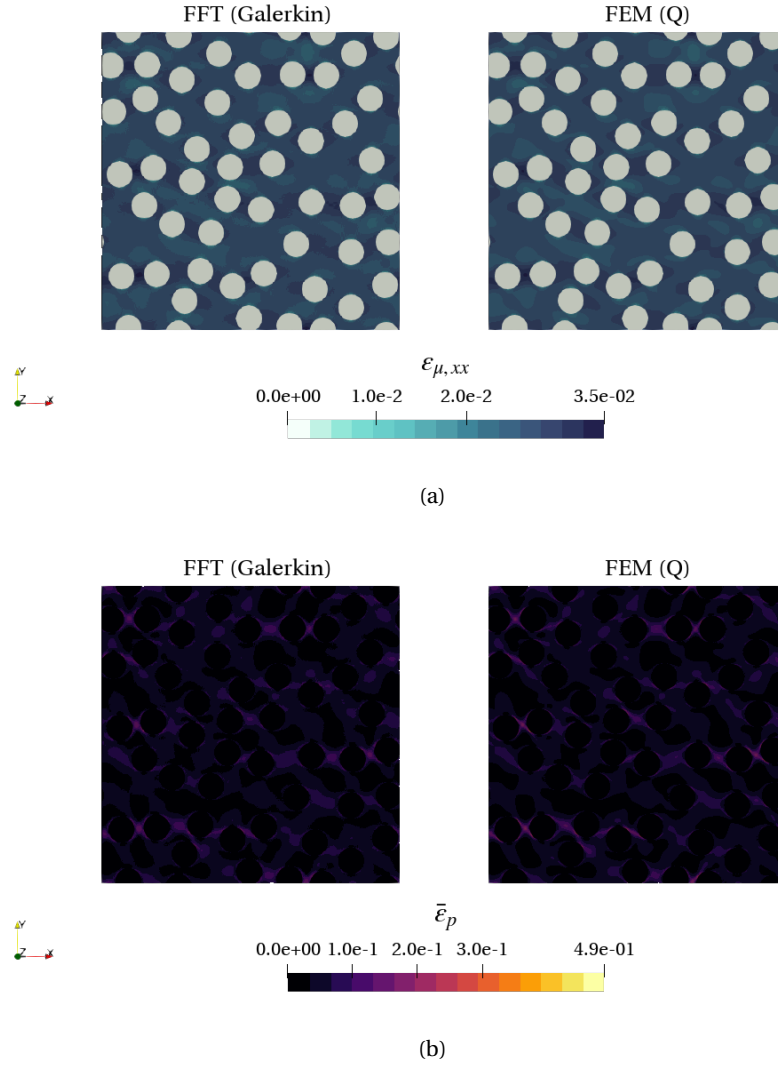


Figure 5.3: Comparison between the FFT-based and FEM-based homogenization approaches in the solution of the fiber-reinforced (fibers: linear elastic; matrix: elastoplastic with a von Mises associative flow rule and the isotropic piecewise linear strain hardening law) composite equilibrium problem under uniaxial strain loading conditions: (a) Local elastic strain field, $\varepsilon_{\mu,xx}$, of the matrix phase at full load; (b) Local accumulated plastic strain field, $\bar{\varepsilon}_p$, of the matrix phase at full load. ($n_v = 600 \times 600$ discretization). Notation: quadratic element (Q).

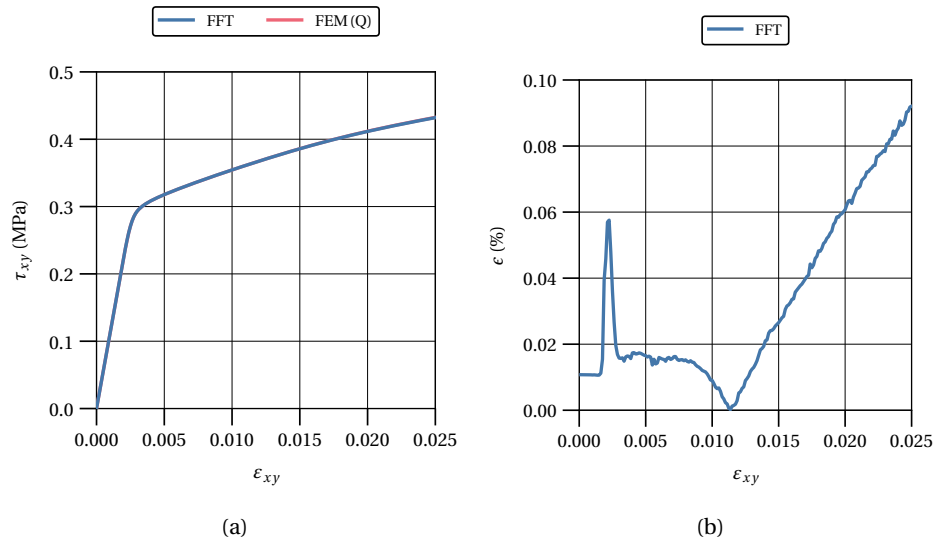


Figure 5.4: Comparison between the FFT and FEM-based homogenization approaches in the solution of the fiber-reinforced (fibers: linear elastic; matrix: elastoplastic with a von Mises associative flow rule and the isotropic piecewise linear strain hardening law) composite equilibrium problem under normal strain loading conditions: (a) Homogenized stress; (b) Computational time; Notation: linear element (L), quadratic element (Q).

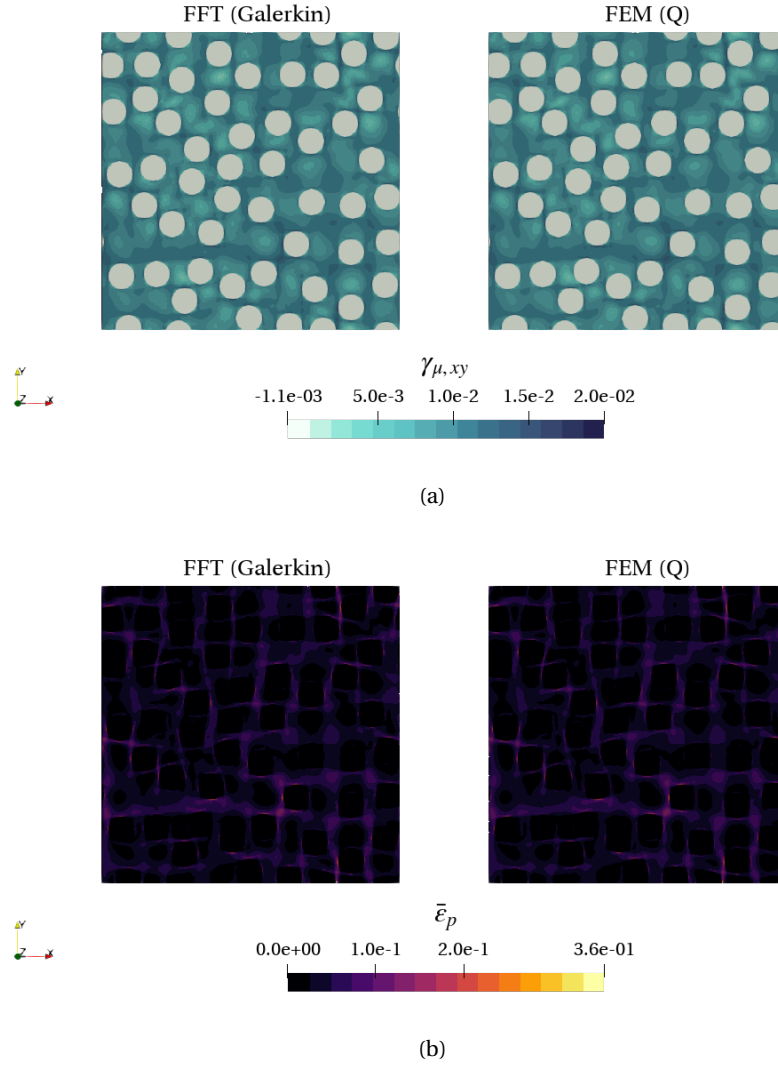


Figure 5.5: Comparison between the FFT-based and FEM-based homogenization approaches in the solution of the fiber-reinforced (fibers: linear elastic; matrix: elastoplastic with a von Mises associative flow rule and the isotropic piecewise linear strain hardening law) composite equilibrium problem under uniaxial strain loading conditions: (a) Local elastic strain field, $\epsilon_{\mu,xx}$, of the matrix phase at full load; (b) Local accumulated plastic strain field, $\bar{\epsilon}_p$, of the matrix phase at full load. ($n_v = 600 \times 600$ discretization). Notation: quadratic element (Q).

Large strain Only the two-dimensional microstructure described in Section 4.1 is again considered together with the elastic properties described in Table 4.2. The matrix is again assumed elastoplastic with a von Mises associative flow rule and the isotropic piecewise linear strain hardening law illustrated in Figure 5.1. Large strains are considered. Periodic boundary conditions are adopted and the following two macroscale strain loading cases are considered

$$\text{uniaxial: } \mathbf{F} = \begin{bmatrix} 1.1 & 0.0 \\ 0.0 & 1.0 \end{bmatrix}, \quad \text{pure shear: } \mathbf{F} = \begin{bmatrix} 1.0 & 0.3 \\ 0.0 & 1.0 \end{bmatrix}, \quad (5.26)$$

being enforced in a total of 200 increments. Note that in the 2D plane strain case, only the in-plane O_{xy} macroscale strain components are enforced. In terms of spatial discretization, a grid $n_\nu = 600 \times 600$ is considered. The convergence criterion used is Criterion II, as described in Section 3.8.

The homogenized response of the fiber-reinforced composite under uniaxial and pure shear strain loading conditions is presented in Figures 5.6 and 5.8. The relative error with respect to the FEM reference solution is also shown. An excellent agreement between the two solutions is found for uniaxial strain loading. Moreover, the error is below 0.1% for the whole deformation history. On the other hand, for the pure shear loading scheme the FFT-based approach fails to converge after $F_{xy} = 0.1$. Immediately before the error starts to increase exponentially reaching around 1.6%.

The local strain fields can be found in Figure 5.7 and 5.9. Again, visually there is no detectable difference between the local field computed using the two different approaches for the uniaxial strain loading scheme. For the FFT-based approach, the local fields are not available at full load. However, it can be gathered from the maximum values of the accumulated plastic strain, shown in Figure 5.9(b), that it reaches values as high as 1.4. It is substantially larger than the maximum value found for the uniaxial strain loading scheme, $\bar{\epsilon}_p \approx 0.7$, thus making the pure shear strain loading scheme more demanding. This helps explain why only the uniaxial strain loading scheme reached full load.

In terms of computational performance, Table 5.3 shows that the FFT approach is around 1.5 times faster than the FEM approach for the uniaxial strain loading scheme. However, as already mentioned, it fails to reach full load for the pure shear strain loading scheme.

Table 5.3: Comparison between the CPU time required by the FFT-based and FEM-based homogenization approaches in the solution of the fiber-reinforced (fibers: hyperelastic (Hencky constitutive model); matrix: elastoplastic with a von Mises associative flow rule and the isotropic piecewise linear strain hardening law) composite equilibrium problem under uniaxial and pure strain loading conditions ($n_\nu = 600 \times 600$).

Loading scheme	CPU Time (s)	
	FFT	FEM
Uniaxial strain	1.66×10^4	2.36×10^4
Pure shear strain	-	6.01×10^4

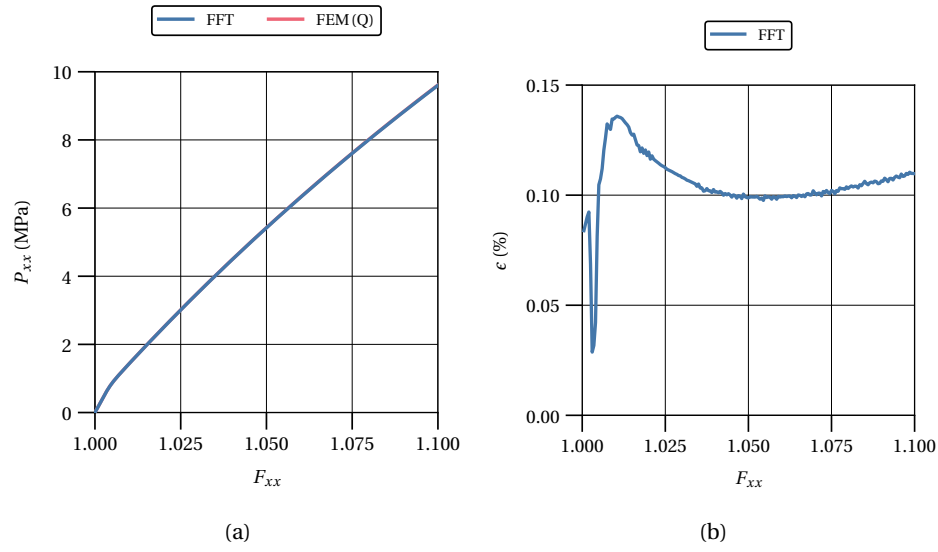


Figure 5.6: Comparison between the FFT and FEM-based homogenization approaches in the solution of the fiber-reinforced (fibers: hyperelastic (Hencky constitutive model); matrix: elastoplastic with a von Mises associative flow rule and the isotropic piecewise linear strain hardening law) composite equilibrium problem under normal strain loading conditions: (a) Homogenized stress; (b) Computational time; Notation: quadratic element (Q).

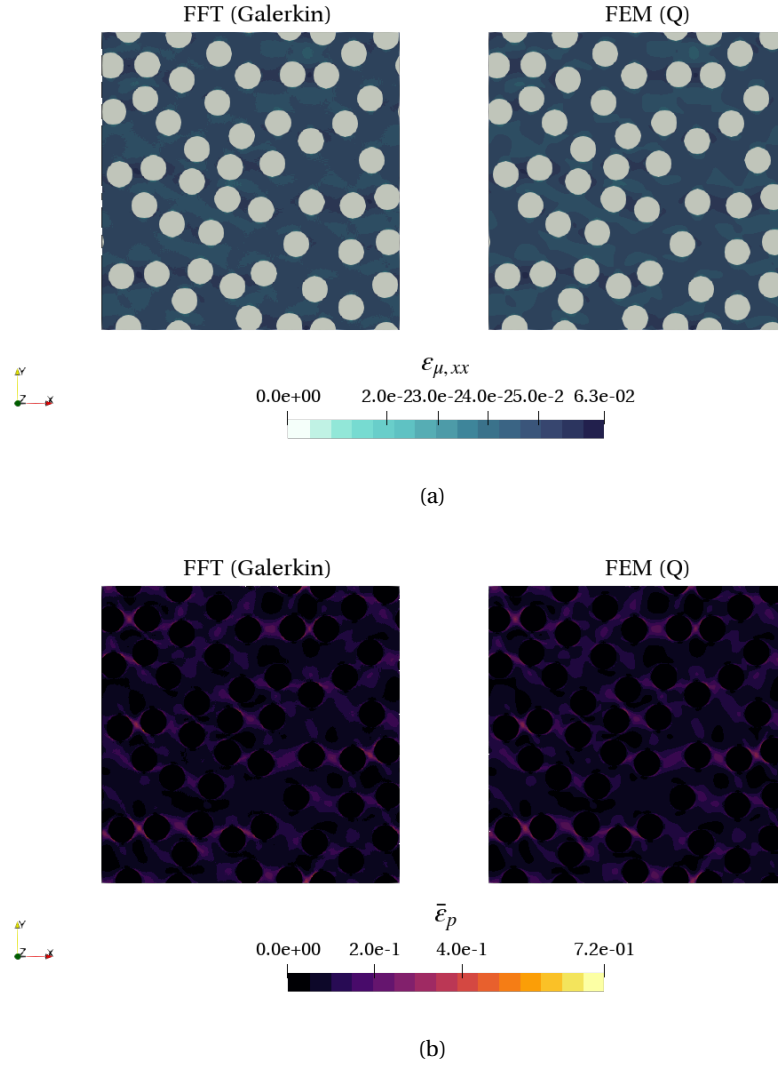


Figure 5.7: Comparison between the FFT-based and FEM-based homogenization approaches in the solution of the fiber-reinforced (fibers: hyperelastic (Hencky constitutive model); matrix: elastoplastic with a von Mises associative flow rule and the isotropic piecewise linear strain hardening law) composite equilibrium problem under uniaxial strain loading conditions: (a) Local elastic strain field, $\varepsilon_{\mu,xx}$, of the matrix phase at full load; (b) Local accumulated plastic strain field, $\bar{\varepsilon}_p$, of the matrix phase at full load. ($n_v = 600 \times 600$ discretization). Notation: quadratic element (Q).

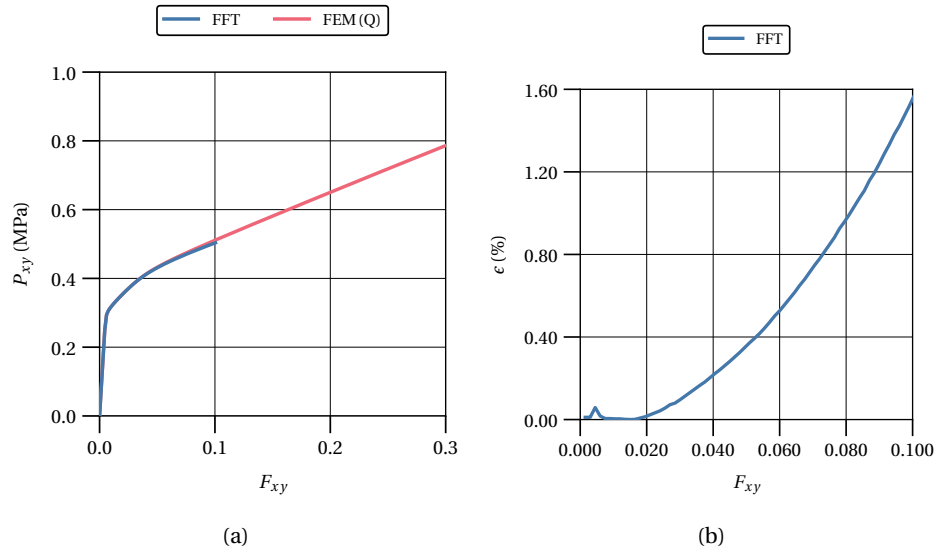


Figure 5.8: Comparison between the FFT and FEM-based homogenization approaches in the solution of the fiber-reinforced (fibers: hyperelastic (Hencky constitutive model); matrix: elastoplastic with a von Mises associative flow rule and the isotropic piecewise linear strain hardening law) composite equilibrium problem under pure shear strain loading conditions: (a) Homogenized stress; ?? Computational time; Notation: quadratic element (Q).

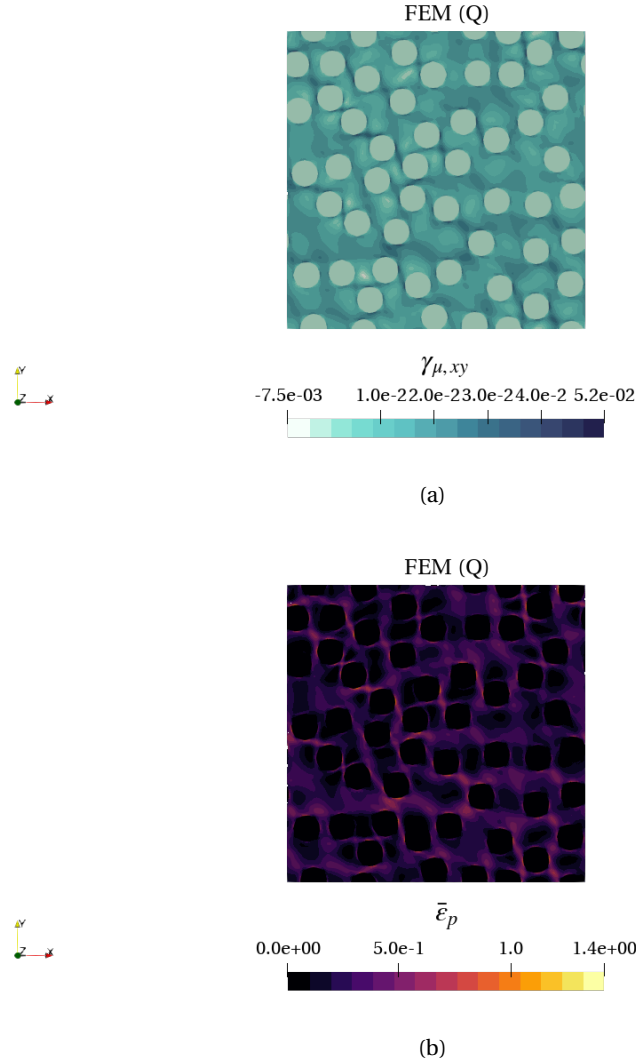


Figure 5.9: Comparison between the FFT-based and FEM-based homogenization approaches in the solution of the fiber-reinforced (fibers: hyperelastic (Hencky constitutive model); matrix: elastoplastic with a von Mises associative flow rule and the isotropic piecewise linear strain hardening law) composite equilibrium problem under pure shear strain loading conditions: ?? Local elastic strain field, $\epsilon_{\mu,xx}$, of the matrix phase at full load; ?? Local accumulated plastic strain field, $\bar{\epsilon}_p$, of the matrix phase at full load - Only FEM available since the FFT solution did not reach full load ($n_v = 600 \times 600$ discretization). Notation: quadratic element (Q).

Chapter 6

Conclusions and Future Research

6.1 Conclusions and final remarks

The main goal of the present work is to document the choice of an accurate and efficient FFT-based homogenization procedure. Both small and large strains, as well as, elastic and elastoplastic material behavior must be taken into account. With this objective in mind, an overview of the FFT-based homogenization procedures available in the literature is given and the FFT-based Galerkin method approach introduced by [Vondřejc et al. \(2014\)](#), [Zeman et al. \(2017\)](#) and [De Geus et al. \(2017\)](#) is determined to be the that more closely matches the requirements established. It also factored into this choice the availability of an implementation of this procedure (). Thus, a detailed description of the main method under review is also included based on [Zeman et al. \(2017\)](#) and [De Geus et al. \(2017\)](#).

Using the code available at , an implementation of the FFT-based Galerkin method homogenization procedure chosen was developed to test it against the FFT-based basic method homogenization procedure proposed by [Moulinec and Suquet \(1994\)](#) and the FEM-based homogenization procedure. To investigate its implementation robustness, accuracy, and efficiency, several numerical applications are presented. The numerical results are divided into two sets of results, the first concerning elasticity and the second elastoplasticity. Both small and large strains are considered in each set of results.

Regarding the elasticity at small strains, the implementation developed for the FFT-based Galerkin method homogenization scheme is validated as solutions obtained (both homogenized results and local fields) are in excellent agreement with ones obtained with the FEM-based homogenization from LINKS and the FFT-based homogenization basic scheme. In the linear elastic regime, the FFT-based homogenization Galerkin scheme outperforms the FEM-based homogenization both in terms of speed and memory footprint. This effect is much more pronounced in the three-dimensional microstructure considered than in the two-dimensional microstructure. However, it must be kept in mind that some of the Python libraries employed in the implementation of the FFT-based homogenization Galerkin scheme are parallelized and only one core is used in the LINKS simulations. Comparing both FFT-based homogenization procedures, the FFT-based homogenization basic scheme outperforms the FFT-based homogenization Galerkin scheme in terms of CPU time expended. Yet, consider that the implementation of the basic scheme used in this work ([Ferreira, 2020](#)) has already undergone some performance optimization. This is

not the case for the implementation of the FFT Galerkin scheme used.

Regarding the convergence criteria used in the present implementation of the FFT-Galerkin method ...

First, the implemented FFT-based homogenization basic scheme (Moulinec and Suquet, 1994) is validated and compared against FEM-based homogenization, both being available to perform the SCA's offline stage (linear elastic analyses under orthogonal strain loading conditions). From an implementation point of view, an optimization procedure is devised to avoid high computational costs associated with discrete frequency loops. Massive speedups are observed in the computation of the reference homogeneous material Green operator and a similar optimization approach is implemented concerning several SCA's algorithmic computations. In the linear elastic regime, it is clear that the FFT-based homogenization basic scheme outperforms the FEM-based homogenization both in terms of speed and memory footprint, being the obtained solutions (both homogenized results and local fields) in excellent agreement with each other. Therefore, it is concluded that the FFT-based homogenization methods are a suitable choice to efficiently compute the local elastic strain concentration tensors in the SCA's offline stage. Second and most importantly, some numerical examples are taken from Liu et al. (2016a) to validate the SCA's implementation. An excellent agreement is obtained and is verified that the SCA can capture the homogenized nonlinear elastoplastic behavior of both fiber and particle-reinforced composite materials (2D plane strain and 3D models, respectively) with a considerable model data compression in comparison with FEM DNS analyses. From a numerical point of view, the expected quadratic convergence rate of Newton-Raphson's method is achieved in the solution of the Lippmann-Schwinger system of equilibrium equations. This suggests that the associated linearization is properly done and that the iterative procedure embedded in the self-consistent scheme is well implemented. Moreover, at the expense of an increased computational cost, it is clear from the results that the SCA predictions accuracy increases as the number of clusters increases. The tradeoff between accuracy and computational cost is further investigated and the accuracy-efficiency balance that must be made by the analyst in the choice of the degree of data compression is evidenced accuracy and computational cost lower and upper bounds, respectively, in terms of the number of clusters. It is remarked that fairly accurate results are obtained with significantly lower computational costs in comparison with the FEM DNS solutions. At last, to gain some insight into the computational cost of the main SCA algorithmic steps, a time profile analysis is performed for different degrees of model compression. In contrast with the clustering procedure, whose relative computational time remains essentially constant, it is verified that the relative computational cost of the cluster interaction tensors computation increases significantly with the increase of the number of clusters.

6.2 Future research and challenges

In the author's opinion, the Self-Consistent Clustering Analysis (SCA) proposed by Liu et al. (2016a) provides a solid and promising foundation that can still be significantly enriched in terms of accuracy and efficiency. Having this in mind, CRATE's high-modular implementation provides a suitable computational framework to perform further developments and innovative extensions. Before those, some aspects related to the present work still need to be tackled and/or further investigated: (1) the clear understanding of the numerical dependency on the Chapter 13 269 reference

homogeneous material elastic properties (intrinsically related to the need of the self-consistent scheme and the nature of the introduced homogeneous far-field strain), (2) further evaluation of the SCA accuracy under complex strain/stress states and non-monotonic loading paths, and (3) the proper finite strain extension (Yu et al., 2019) implementation required to predict the behavior of polymeric materials under finite strains.

Bibliography

- Bonnet, G.
2007. Effective properties of elastic periodic composite media with fibers. *Journal of the Mechanics and Physics of Solids*, 55(5):881–899. Publisher: Elsevier.
- Brenner, R.
2010. Computational approach for composite materials with coupled constitutive laws. *Zeitschrift für angewandte Mathematik und Physik*, 61(5):919–927. Publisher: Springer.
- Brisard, S. and L. Dormieux
2010. FFT-based methods for the mechanics of composites: A general variational framework. *Computational Materials Science*, 49(3):663–671. Publisher: Elsevier.
- Brisard, S. and L. Dormieux
2012. Combining Galerkin approximation techniques with the principle of Hashin and Shtrikman to derive a new FFT-based numerical method for the homogenization of composites. *Computer Methods in Applied Mechanics and Engineering*, 217-220:197–212.
- Cardoso Coelho, R. P.
2019. Selection, Implementation and Benchmarking of New Direct and Iterative Solvers in LINKS. CM2S Technical report, University of Porto.
- De Geus, T., J. Vondřejc, J. Zeman, R. Peerlings, and M. Geers
2017. Finite strain FFT-based non-linear solvers made simple. *Computer Methods in Applied Mechanics and Engineering*, 318:412–430. Publisher: Elsevier.
- de Souza Neto, E., D. Peric, and D. Owen
2008. *Computational Methods for Plasticity: Theory and Applications*. Wiley.
- Djaka, K. S., A. Villani, V. Taupin, L. Capolungo, and S. Berbenni
2017. Field Dislocation Mechanics for heterogeneous elastic materials: A numerical spectral approach.
- Eisenlohr, P., M. Diehl, R. Lebensohn, and F. Roters
2013. A spectral method solution to crystal elasto-viscoplasticity at finite strains.
- Eloh, K. S., K. S. Eloh, A. Jacques, S. Berbenni, and S. Berbenni
2019. Development of a new consistent discrete green operator for FFT-based methods to solve heterogeneous problems with eigenstrains.

- Ernesti, F. and M. Schneider
2021. An FFT-based method for computing the effective crack energy of a heterogeneous material on a combinatorially consistent grid. *arXiv preprint arXiv:2103.05968*.
- Ernesti, F., M. Schneider, and T. Böhlke
2020. Fast implicit solvers for phase-field fracture problems on heterogeneous microstructures.
- Eyre, D. J. and G. W. Milton
1999. A fast numerical scheme for computing the response of composites using grid refinement. *The European Physical Journal Applied Physics*, 6(1):41–47. Publisher: EDP Sciences.
- Ferreira, B.
2020. Accurate and efficient multi-scale analyses of nonlinear heterogeneous materials based on clustering-based reduced order models. PhD Seminar, FEUP.
- Fraunhofer ITWM
2020. FeelMath - Fraunhofer ITWM. Publication Title: Fraunhofer Institute for Industrial Mathematics ITWM.
- Geus, D.
2016. From damage to fracture, from micro to macro : a systematic study of ductile fracture in multi-phase microstructures.
- Gierden, C., J. Waimann, B. Svendsen, and S. Reese
2021. A geometrically adapted reduced set of frequencies for a FFT-based microstructure simulation. *arXiv preprint arXiv:2103.10203*.
- Göküzüm, F. S., L. T. K. Nguyen, and M.-A. Keip
2019. A multiscale FE-FFT framework for electro-active materials at finite strains.
- Gélébart, L. and R. Mondon-Cancel
2013. Non-linear extension of FFT-based methods accelerated by conjugate gradients to evaluate the mechanical behavior of composite materials. *Computational Materials Science*, 77:430–439. Publisher: Elsevier.
- Gupta, A.
2002a. Improved Symbolic and Numerical Factorization Algorithms for Unsymmetric Sparse Matrices. *SIAM Journal on Matrix Analysis and Applications*, 24.
- Gupta, A.
2002b. WSMP: Watson Sparse Matrix Package Part II - direct solution of general sparse systems. *Future Generation Computer Systems*.
- Hashin, Z. a. and S. Shtrikman
1962. On some variational principles in anisotropic and nonhomogeneous elasticity. *Journal of the Mechanics and Physics of Solids*, 10(4):335–342. Publisher: Elsevier.
- Kabel, M., T. Böhlke, and M. Schneider
2014. Efficient fixed point and Newton–Krylov solvers for FFT-based homogenization of elasticity at large deformations.

- Kabel, M., A. Fink, and M. Schneider
2017. The composite voxel technique for inelastic problems. *Computer Methods in Applied Mechanics and Engineering*, 322:396–418. Publisher: Elsevier.
- Kochmann, J., L. Ehle, S. Wulfinghoff, J. Mayer, B. Svendsen, and S. Reese
2018a. Efficient multiscale FE-FFT-based modeling and simulation of macroscopic deformation processes with non-linear heterogeneous microstructures.
- Kochmann, J., K. Manjunatha, C. Gierden, S. Wulfinghoff, B. Svendsen, and S. Reese
2019. A simple and flexible model order reduction method for FFT-based homogenization problems using a sparse sampling technique. *Computer Methods in Applied Mechanics and Engineering*, 347:622–638. Publisher: Elsevier.
- Kochmann, J., S. Wulfinghoff, L. Ehle, J. Mayer, B. Svendsen, and S. Reese
2018b. Efficient and accurate two-scale FE-FFT-based prediction of the effective material behavior of elasto-viscoplastic polycrystals.
- Lahellec, N., J.-C. Michel, H. Moulinec, and P. Suquet
2003. Analysis of inhomogeneous materials at large strains using fast Fourier transforms. In *IUTAM symposium on computational mechanics of solid materials at large strains*, Pp. 247–258. Springer.
- Lebensohn, R.
2001. N-site modeling of a 3D viscoplastic polycrystal using Fast Fourier Transform.
- Lebensohn, R. and A. Rollett
2020. Spectral methods for full-field micromechanical modelling of polycrystalline materials.
- Lucarini, S. and J. Segurado
2019a. An algorithm for stress and mixed control in Galerkin based FFT homogenization.
- Lucarini, S. and J. Segurado
2019b. DBFFT: A displacement based FFT approach for homogenization of the mechanical behavior.
- Ma, R. and T. J. Truster
2019. FFT-based homogenization of hypoelastic plasticity at finite strains.
- Ma, X., M. Shakoov, D. Vasiukov, S. V. Lomov, and C. H. Park
2021. Numerical artifacts of Fast Fourier Transform solvers for elastic problems of multi-phase materials: their causes and reduction methods. *Computational Mechanics*, Pp. 1–23. Publisher: Springer.
- Magri, M., S. Lucarini, G. Lemoine, L. Adam, and J. Segurado
2021. An FFT framework for simulating non-local ductile failure in heterogeneous materials. *Computer Methods in Applied Mechanics and Engineering*, 380:113759. Publisher: Elsevier.
- Mareau, C. and C. Robert
2017. Different composite voxel methods for the numerical homogenization of heterogeneous inelastic materials with FFT-based techniques.

- Michel, J., H. Moulinec, and P. Suquet
2000. A computational method based on augmented Lagrangians and fast Fourier transforms for composites with high contrast. *CMES(Computer Modelling in Engineering & Sciences)*, 1(2):79–88.
- Michel, J., H. Moulinec, and P. Suquet
2001. A computational scheme for linear and non-linear composites with arbitrary phase contrast. *International Journal for Numerical Methods in Engineering*, 52(1-2):139–160. Publisher: Wiley Online Library.
- Michel, J.-C., H. Moulinec, and P. Suquet
1999. Effective properties of composite materials with periodic microstructure: a computational approach. *Computer methods in applied mechanics and engineering*, 172(1-4):109–143. Publisher: Elsevier.
- Mishra, N., J. Vondrejč, and J. Zeman
2015. Block Conjugate Gradient Iteration for Fourier-Galerkin Homogenization of Periodic Media.
- Mishra, N., J. Vondrejč, and J. Zeman
2016. A comparative study on low-memory iterative solvers for FFT-based homogenization of periodic media.
- Monchiet, V.
2015. Combining FFT methods and standard variational principles to compute bounds and estimates for the properties of elastic composites.
- Monchiet, V. and G. Bonnet
2012. A polarization-based FFT iterative scheme for computing the effective properties of elastic composites with arbitrary contrast. *International Journal for Numerical Methods in Engineering*, 89(11):1419–1436. Publisher: Wiley Online Library.
- Moulinec, H. and F. Silva
2014. Comparison of three accelerated FFT-based schemes for computing the mechanical response of composite materials.
- Moulinec, H., F. Silva, P. Suquet, and C. Lma
2014. Comparison of different FFT-based methods for computing the mechanical response of heterogeneous materials.
- Moulinec, H. and P. Suquet
1994. A fast numerical method for computing the linear and nonlinear mechanical properties of composites. *Comptes rendus de l'Académie des sciences. Série II. Mécanique, physique, chimie, astronomie*.
- Moulinec, H. and P. Suquet
1995. A FFT-based numerical method for computing the mechanical properties of composites from images of their microstructures. In *IUTAM symposium on microstructure-property interactions in composite materials*, Pp. 235–246. Springer.
- Moulinec, H. and P. Suquet
1998. A numerical method for computing the overall response of nonlinear

- composites with complex microstructure. *Computer methods in applied mechanics and engineering*, 157(1-2):69–94. Publisher: Elsevier.
- Moulinec, H., P. Suquet, and G. W. Milton
2018. Convergence of iterative methods based on Neumann series for composite materials: Theory and practice. *International Journal for Numerical Methods in Engineering*, 114(10):1103–1130. Publisher: Wiley Online Library.
- Nguyen, M.-T., Q.-D. To, and V. Monchiet
2021. Derivation of FFT numerical bounds of the effective properties of composites and polycrystals. *Theoretical and Applied Mechanics Letters*, P. 100236. Publisher: Elsevier.
- Roters, F., M. Diehl, P. Shanthraj, P. Eisenlohr, C. Reuber, S. L. Wong, T. Maiti, A. Ebrahimi, T. Hochrainer, H.-O. Fabritius, and others
2019. DAMASK–The Düsseldorf Advanced Material Simulation Kit for modeling multi-physics crystal plasticity, thermal, and damage phenomena from the single crystal up to the component scale. *Computational Materials Science*, 158:420–478. Publisher: Elsevier.
- Schenk, O. and K. Gärtner
2004. Solving unsymmetric sparse systems of linear equations with pardiso. *Future Generation Computer Systems*, 20(3):475–487.
- Schenk, O., K. Gärtner, W. Fichtner, and A. Stricker
2001. Pardiso: a high-performance serial and parallel sparse linear solver in semiconductor device simulation. *Future Generation Computer Systems*, 18(1):69–78.
- Schneider, M.
2019. On the Barzilai-Borwein basic scheme in FFT-based computational homogenization. *International Journal for Numerical Methods in Engineering*, 118(8):482–494. Publisher: Wiley Online Library.
- Schneider, M.
2020a. A dynamical view of nonlinear conjugate gradient methods with applications to FFT-based computational micromechanics. *Computational Mechanics*, 66(1):239–257.
- Schneider, M.
2020b. Lippmann-Schwinger solvers for the computational homogenization of materials with pores.
- Schneider, M., D. Merkert, and M. Kabel
2017. FFT-based homogenization for microstructures discretized by linear hexahedral elements.
- Schneider, M., F. Ospald, and M. Kabel
2016. Computational homogenization of elasticity on a staggered grid.
- Schneider, M., D. Wicht, and T. Böhlke
2019. On polarization-based schemes for the FFT-based computational homogenization of inelastic materials.

- Schwichow, S.
2020. GeoDict Startpage. Publication Title: Math2Market.
- Shanthraj, P., M. Diehl, P. Eisenlohr, F. Roters, and D. Raabe
2019. Spectral Solvers for Crystal Plasticity and Multi-physics Simulations.
- Shanthraj, P., P. Eisenlohr, M. Diehl, and F. Roters
2015. Numerically robust spectral methods for crystal plasticity simulations of heterogeneous materials. *International Journal of Plasticity*, 66:31–45. Publisher: Elsevier.
- To, Q. and G. Bonnet
2020. FFT based numerical homogenization method for porous conductive materials.
- Tu, F., Y. Jiao, X. Zhou, Y. Cheng, and F. Tan
2020. The implementation of B-splines to Hashin and Shtrikman variational principle based FFT method for the homogenization of composite. *International Journal of Solids and Structures*, 191:133–145. Publisher: Elsevier.
- Vinogradov, V. and G. Milton
2008. An accelerated FFT algorithm for thermoelastic and non-linear composites. *International Journal for Numerical Methods in Engineering*, 76(11):1678–1695. Publisher: Wiley Online Library.
- Vondřejc, J., J. Zeman, and I. Marek
2014. An FFT-based Galerkin method for homogenization of periodic media. *Computers & Mathematics with Applications*, 68(3):156–173. Publisher: Elsevier.
- Vondřejc, J., J. Zeman, and I. Marek
2015. Guaranteed upper-lower bounds on homogenized properties by FFT-based Galerkin method.
- Vondřejc, J. and T. W. J. d. Geus
2020. Energy-based comparison between the Fourier-Galerkin method and the finite element method.
- Wang, B., G. Fang, S. Liu, M. Fu, and J. Liang
2018. Progressive damage analysis of 3D braided composites using FFT-based method.
- Wicht, D., M. Schneider, and T. Böhlke
2019. On Quasi-Newton methods in fast Fourier transform-based micromechanics [in press].
- Wicht, D., M. Schneider, and T. Böhlke
2020a. Computing the effective response of heterogeneous materials with thermomechanically coupled constituents by an implicit FFT-based approach.
- Wicht, D., M. Schneider, and T. Böhlke
2020b. An efficient solution scheme for small-strain crystal-elasto-viscoplasticity in a dual framework.

Wicht, D., M. Schneider, and T. Böhlke

2021. Anderson-accelerated polarization schemes for fast Fourier transform-based computational homogenization. *International Journal for Numerical Methods in Engineering*, 122(9):2287–2311. Publisher: Wiley Online Library.

Willot, F.

2015. Fourier-based schemes for computing the mechanical response of composites with accurate local fields.

Willot, F., B. Abdallah, and Y.-P. Pellegrini

2014. Fourier-based schemes with modified Green operator for computing the electrical response of heterogeneous media with accurate local fields. *International Journal for Numerical Methods in Engineering*, 98(7):518–533. Publisher: Wiley Online Library.

Willot, F. and Y.-P. Pellegrini

2008. Fast Fourier transform computations and build-up of plastic deformation in 2D, elastic-perfectly plastic, pixelwise disordered porous media. *arXiv preprint arXiv:0802.2488*.

Yvonnet, J.

2012. A fast method for solving microstructural problems defined by digital images: a space Lippmann–Schwinger scheme. *International Journal for Numerical Methods in Engineering*, 92(2):178–205. Publisher: Wiley Online Library.

Zeman, J., T. W. de Geus, J. Vondřejc, R. H. Peerlings, and M. G. Geers

2017. A finite element perspective on nonlinear FFT-based micromechanical simulations. *International Journal for Numerical Methods in Engineering*, 111(10):903–926. Publisher: Wiley Online Library.

Zeman, J., J. Vondřejc, J. Novák, and I. Marek

2010. Accelerating a FFT-based solver for numerical homogenization of periodic media by conjugate gradients. *Journal of Computational Physics*, 229(21):8065–8071. Publisher: Elsevier.

Zhou, H. and K. Bhattacharya

2020. Accelerated computational micromechanics.